Shot Noise Limited Ultrafast Spectroscopy of Magnetic
Thin Films Using Extreme Ultraviolet Light

by

Peter Johnsen

A.B. Physics, Princeton University, 2015

M.S. Physics, University of Colorado Boulder, 2019

A thesis submitted to the

Faculty of the Graduate School of the

University of Colorado in partial fulfillment

of the requirements for the degree of

Doctor of Philosophy

Department of Physics

2022

Committee Members:

Margaret Murnane, Chair

Henry Kapteyn

Joseph Berry

Sandeep Sharma

Hans Nembach

Johnsen, Peter (Ph.D., Physics)

Shot Noise Limited Ultrafast Spectroscopy of Magnetic Thin Films Using Extreme Ultraviolet Light

Thesis directed by Prof. Margaret Murnane

High harmonic generation makes it possible to measure the fastest spin and charge dynamics in materials on femtosecond to attosecond timescales. However, the extreme nonlinear nature of the high harmonic process means that intensity fluctuations can limit measurement sensitivity. In this work, I present a noise-cancelled, tabletop high harmonic beamline for time-resolved reflection mode spectroscopy of magnetic materials. I use a reference spectrometer to independently normalize the intensity fluctuations of each harmonic order and also eliminate long term drift, which allows us to make spectroscopic measurements near the shot noise limit. These improvements allow us to significantly reduce the integration time required for high signal-to-noise (SNR) measurements of element-specific spin dynamics. I also present time- and element-resolved measurements of the spin dynamics of two half-metallic Heusler compounds, NiMnSb and Co_2MnGa. I show that we can directly control the spin dynamics of these materials with optical pulses due to their unique band structures, enabling the transfer of magnetization from one element to another. These results demonstrate our ability to precisely manipulate the magnetization of complex materials on femtosecond timescales. Looking forward, improvements in EUV flux, optical coatings, and grating design can further reduce the acquisition time for high SNR measurements by an additional 1-2 orders of magnitude, enabling dramatically improved sensitivity to spin, charge and phonon dynamics in multilayer and alloyed magnetic materials.

Dedication

To my friends and family, and to the beauty of the natural world, that in our study of it, we don't forget to see it.

Acknowledgements

First and foremost, thanks be to almighty God, who made the heavens and the earth, the bosons and the fermions, for making my work possible and for spiritual comfort on a long and sometimes dark journey. Thank you to my advisors Henry Kapteyn and Margaret Murnane for the great scientific opportunities you have provided. I also want to thank you for the wonderful extra-scientific opportunities you provided: our group ski and mountain biking trips have been some of the highlights of my time in graduate school. Thank you to Sinéad Ryan, for helping me the entire way through building a really challenging experiment, and for hundreds of hours discussing fundamental concepts in magnetism. Thank you to Robert Karl and Charles Bevis, for teaching me how to operate an ultrafast laser system. Thank you to Michael Tanksalvala for a nearly endless number of discussions about interesting questions, scientific and otherwise. Thank you to Michaël Hemmer for inspiring me to truly understand my experiments and not to be intimidated by anything. Thank you to the rest of the KM group, for helping me to solve problems, for big-picture scientific debates, and for so many fantastic group lunches and discussions. Thank you to my friends, especially Nathan Brooks, Wren Suess, Eric Rosenthal, Michael Hoefer, Ellen Rumley, Max Urmey, Thomas Greenspan, Kelly Kochanski, and Geoffrey Bostany, for your constant encouragement and keeping my spirits high. Thank you to James Uhrich for your help building and repairing parts at the very last second, and to the rest of the instrument shop for your advice and support. Thank you to Erik Hosler for many long discussions about high harmonic generation. Thank you to Henrike Probst, for braving the TSA and bringing many interesting (and totally harmless) samples from Göttingen to Boulder. Thank you to Bob McLeod and Kelvin Wagner for your amazing classes and

for good research and life advice. Thank you to Tessa Calhoun for mentorship in my undergraduate research and for introducing me to lasers. Finally, thank you to my family, who have been there cheering for me since day one. I love you all.

Contents

Chapter

Tables

Table

Figures

Figure

Chapter 1

Introduction

Condensed matter systems have multiple kinds of internal degrees of freedom: charge (corresponding to the presence or absence of electrons), spin (corresponding to the angular momentum of electrons), orbital (corresponding to the spatial distribution of electrons), and lattice (corresponding to the spatial distribution of atomic nuclei). The structure of and couplings between these degrees of freedom defines the behavior of all condensed matter systems, and the observation of ultrafast laser induced demagnetization has fundamentally restructured our understanding of the coupling between these degrees of freedom.

When a femtosecond laser pulse is incident on a magnetic material, it excites electrons into a highly non-equilibrium distribution. These excited electrons can then exchange energy and angular momentum with each other and with the lattice. Before the observation of laser induced demagnetization, the fastest spin-lattice interaction was thought to be 10s or 100s of picoseconds. The discovery that demagnezation could proceed in under 1 ps revealed there must be strong unknown interactions coupling the spin system to the lattice. Since this discovery, ultrafast magnetism has become an active area of research with aims both to uncover the fundamental interactions of condensed matter systems and to use these fundamental interactions to control a material's magnetic state on femtosecond timescales for technological purposes.

Because these magnetic interactions take place on subpicosecond timescales, ultrafast laser pulses are not only a suitable excitation, but also an ideal probe. Extreme ultraviolet (EUV) light is a particularly good probe because it can excite atomic core-to-shell transitions and thereby obtain

element specific magnetic information which is critical for the study of multi-element alloys. A process called high harmonic generation (HHG) can produce these EUV wavelengths by converting infrared light into EUV light. HHG additionally offers perfect temporal synchronization between the driving infrared laser and the generated EUV light, making it the ideal light source for studying ultrafast magnetism.

In this thesis, I will discuss the fundamentals of magnetism with particular emphasis on magnetic metals, magneto-optical effects, and known ultrafast magnetic interactions (Chapter 2). I will also discuss the physics of high harmonic generation and practical methods of its implementation (Chapter 3). I will then describe the intensity normalizing ultrafast EUV spectrometer I built for measuring magnetic dynamics using the transverse magneto-optical kerr effect (TMOKE), and I will demonstrate that this instrument operates near the shot-noise limit, significantly improving the signal-to-noise ratio (SNR) and acquisition time of our measurements (Chapter 4). Finally, I will discuss measurements taken with this new instrument on two different half-metallic ferromagnets in the Heusler family, NiMnSb and Co_2MnGa. I present evidence for optical intersite spin transfer (OISTR) in these materials, where magnetization is directly transferred from one element to another by an optical pulse. In fluence dependent studies of NiMnSb, I present evidence for laser induced changes to the material's band structure. In Co_2MnGa, a magnetic Weyl semimetal, I observe a large transient enhancement of the Co TMOKE signal as well as an unexpected time delay between magnetic and electronic responses of this material. The new instrument presented in this thesis represents a significant advance in HHG experimentation with special applicability to the study of ultrafast magnetism, as demonstrated by challenging measurements on complex magnetic compounds with extremely small magnetic moments. The scientific results of this thesis elucidate the spin dynamics of multi-element compounds at multiple points throughout their band structures, an important step forward in understanding optical interactions in condensed matter systems.

Chapter 2

Magnetism

Magnetism is a complex topic of study with a long history, and many large textbooks have been written on the matter. It has historically been the subject of a variety of strange and interesting theories (for example, until the 1700s it was commonly believed that garlic and magnets were "enemies" [1]). Rather than attempt to review the entirety of magnetism, I will start from first principles to describe a minimal amount of background information on magnetism necessary for understanding the interaction of light and magnetism on femtosecond time scales. I will start with the origin of magnetism in materials, especially in metals, and describe two complementary models of magnetism. I then discuss a variety of common magnetic interactions and their applicability to optically induced magnetic phenomena. I review Maxwell's equations in magnetic materials and the dielectric tensor, which allows us to describe various magneto-optic effects. I describe the geometry and effect of three magneto-optic Kerr effects (MOKEs): longitudinal (LMOKE), polar (PMOKE), and transverse (TMOKE). Finally, I discuss the microscopic origin and selection rules of x-ray magnetic circular dichroism, and discuss the origin and interpretation of extreme ultraviolet (EUV) TMOKE.

2.1   The origin of magnetism

2.1.1   Current Loops

Since there are no magnetic monopoles, all magnetic fields must originate from arrangements of magnetic dipoles. The simplest way to generate such a field is by running a current in a

wire loop, as shown below:
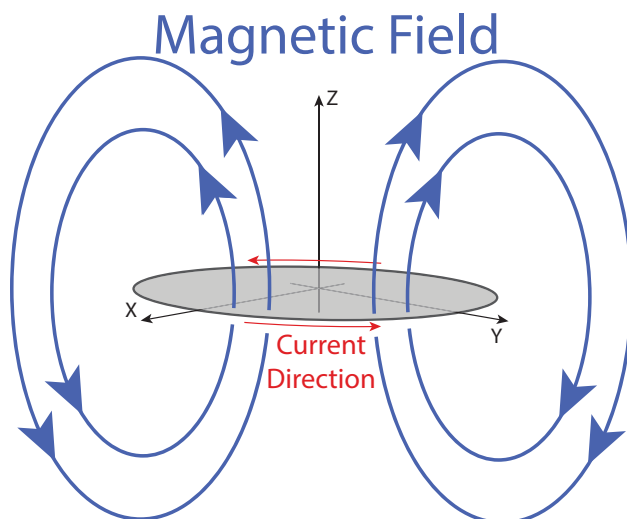
Figure 2.1: **The dipolar magnetic field generated by flowing wire through a current loop.** The loop encloses a total area A.

The Biot-Savart law gives us the magnitude of the magnetic induction at an arbitrary point in space:

$$dB = \frac{\mu_0 I}{4\pi r^2} \left(dL \times r \right) \tag{2.1}$$

where dB is the infinitesimal magnetic induction, μ_0 is the permeability of free space, I is the current, dL is the infinitesimal length of wire, and r is the vector from the wire to the given point in space. We can write the strength of the magnetic dipole moment as:

$$\mu = IA \tag{2.2}$$

where I is again the current and A is the area enclosed by the loop.

Considering the magnetic dipole from this approach, we can intuitively understand why magnetic fields carry angular momentum: they are always mathematically equivalent to a circular current loop that carries with it an associated angular momentum.

2.1.2   Electron Spin

All known fundamental particles have an intrinsic spin (or lack thereof) that cannot be altered: fermions have half-integer spin and bosons have integer spin. This spin gives charged particles an intrinsic magnetic dipole moment, as if they were spinning about their axis (although whether or not fundamental particles actually spin is unclear). A particle's spin obeys the same laws as other quantized angular momenta, and so it can be considered a particle's intrinsic angular momentum. An electron's spin quantum number is always 1/2, but it's measured value can be positive or negative (this can be interpreted as pointing with or against the measurement axis). The eigenvalues of the spin operator $\hat{s}_i$ are:

$$\hat{s}_i |\psi_{s,m_s}\rangle = m_s |\psi_{s,m_s}\rangle \tag{2.3}$$

where i is the measurement axis, $s = 1/2$, $m_s = \pm 1/2$. We will generally take the measurement axis to be the z-axis. We can find the total spin angular momentum by looking for the eigenvalues of the total spin operator $\hat{S}^2 = \hat{s}_x^2 + \hat{s}_y^2 + \hat{s}_z^2$:

$$\hat{S}^2 |\psi_{s,m_s}\rangle = \hbar^2 s(s+1) |\psi_{s,m_s}\rangle = 3\hbar^2/4 |\psi_{s,m_s}\rangle \tag{2.4}$$

Note that $|\psi_{s,m_s}\rangle$ is a simultaneous eigenstate of $\hat{S}^2$ and $\hat{s}_i$ because they commute:

$$\left[\hat{S}^2, \hat{s}_i\right] = 0 \tag{2.5}$$

Importantly, $\hat{s}_x$, $\hat{s}_y$, and $\hat{s}_z$ *do not* commute: it is impossible to know the projection of the electrons angular momentum on two axes simultaneously. This fact can be represented as the two spin operators having a non-zero commutator:

$$[\hat{s}_i, \hat{s}_j] = i\hbar \tag{2.6}$$

We can now relate the electron's z-component of angular momentum ($\pm\hbar/2$) to its magnetic moment by assuming the electron has a classical circular orbit with angular momentum $\hbar/2$. First,

we compute the current of a single electron orbit:

$$I = -\frac{e}{T} \tag{2.7}$$

$$= -\frac{ev}{2\pi r} \tag{2.8}$$

$$= -\frac{ev}{2\pi r^2}\frac{m_e r}{m_e} \tag{2.9}$$

where e is the electron charge, T is the orbital period, v is the electron's velocity, and r is the radius of the orbit. In the final step, we have simply multiplied by $1 = m_e r/m_e r$ for convenience later. Now, we note that the area of the circular orbit is simply $A = \pi r^2$. Finally, we combine these into the electron's magnetic moment, remembering that $L = mr \times v$, classical expression for angular momentum:

$$\mu_z = IA \tag{2.10}$$

$$= -\frac{ev}{2\pi r^2}\frac{m_e r}{m_e}\left(\pi r^2\right) \tag{2.11}$$

$$= -\frac{e}{2m_e}(m_e rv) \tag{2.12}$$

$$= -\frac{e}{2m_e}L_z \tag{2.13}$$

$$= \pm\frac{1}{2}\frac{\hbar e}{2m_e} \tag{2.14}$$

$$= \pm\frac{1}{2}\mu_B \tag{2.15}$$

where we have used $L_z = \hbar/2$, the z-component of the electron's angular momentum, and have defined a new quantity called the *Bohr magneton*:

$$\mu_B = \frac{\hbar e}{2m_e} \tag{2.16}$$

The Bohr magneton is a natural, atomic scale unit for magnetic moment. It might have seemed strange to assume that an electron has an intrinsic magnetic moment that is equivalent to it moving in a classical circular orbit, but interestingly, the measured magnetic moment is about double that of the expression in Equation 2.15. The correct expression is as follows:

$$\mu_{s,z} = \pm\frac{1}{2}g_s\mu_B \tag{2.17}$$

where we have introduced the electron spin g-factor $g_S \approx 2$. (In fact, the electron spin g-factor is known very precisely: $g_S = 2.00231930436256(35)$. This small deviation away from exactly 2 arises as a consequence of relativistic quantum mechanics [2, 3], but we can safely ignore this for our purposes). The electron spin g-factor is a phenomenological proportionality factor between the electron spin and it's magnetic moment. Thus, the z-component of the magnetic moment for a free electron is roughly one Bohr magneton. If we wish instead to consider the total spin magnetic moment, we can see that it is proportional to the total spin angular momentum $\boldsymbol{S}$:

$$\boldsymbol{\mu}_S = \frac{\boldsymbol{S}}{\hbar} g_S \mu_B \tag{2.18}$$

2.1.3   Orbital magnetism

Since we calculated the electron's intrinsic magnetic moment by considering a classical orbit, we can reason that the electron's actual orbital should also carry some angular momentum and therefore carry a magnetic moment. This can be done relatively simply: we take Equation 2.13 and insert the value of the angular momentum for a given electron orbital. Orbital angular momentum values are given in Table 2.1 below:

Orbital	ℓ	m_ℓ
s	0	0
p	1	-1, 0, 1
d	2	-2, 1, 0, 1, 2
f	3	-3, -2, 1, 0, 1, 2, 3

Table 2.1: **Azimuthal quantum numbers for atomic orbitals.**

We we can now write the orbital magnetic moment as:

$$\boldsymbol{\mu}_L = -\frac{\boldsymbol{L}}{\hbar} g_L \mu_B \tag{2.19}$$

where $\boldsymbol{L}$ is the total angular momentum and we have introduced the orbital g-factor $g_L = 1$. The

magnetic moment of an electron orbital is exactly what we would expect from a classical calculation of the magnetic moment (while also taking into consideration that these orbits are quantized). This orbital magnetic moment can contribute substantially to material's magnetic moment (like cobalt platinum alloys), or not at all (like hydrogen in its ground state), depending on the material in consideration.

2.1.4 Spin-orbit coupling

We can intuitively understand the spin-orbit coupling through the lens of magnetic dipole interactions. The electron's orbit generates a magnetic field which interacts with the electron's spin (which is its intrinsic magnetic moment). In order to compute this interaction, we will find the total angular momentum of our electron by adding the spin angular momentum to the orbital angular momentum. To do so, we call to mind the rules for adding vectors in quantum mechanics [4] and obtain:

$$J = |\ell - s|, |\ell - s| + 1, ..., \ell + s, \quad m_J = -J, -J + 1, ..., J \tag{2.20}$$

meaning that J can take any value between $|\ell - s|$ and $\ell + s$ Now that we have obtained the total angular momentum J for our electron, we can express the magnetic moment of the associated state as:

$$|\boldsymbol{\mu}_J| = -\frac{|\boldsymbol{J}|}{\hbar} g_J \mu_B \tag{2.21}$$

where g_J is the Landé g-factor:

$$g_J = 1 + \frac{J(J+1) + s(s+1) - \ell(\ell+1)}{2J(J+1)} \tag{2.22}$$

To relate the total magnetic moment to the total angular momentum in Equation 2.21, we must compare magnitudes of $\boldsymbol{\mu_J}$ and $\boldsymbol{J}$. This is because $\boldsymbol{\mu_J}$ does not lie along $\boldsymbol{J}$ since $\boldsymbol{\mu}_J = \boldsymbol{\mu}_L + \boldsymbol{\mu}_s$ and $\boldsymbol{J} = \boldsymbol{L} + \boldsymbol{S}$, and the values of the g-factors relating $\boldsymbol{L}$ and $\boldsymbol{S}$ to their respective magnetic moments are different.

In real materials, the magnitude of the spin-orbit interaction varies greatly. We can write

a simple Hamiltonian for this interaction:

$$\hat{H}_{SO} = \xi_{n\ell}\hat{S} \cdot \hat{L} \tag{2.23}$$

where $\xi_{n\ell}$ is the spin-orbit coupling constant that depends on the quantum numbers n and ℓ and has units of energy [5]. The spin-orbit interaction in $3d$ transition metals is weak, roughly 10-100 meV in their valence shells, and in these materials the orbital magnetism does not play a large role in the overall magnetization of the system. Nevertheless, the spin-orbit coupling plays an important role in solid-state magnetism for $3d$ metals because it couples the spin system to the crystal lattice. This coupling to the lattice sets a preferred direction for the overall magnetization of the system because of the arrangement of the unit cell; this phenomenon is called *magnetocrystalline anisotropy.* This lattice coupling also allows for a material to exchange angular momentum between the spin system and phonon modes, an important interaction in the study of ultrafast magnetic dynamics.

The spin-orbit interaction also mixes spin states, so that spin is no longer a good quantum number. The amount of this mixing can vary greatly - in the d shell, the spin mixing is quite small and spin is a "pretty good" quantum number, although the spin-orbit interaction still plays in important role in processes that flip electron spins (See Chapter 2.5.1). The spin-orbit interaction also converts the p orbitals into triplet and singlet manifolds which play an important role in x-ray measurements of magnetism (see Chapter 2.8).

In heavy elements, like lead or uranium, the spin-orbit interaction can lead to large energy shifts in their valence shells on the order of multiple eV. Because the spin-orbit interaction is so strong, we must consider the total angular momentum quantum number of the electron and can no longer consider its spin and orbital numbers to be good approximations, meaning that the spin-orbit coupling can no longer be treated as a perturbation to the original energy levels. Calculating magnetic effects for such materials can be substantially different than for the $3d$ transition metals. When the spin-orbit interaction is very strong and spin is no longer a good quantum number, every electron is defined by its total angular momentum and we call this the *j-j coupling scheme.* For lighter elements, by contrast, the spin orbit coupling is weaker and we can consider the spin

and orbital components of the electron's angular momentum independently - this is called the *Russel-Saunders coupling scheme*.

2.1.5   The exchange interaction

The exchange interaction in magnetism refers to the interplay of the Pauli principle and the Coulomb interaction that generates magnetic order. The Pauli principle states that the total wavefunction for fermions must be antisymmetric under the exchange of any two particles. The total wavefunction Ψ can be expressed as follows:

$$\Psi(r_1, r_2) = \Phi(r_1, r_2)\sigma(r_1, r_2) \tag{2.24}$$

where $\Phi(r_1, r2)$ is the spatial part of the wavefunction and $\sigma(r_1, r_2)$ is the spin part of the wavefunction. Since the total wavefunction is a product of the spatial and spin wavefunctions, one must be symmetric and the other anti-symmetric. The two possibilities for spatial wavefunction can be written as:

$$\Phi(r_1, r_2) = \frac{1}{\sqrt{2}} \left[\phi_1(r_1)\phi_2(r_2) \pm \phi_1(r_2)\phi_2(r_1) \right] \tag{2.25}$$

where the sum combination is the symmetric state and the difference combination is the antisymmetric state. The spin wavefunction has 4 possibilities, three symmetric and one antisymmetric:

$$\text{Symmetric:} \qquad \sigma(r_1, r_2) = \begin{cases} \sigma_\uparrow(r_1)\sigma_\uparrow(r_2) \\[2mm] \sigma_\downarrow(r_1)\sigma_\downarrow(r_2) \\[2mm] \frac{1}{\sqrt{(2)}} \left[\sigma_\uparrow(r_1)\sigma_\downarrow(r_2) + \sigma_\uparrow(r_2)\sigma_\downarrow(r_1) \right] \end{cases} \tag{2.26}$$

$$\text{Antisymmetric:} \qquad \sigma(r_1, r_2) = \frac{1}{\sqrt{2}} \left[\sigma_\uparrow(r_1)\sigma_\downarrow(r_2) - \sigma_\uparrow(r_2)\sigma_\downarrow(r_1) \right] \tag{2.27}$$

This implies that the spatial wavefunction of two electrons in the same spin state must be antisymmetric, since their spin wavefunction is symmetric.

The exchange interaction plays a role in determining whether a particular atom is magnetic. To make such a determination, we need to know an atom's ground state. It is not immediately

obvious how to do this. A cobalt 2+ atom, for example, has 7 valence electrons that must be distributed in 5 $3d$ orbitals: there are 120 possibilities! Friedrich Hund developed phenomenological rules for determining the electronic ground state of an atom that obeys the Russel-Suanders coupling scheme. Hund's three rules are:

(1) Electrons minimize their Coulomb interaction by avoiding each other, and the exchange interaction then tends to align their spins.

(2) The orbital angular momentum must be maximized.

(3) The spin and orbital angular momenta must be parallel. This means that if the valence shell is less than half filled, $J = |L - S|$. If the shell is more than half filled, $J = L + S$. If the shell is exactly half filled, $J = S$.

An element's magnetic moment is proportional to its total electron angular momentum J, as described in Equation 2.21.

In order to determine whether individual magnetic atoms will form ferromagnetically ordered solids, let us now consider the energy of the Coulomb interaction between an electron and a nucleus:

$$H_{en} = -\frac{Ze^2}{4\pi\varepsilon_0 r_{12}} \tag{2.28}$$

where Z is the atomic number, e is the electron charge, ε_0 is the permittivity of free space, and $r_{1,2}$ is the distance between the electron and the nucleus. When the electron is near to the nucleus, its energy is low, and its energy increases the further the electron is from the nucleus.

We can now create an intuitive picture of this exchange interaction by combining the Coulomb interaction with the Pauli principle. If the nuclei are close together, a symmetric spatial wavefunction allows an the electron to stay close to both nuclei, minimizing the Coulomb energy - this requires the spin wavefunction to be antisymmetric, meaning the spins must be anti-aligned. If the nuclei are further apart, an antisymmetric wavefunction allows the electron to be closer to both nuclei, minimizing the Coulomb energy - this requires the spin wavefunction to be symmetric,

meaning the spins must be aligned. *Read this paragraph and study the diagram in Figure 2.2 as many times as necessary. This is a crucial point that lies at the very heart of magnetism in all condensed matter systems.*
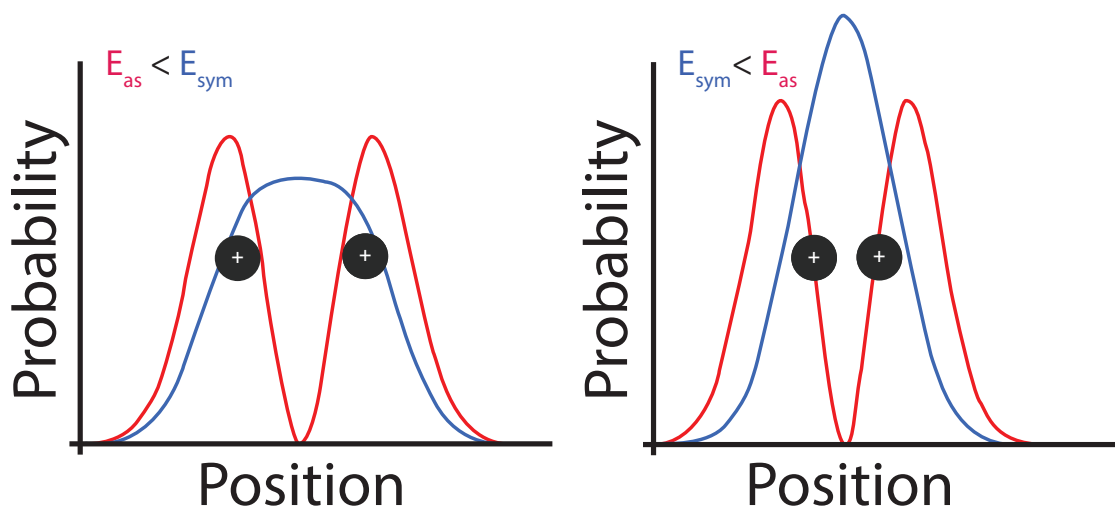
Figure 2.2: **The interatomic exchange interaction.** The black circles are the positions of the nuclei, the red lines are the positions of the electrons in antisymmetric spatial wavefunctions, and the blue lines are the positions of the electrons in symmetric spatial wavefunctions. When the nuclei are far from each other, the electron has a higher probability of being close to the nuclei in an antisymmetric spatial wavefunction (the area under the red line has more overlap more with the black circles). When the nuclei are close, the electron has a higher probability of being close to the nuclei in a symmetric spatial wavefunction (the area under the blue line has more overlap more with the black circles). The symmetry of the spin wavefunction must be opposite the symmetry of the spatial wavefunction, since the total wavefunction must be antisymmetric. This figure was adapted from [6].

In summary, electrons will act to minimize the energy of their Coulomb interaction with their neighboring nuclei. This can occur in a spatially symmetric *or* antisymmetric wavefunction, depending on the nuclear separation. Once the symmetry of the spatial wavefunction is determined, the symmetry of the spin wavefunction follows. Heuristically, this lets us determine the type of

magnetic order that appears in a given material.

An atom is magnetic if it has many unpaired electrons. This occurs in many materials, but such materials are often paramagnetic, meaning that their net magnetization is simply proportional to an applied external field and they maintain no magnetization in the absence of an applied field. For paramagnetic materials, the exchange interaction between atoms is not large enough to overcome thermal fluctuations and spontaneously form magnetic order. Magnetic materials, like the $3d$ transition metals Cr, Mn, Fe, Co, and Ni have large exchange energies and a relatively large nuclear charge that pulls the electrons in the poorly shielded $3d$ orbitals closer to their own nucleus, preventing them from bonding with other atoms. The electrons in these poorly shielded and more localized orbitals have a symmetric spin state (meaning their spins are aligned) in order to satisfy the antisymmetry requirement of fermionic wavefunctions. This can be contrasted with a material like carbon, where its covalent bonds are a symmetric spatial wavefunction with an antisymmetric spin wavefunction that is therefore non-magnetic. Some 4f metals are also magnetic because the 4f orbitals, like the $3d$ orbitals, are poorly shielded from the nuclear charge, causing them to localize, making them ineffective at bonding, making them spatially antisymmetric and spin symmetric.

Once we have a material made of magnetic atoms with a strong enough exchange interaction to form long range magnetic order, the magnetic moments of those atoms will align if their nuclear separation is far enough. If their nuclei are too close, the magnetic moments of those atoms will be anti-aligned. These states are called *ferromagnetic* and *antiferromagnetic*. We can see the effect of this nuclear separation in real materials by examining the *Bethe-Slater curve* in Figure 2.3 below. This model successfully predicts the magnetic ordering of $3d$ transition elements, as Cr and Mn have the closest packing and are antiferromagnetically ordered, and Fe, Co, and Ni are ferromagnetically ordered.
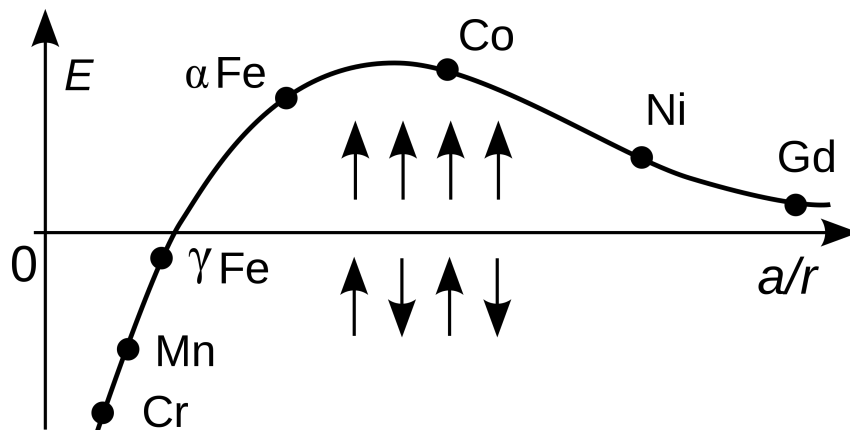
Figure 2.3: **The Bethe-Slater curve, which shows how the magnetic ordering of materials switches from antiferromagnetic to ferromagnetic as their interatomic spacing increases.** Note that γFe is a face centered cubic (fcc) ordering of iron with a smaller interatomic distance than αFe which is body centered cubic (bcc). This γFe ordering is not commonly encountered because it occurs when Fe is heated above 912 °C.

We can formalize our intuitive understanding of the exchange interaction in materials into an expression of the exchange energy:

$$H_{ex} = -J_{ex}\hat{S}_1 \cdot \hat{S}_2 \tag{2.29}$$

where J_{ex} is called the exchange integral, and $\hat{S}_{1,2}$ are the spin operators for each electron. The details of exchange integral depend on the specific system under consideration, but the spins will align if it is positive and anti-align if it is negative. Having discussed the origins of magnetism and magnetic ordering, we are ready to move on to modelling magnetism in metals and the associated challenges of understanding magnetism when the electrons that contribute strongly to the magnetic moment are delocalized.

2.2   Modeling magnetic materials

In both metals and non-metals, the Heisenberg and Ising models of magnetism allows us to describe the alignment of individual, localized, magnetic moments and successfully predicts

phenomena like the temperature dependence of magnetization and the magnetic susceptibility, including critical points and magnetic order phase transitions. The Heisenberg model does not consider the important role that delocalized electrons play in the properties of metals and requires that each spin stay localized to a single site.

The Stoner model, in contrast, takes into account the delocalized nature of electrons in metals. This model approximates magnetism with a non-interacting system of electrons to calculate a band structure and density of states (DOS) and then shifts the energy of the DOS for the spin-up electrons relative to the spin-down electrons by an amount called the "exchange splitting". The magnetism is then assumed to be proportional to the spin polarization of the total number of filled states. While this model accurately predicts the strength of metallic feromagnets and is useful for studying the behavior of electrons in magnetic materials near the Fermi energy, it unfortunately fails entirely to accurately predict magnetic phase transition temperatures. Both models are needed to accurately predict magnetic behavior in real systems.

2.2.1 The Ising model and the mean-field model

In the Ising model, we consider a lattice of identical spins, where each spin is constrained to its own site. The Hamiltonian for this system can be written as:

$$H_{IS} = -\sum_{i,j} J_{i,j} \hat{s}_i \cdot \hat{s}_j \tag{2.30}$$

where

$$J_{i,j} = \begin{cases} J \text{ if i, j are neighbors} \\ 0 \text{ otherwise} \end{cases} \tag{2.31}$$

In this model, $J_{i,}$ is normally assumed to be a model parameter because of the difficulty of evaluating the exchange integral in real solids. $J_{i,j}$ is also assumed to exist only for nearest neighbor interactions. We can make an additional simplifying assumption that a spin interacts with the average magnetic field produced by its neighbors, rather than each individual neighbor:

$$\hat{s}_i \cdot \hat{s}_j \rightarrow \hat{s}_i \cdot \langle \hat{s} \rangle \tag{2.32}$$

This allows us to write the mean-field Hamiltonian:

$$H_{MF} = -\sum_i \hat{s}_i \cdot zJ \langle \hat{s} \rangle \tag{2.33}$$

where z is the number of nearest neighbor atoms, called the *coordination number*. We can then define an effective field:

$$B_{MF} = \frac{z}{\mu_B} J \langle \hat{s} \rangle \tag{2.34}$$

This effective field, also called the Weiss field, is 100s of T for $3d$ transition metals. The energies of the possible magnetic states in this field are:

$$E_{\pm} = -\mu \cdot B_{MF} = \mp \mu_B B_{MF} \tag{2.35}$$

We can now find the fraction of spins in each orientation using the Boltzmann distribution:

$$\frac{N_{\uparrow}}{N} = \frac{\exp\left(\frac{\mu_B B_{MF}}{k_B T}\right)}{\exp\left(\frac{\mu_B B_{MF}}{k_B T}\right) + \exp\left(\frac{-\mu_B B_{MF}}{k_B T}\right)} \tag{2.36}$$

$$\frac{N_{\downarrow}}{N} = \frac{\exp\left(\frac{-\mu_B B_{MF}}{k_B T}\right)}{\exp\left(\frac{\mu_B B_{MF}}{k_B T}\right) + \exp\left(\frac{-\mu_B B_{MF}}{k_B T}\right)} \tag{2.37}$$

$$\tag{2.38}$$

where $N_{\uparrow}$ is the number of spin up electrons, $N_{\downarrow}$ is the number of spin down electrons, N is the total number of electrons, k_B is Boltzmann's constant, and T is the temperature. The magnetization per unit volume is:

$$\boldsymbol{M} = n\mu \tanh\left(\frac{\mu B_{MF}}{k_B T}\right) \tag{2.39}$$

where n is the number of magnetic moments per unit volume. Equation 2.39 is called the self-consistent equation of state for M because M depends on B_{MF}, which in turn depends on M. While this may seem circular, it will allow us to derive the temperature dependent properties of ferromagnets. In particular, we will define the saturation magnetization $M_S = n\mu_B$ and the critical temperature $T_c = zJ/k_B$. We can now simplify Equation 2.39 to:

$$M = M_s \tanh\left(\frac{T_C}{T} \frac{M}{M_s}\right) \tag{2.40}$$

and by further parameterizing this equation with $m = M/M_s$ and $t = T/T_c$, we obtain:

$$m = \tanh\left(\frac{m}{t}\right) \tag{2.41}$$

If we solve this transcendental equation numerically, we obtain the following behavior for the magnetization fraction m as a function of temperature:
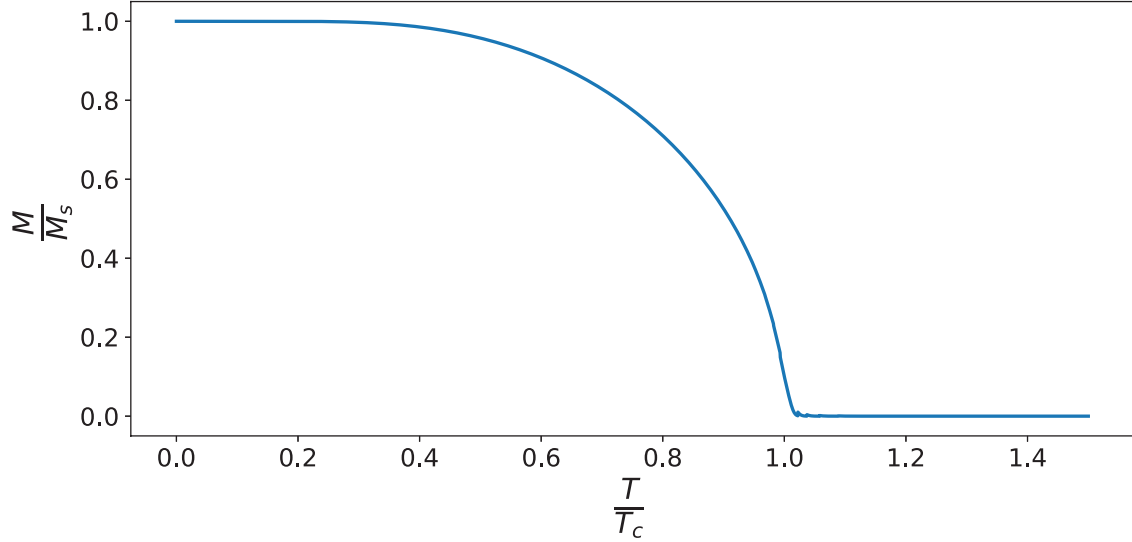
Figure 2.4: **Magnetization fraction as a function of temperature in the mean-field model.**

We can see clearly that at the critical temperature, the magnetization fraction drops to zero. The material will not spontaneously magnetize beyond this temperature. In ferromagnets, this critical temperature is called the *Curie temperature*, below which the material is ferromagnetic. A ferromagnetic material's magnetic susceptibility χ is given by the *Curie-Weiss law*:

$$\chi = \frac{C}{T - T_c} \tag{2.42}$$

where C is the material specific Curie constant:

$$C = \frac{\mu_0 \mu_B^2}{3k_B} n g_J^2 J(J+1) \tag{2.43}$$

where μ_0 is the permittivity of free space, μ_B is the Bohr magneton, k_B is Boltzmann's constant, n is the number of magnetic moments per unit volume, g_J is the Landé g-factor, and J is the

total angular momentum of the atom. In this expression for the magnetic susceptibility, we can see that it it diverges near the critical temperature as long range interactions become increasingly important because the energy scale of thermal fluctuations exactly matches the energy scale of spin realignments.

Throughout this derivation we have made one additional assumption that J is positive, meaning that aligned spins are a lower energy configuration than anti-aligned. If J is negative, then anti-aligned spins are the lowest energy configuration and there is no spontaneous net magnetic moment at any temperature - the material will be antiferromagnetically ordered. Antiferromagnets also have a critical temperature called the *Neél Temperature*, below which they are antiferromagnetic.

The Heisenberg model does a good job of predicting the temperature dependent behavior of magnetic materials, but it is unable to predict the strength of the magnetic moments within those materials. This is because it does not take into account the delocalized nature of electrons in metallic magnets. In order to accurately determine the strength of metallic ferromagnets, we turn to the Stoner model of magnetism.

2.2.2   Stoner magnetism and the density of states

In a metallic system, electrons are not well localized and instead can travel throughout the material. To understand how this is possible, let us consider N atoms arranged into a crystal. In an individual atom, the energy levels of electrons are discreet and well defined. When an atom bonds with its neighbors, the original orbital is hybridized into new orbitals, and its corresponding orbital energy levels are also adjusted. There will be N new hybrid orbitals, spaced by $\sim 1/N$ eV. In a macroscopic system where there are on the order of 10^{22} atoms, the energy levels of these new, hybrid orbitals will be spaced by 10^{-22} eV. These very tightly packed orbitals can be approximated as a continuous "band" of energies. After making the assumption that the energies levels within a given band are continuous, we can then define a density of states, which describes how many states

are available for an electron at a given energy:

$$g(E) = \frac{dN}{dE} \tag{2.44}$$

The exact form of the density of states depends on the material in consideration. Note that these states do not need to be occupied, although they can be; they simply need to be available.

Once we have defined the electronic bands, we can discuss the thermodynamic properties of electrons within those bands. The probability of a state with an energy E being occupied by an electron is given by the Fermi-Dirac distribution:

$$f(E) = \frac{1}{e^{(E-E_F)/(k_B T)} + 1} \tag{2.45}$$

where E_F is the Fermi energy, k_B is Boltzmann's constant, and T is the temperature in Kelvins. There is exactly a 50% chance of an electron occupying a state with the Fermi energy E_F, by definition. At 0 K, all energy states below E_F are filled, and none above E_F are filled. As the temperature increases, the slope of the Fermi-Dirac distribution near E_F decreases, allowing more states above E_F to be occupied while reducing the occupation below E_F. The width of the sloped portion of the Fermi-Dirac distribution is $\sim k_B T$. The Fermi-Dirac distribution at various temperatures is shown in Figure 2.5 below:
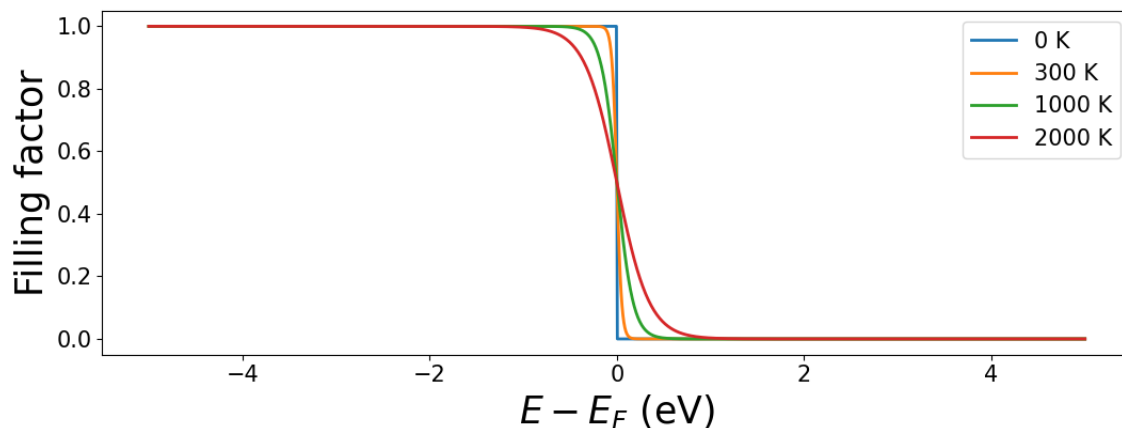
Figure 2.5: **Fermi-Dirac distribution at various temperatures, assuming $E_F = 11.1$ eV (the Fermi energy of Fe).** At room temperature ($\sim$300 K), the occupation is very similar to that at 0 K.

Depending on how the energy levels of the original atom hybridize, multiple bands can be formed, and these bands may have a large energy spacing between them, a small energy spacing, or they can overlap. We can understand the difference between metals, insulators, and semiconductors by considering the location of the Fermi energy relative to the material's band structure. If there is a large density of states at the Fermi energy, the material is a conductor. If there is no density of states at the Fermi energy, the material is an insulator. If there is no density of states at the Fermi energy but there are states available nearby, the material is a semiconductor.
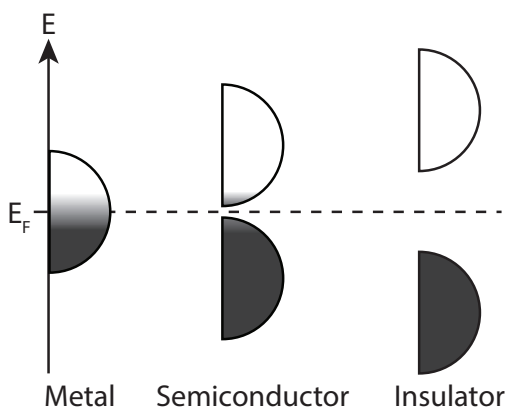
Figure 2.6: **Cartoon depiction of the density of states for metals, semiconductors, and insulators near the Fermi energy.** In a metal, the valence and conduction bands are joined and electrons can flow freely in the material. In a semiconductor, small excitations can promote electrons across the band gap, allowing them to conduct. In an insulator, the band gap is large and there is no conduction at low temperatures.

With the band structure description of metals in hand, we are ready to understand how the delocalized, or itinerant, electrons in $3d$ transition metals can give rise to magnetism. We consider the case of a material with an equal number of spin up and spin down electrons. If the density of states for up and down electrons are shifted relative to each other, a difference in the total occupancy of spin up and spin down electrons leads to a net spin polarization, which causes the material to be magnetic. We now ask the questions: why would the band structure spontaneously

form a net spin polarization? Under what circumstances is it energetically favorable to "split" the density of states of the spin up and spin down electrons?
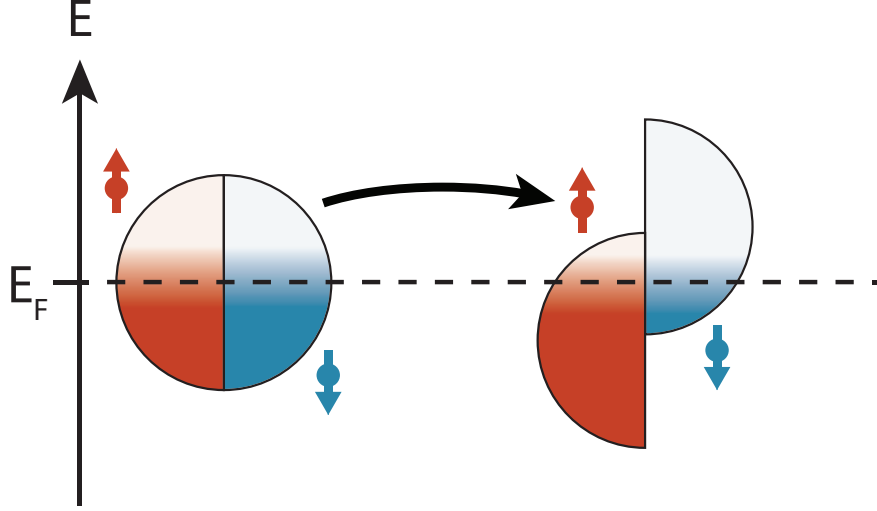
Figure 2.7: **Band splitting of the up and down electrons in the Stoner model of magnetism.** After the splitting occurs, there are more spin up electrons than spin down electrons and the material is magnetized.

We can write the total energy of our system as the sum of a kinetic energy term and an interaction term:

$$E = E_K + E_U \tag{2.46}$$

with

$$E_K = \int_E g(E) f(E) dE \tag{2.47}$$

$$E_U = J \left[\int_E g_\uparrow(E) f(E) \right] \left[\int_E g_\downarrow(E) f(E) \right] \tag{2.48}$$

where $g(E)$ is the density of states at a given energy E, $f(E)$ is the filling factor given by the Fermi-Dirac distribution, J is the exchange integral, and $g_\uparrow(E)$, $g_\downarrow(E)$ are the density of states for spin up and spin down electrons, respectively. If we consider an infinitesimal band splitting of δE, the kinetic energy increases by:

$$\Delta E_K = g(E_F)(\delta E)^2 \tag{2.49}$$

and the exchange energy decreases by:

$$\Delta U = -Jg^2(E_F)(\delta E)^2 \tag{2.50}$$

giving us a total energy change of:

$$\Delta E = g(E)(\delta E)^2 \left[1 - Jg(E_F)\right] \tag{2.51}$$

If Equation 2.51 is negative, the bands will spontaneously split and the material will be ferromagnetic. We can write the condition under which this occurs, called the *Stoner criterion*:

$$Jg(E_F) > 1 \tag{2.52}$$

This indicates that in order to have ferromagnetic order in a metal, we must have sufficient density of states at the Fermi energy and a sufficiently large exchange interaction. For the $3d$ transition metals, only Fe, Ni, and Co have a Stoner criterion greater than one. Since the Stoner model defines the magnetism as the total spin polarization, fractional magnetic moments are possible. This agrees with measurements of the average magnetic moment in bulk metals. Unlike the Heisenberg model, however, the Stoner model predicts critical temperatures for 3d transition metals that are several thousand K [7]. Why are these predicted temperatures so different than the actual transition temperatures which are well predicted by the Heisenberg model? The answer lies in the fact that the exchange energy refers to a slightly different quantity in each model of magnetism.

2.2.3   Revisiting the meaning of the exchange interaction

The exchange interaction has three different meanings depending on whether it is referring to the singlet-triplet intra-atomic exchange interaction, the inter-atomic exchange interaction in the mean field model, or the Stoner exchange interaction. In a two-electron atom, we can interpret the exchange energy as the energy cost of flipping one electron. In the mean-field model, the exchange energy is the energy cost of flipping the magnetic moment of an entire atom. In the Stoner model, the exchange energy is the energy cost of flipping a single spin in a sea of delocalized electrons. These different scenarios are illustrated below in Figure 2.8:

Single Atom Exchange

Singlet-triplet
exchange

~1 eV

Mean-Field Exchange

Atomic
moment
reversal

~0.2 eV

Stoner Exchange

Single spin
reversal

~1 eV
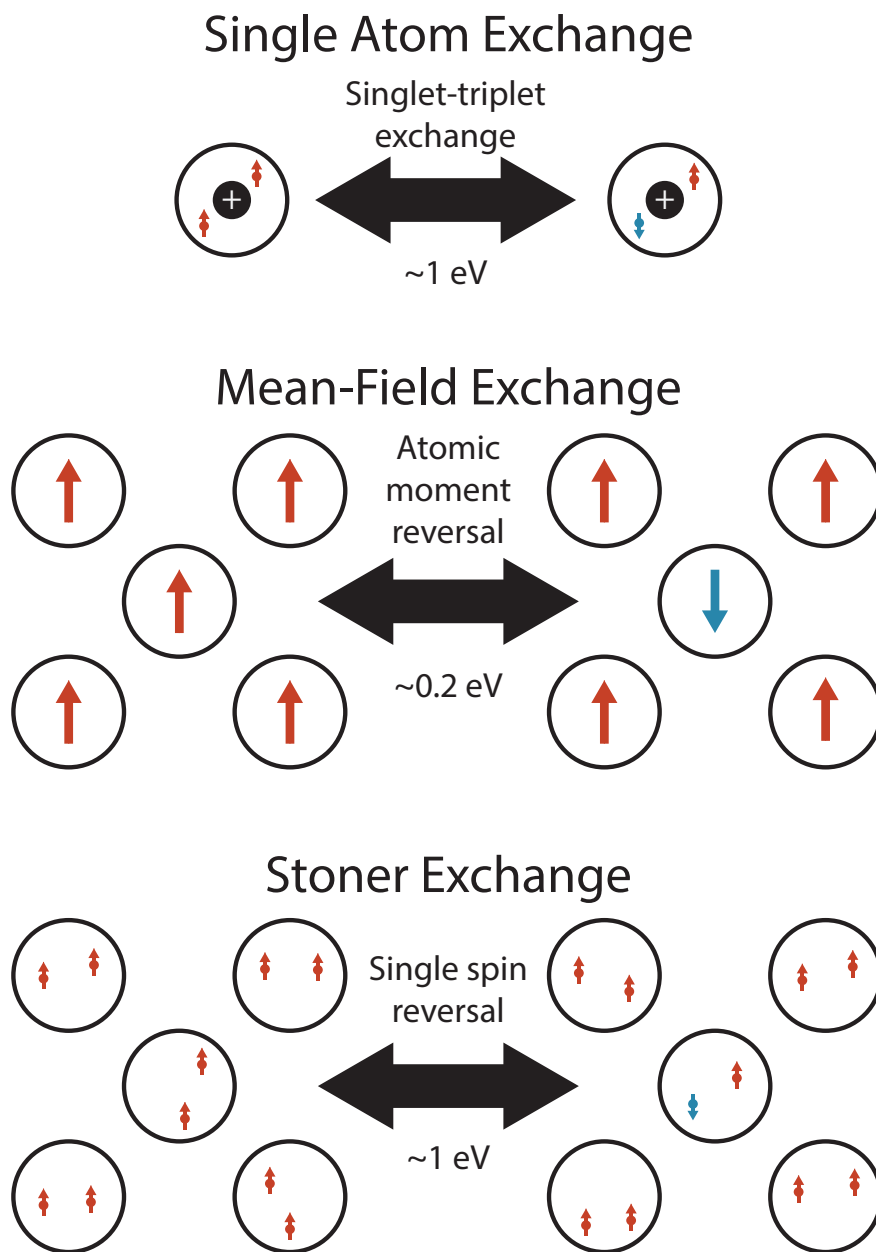
Figure 2.8: **Illustration of the three different types of exchange interaction.** Figure adapted from [5].

With these differences in mind, we can clearly see that the exchange energy in the Stoner model and the exchange energy within a single atom are similar to each other and dissimilar and the exchange energy between neighboring atomic sites in the mean-field model. Why are the Stoner and mean-field exchange energies so different? For a given electron spin in the Stoner model, the

intra-atomic Coulomb interactions are large and responsible for most of the exchange energy; as the distance from a given spin increases, other Coulomb interactions are screened by delocalized s-p conduction electrons in the metal and therefore do not contribute strongly to the exchange energy. In the mean-field model, by contrast, the entire atom's magnetic moment flips and there are no screening conduction electrons.

Understanding of how the exchange interaction differs in different models of magnetism gives us intuition about the behavior of ferromagnets. We can see why the Curie temperatures predicted by the mean-field and Stoner models are so different: the mean-field model exchange energy is the energy required to flip an entire atom's magnetic moment; this is considerably less than the energy to flip a single spin within that atom (as is required in the Stoner model). This energy difference also explains why the local moments of atoms persist at temperatures well above the Curie temperature, as evidenced by their paramagnetic susceptibility (the temperature dependent proportionality constant with which a material's internal magnetic field aligns with an external field). Presumably at extremely high temperatures, the spins within the atoms will also become disordered and the atoms will lose their local moments, although this has not been experimentally observed. In summary, *the Stoner exchange energy is the energy of local magnetic moment formation and the mean-field exchange energy is the energy of long range magnetic order formation.*

2.3   Magnetic excitations

Magnetic excitations can be divided into Stoner excitations and Heisenberg excitations. A Stoner excitation is simply a single electron spin flip. Such an excitation changes the system's angular momentum by $\Delta s_z = \hbar$ and its energy by the Stoner exchange energy (~ 1 eV, as discussed in previously in section 2.2.3). Since these excitations are very high energy, they cannot be responsible for the changes in magnetization below T_c shown in Figure 2.4. In order to find the excitations responsible for the $T < T_c$ changes in magnetism, we will return to the mean-field model, and then generalize back to the Stoner model.

In the Weiss mean-field model of localized magnetic moments, we can define a collective

excitation of spins called a *magnon*. These magnons are spin waves with quantized angular momentum. A magnon can be viewed as a synchronized precession of spins on different sites with a uniform phase shift between adjacent sites, just as a phonon can be viewed as a synchronized position oscillation of atomic nuclei with a phase shift.

N-1   N   N+1
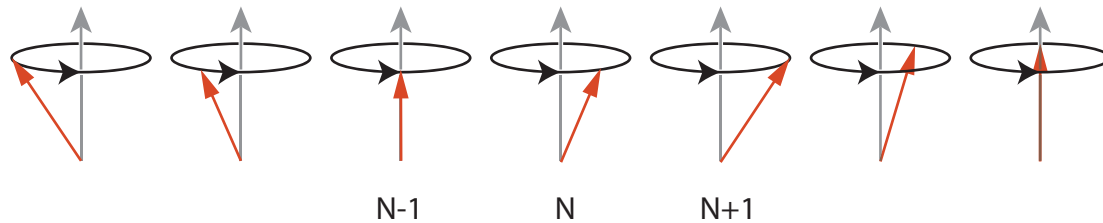
Figure 2.9: **Spin wave in a 1-dimensional spin chain.**

In effect, a magnon allows us to distribute the excitation of a single spin flip over multiple lattice sites. The less localized the magnon is (meaning that more spins are participating), the lower its energy. This means that arbitrarily small magnon energies are possible by recruiting more lattice sites to participate. In the limit of very short wavelength magnons, the magnon becomes a single spin flip and its energy is equal to the exchange energy in the mean-field model.

While their energy is allowed to vary with the number of spins participating in the collective behavior, magnons always carry an angular momentum of $\hbar$. Because they have integer spin, magnons are bosons and obey boson statistics, like photons or phonons. Since they obey boson statistics, multiple magnons are allowed to exist in the same state. This implies that at non-zero temperatures, all the thermal energy could go into low energy magnon formation and immediately destroy the magnetic order! Why does this not occur? There is an energy gap generated by the magnetic anisotropy (a preferential direction of magnetization) that prevents long range magnon formation - this is the result of the *Mermin-Wagner theorem.*

Now that we have addressed magnon formation in the mean-field model, we can generalize it to the Stoner model. In the mean-field model, a *whole atom* spin flip is distributed over multiple lattice sites. In the Stoner model, we can distribute a *single electron* spin flip over multiple lattice

sites. Practically, this simply increases the upper bound on the energy which a magnon can carry, increasing it from ~ 0.3 meV to ~ 1 eV. The low energy bound allowed by the magnetic anisotropy allows remains unchanged. In summary, magnetic excitations always carry angular momentum $\hbar$, but they exist on a continuum between long wavelength spin waves and single electron spin flips with energies ranging from ~ 0 to 1 eV.

2.4 Ultrafast electronic excitation

When a laser pulse is incident on a magnetic material, electrons can be promoted from their ground state below the Fermi to an excited state above the Fermi energy. This transition is modeled as an electric dipole transition from an initial state $|i\rangle$ to a final state $|f\rangle$. The transition probability per unit time Γ between these two states is given by Fermi's golden rule:

$$\Gamma_{i \to f} = \frac{2\pi}{\hbar} \left| \langle f | H' | i \rangle \right|^2 g(E_f) \tag{2.53}$$

where $\langle f | H' | i \rangle$ is the matrix element of the driving laser field perturbation between the initial and final states, and $g(E_f)$ is the density of states at the energy of the final state E_f.

During the laser pulse and immediately after the laser pulse arrival, the electrons are in a highly non-equilibrium, non-thermal distribution, as shown below:
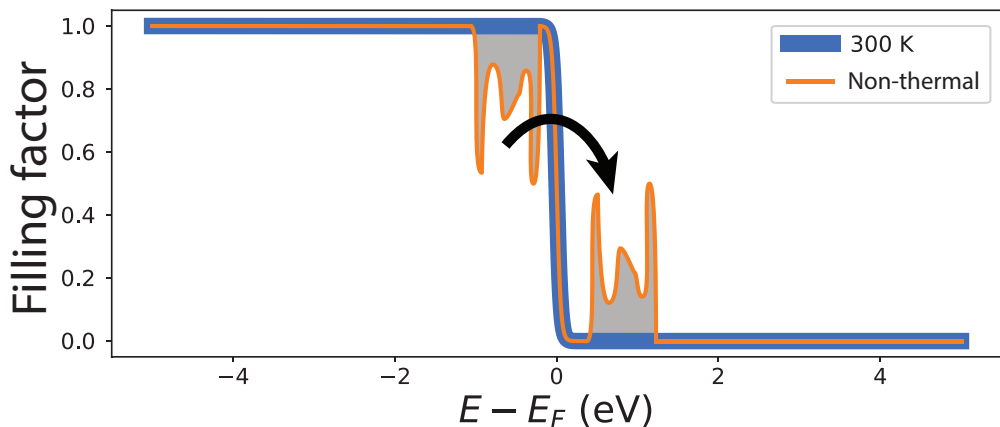
Figure 2.10: **The filling factor in a hypothetical material before and after an incident laser pulse.** The black arrow shows the transition and the shaded regions indicate initial and final states of the transition. The excitation shape is a function of the laser spectrum, the density of initial states, and the density of final states.

Figure 2.10 shows a cartoon of how the filling factor based on the Fermi-Dirac distribution would change after laser excitation. The exact shape of the excitation depends on the density of states in the material's ground state and the photon energy of the incident laser pulse. Once this non-equilibrium electron distribution is formed, the electrons will thermalize via electron-electron scattering and form a new Fermi-Dirac distribution with a higher temperature. In this thesis we will only consider electric dipole transitions, although magnetic dipole transitions (where the laser pulse's magnetic field couples directly to the electron spin) are also possible.

This very simple understanding of how a laser excitation interacts with a material will give us a starting point to understand ultrafast magnetism. The fastest timescale in this experiment is the direct interaction between the electrons and the laser pulse, and other interactions will allow for the transfer of energy and angular momentum between the excited electrons and other systems.

2.5   Ultrafast magnetic interactions

At this point, we have discussed the origins of magnetism and various ways to model it in real materials. We now turn our attention to ultrafast magnetic interactions that are relevant to

non-equilibrium magnetic processes. Understanding these interactions and their associated length and time scales will help us to understand the complex behavior of ultrafast magnetic dynamics in real systems. In 1996, Beaurepaire first observed that the ultrafast demagnetization of Ni occurred on a sub-picosecond timescale after excitation with an ultrafast laser pulse [8]. This was surprising because: (1) electric dipole transitions preserve electron spin polarization and (2) the only known mechanisms to transfer angular momentum into or out of the spin system involved coupling the electrons to the lattice, and the spin-lattice relaxation timescale was known to be 10s or 100s of picoseconds [9, 10, 11, 12]. In order to demagnetize a ferromagnet, the spins must become disordered, meaning that the angular momentum of the spin system must change. We will consider both the energy balance and angular momentum balance of the spin system, since these quantities must be globally conserved (although they are not conserved *within* the spin system). In particular, we will look at fundamental interactions that allow the angular momentum of the spin system to change, since magnetism is fundamentally angular momentum. A change in angular momentum can happen in three ways - it can be:

(1) transferred between electron spins and the lattice

(2) transferred between electron spins and other electron spins

(3) removed from the area under observation

Each of these can occur in ultrafast demagnetization and can occur on ultrafast timescales. Electron spin angular momentum can be exchanged with the lattice, and this can occur on femtosecond timescales, despite earlier beliefs to the contrary. Electron spin angular momentum can be transferred to other electron spins via magnon generation and spin-flip exchange scattering. Finally, the electron spin can be removed from the area under observation by superdiffusive spin currents or by moving from one element to another in a compound. We will consider each of these interactions in turn.

2.5.1   Electron spin to phonon angular momentum transfer

In Elliott-Yafet spin scattering [13, 14], electrons have a probability of flipping their spin in each scattering event because spin-orbit coupling mixes the spin up and spin down states, making the electron spin no longer a good quantum number - each scattering event thus changes the electron's momentum and therefore its spin mixture. This occurs even though the spin mixing is generally small. Elliott-Yafet scattering involves electrons scattering from non-magnetic defects and phonons. The spin-orbit coupling of the electrons can be modified by lattice vibrations. Thus, there is an interaction between electron spin and phonons, i.e. quantized lattice vibrations.
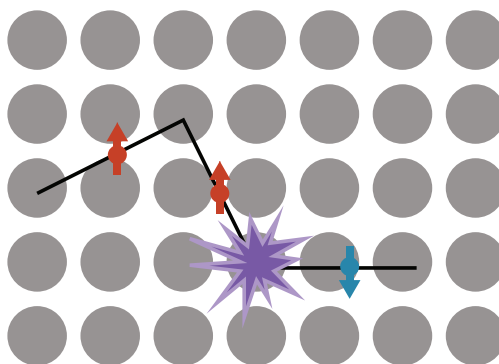
Figure 2.11: **Cartoon of Elliott-Yafet scattering.** The electron scatters off of acoustic phonons or lattice defects, and each scattering event has a small probability of flipping the electron spin due to spin-orbit coupling.

In the electron-phonon Elliott-Yafet scattering process, the spin precession rate exceeds the scattering rate, and thus the spin relaxation time (the timescale of an electron spin flip) is proportional to the electron-phonon scattering rate. This spin relaxation time has been measured to be roughly 50 fs in nickel at room temperature [15].

Importantly, single electron spin flip processes change the total angular momentum in the spin system by changing a material's total spin polarization. Since angular momentum must be conserved, this angular momentum must be transferred into a different degree of freedom. In Elliott-Yafet scattering, the angular momentum is transferred into the lattice.

There are other ways for the spin system to exchange angular momentum with the lattice. In the presence of spin-orbit coupling that mixes spin up and spin down channels, *any* momentum dependent scattering event can change the spin mixture and therefore flip an electron spin. Electron-electron Coulomb scattering in the presence of spin-orbit coupling is inelastic because scattering events can dissipate angular momentum into the phonon bath [16]. In this way, electron-electron scattering also become a spin angular momentum dissipation channel and can act on much faster timescales than electron-phonon scattering. A different channel for transferring electron spin angular momentum to phonons involves the valence-electron localization during the first 120 fs after an intense laser pulse; the valence electron localization changes the spin-orbit interaction, just as phonons can change the spin-orbit interaction [17]. These alternate channels open the possibility to transfer angular momentum from the electron spins to the phonon system on a time scale much faster than the spin-lattice relaxation time of 10-100 ps.

2.5.2 Electron-electron angular momentum transfer

One method for electron-electron angular momentum transfer is scattering on spin waves, whereby a minority electron can flip its spin to a majority spin, exciting a spin wave (or magnon). The reverse can also occur: a majority electron can flip its spin to a minority spin, absorbing a spin wave. The spin-flip time t_{sf} is inversely proportional to the energy of the spin wave E_{sw}, which itself is proportional to the square of the spin wave vector $q = 2\pi/\lambda$, giving us $t_{sf} \propto E \propto q^2$. The magnon wavelength λ cannot be shorter than the lattice constant, giving us an upper bound on the timescale of spin wave scattering. At room temperature, a typical timescale for spin wave scattering is ~ 300 fs [5, Chapter 12.7.1].

Another method for electrons to transfer angular momentum between themselves is spin exchange scattering. In this process, the indistinguishability of electrons can allow for two electrons to effectively "trade places", while appearing that the spins of the original electrons have flipped. (In fact, indistinguishability means there is no meaningful way to refer to the "original" electron - these two pictures are completely identical.) The time scale for this process is typically on the

order of ~ 1 fs [5, Chapter 12.7.2].
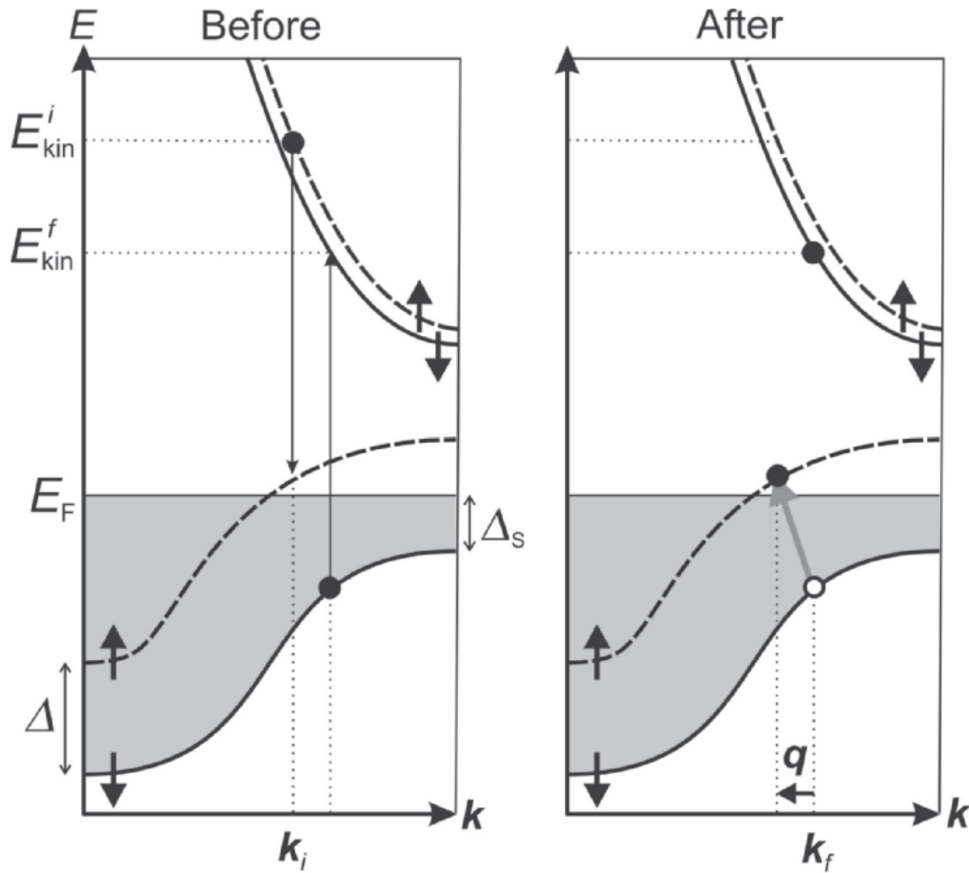
Figure 2.12: **Spin exchange scattering.** An incident spin up electron can drop into an unoccupied $3d^{\uparrow}$ state, exciting an occupied $3d^{\downarrow}$ state. In this exchange scattering interaction, there is an energy loss $E_{kin}^{i} - E_{kin}^{f} \approx \Delta$ and a momentum change $\mathbf{q} = \mathbf{k_i} - \mathbf{k_f}$. Figure adapted from [5, Chapter 12.7.2].

While this process is very fast and may play a role in ultrafast magnetization dynamics, different experiments offer dramatically different estimates for the likelihood of spin exchange scattering. If the exchange scattering rate is high, spins should easily flip into the opposite spin state, causing their lifetimes and scattering lengths to equilibrate. Experiments on the lifetime ratios of majority to minority spins in Co show that the spin lifetimes are similar near the Fermi energy and diverge as the energy increases [18, 19]. Experiments on the spin dependent scattering length in $Ni_{81}Fe_{19}$

show the opposite trend, where majority and minority spins have more similar lifetimes far above the Fermi energy that diverge as they approach the Fermi energy [20]. Although these different experimental approaches give different results as to whether the electron excited state lifetimes are spin dependent, I will assume in this thesis that *scattering lengths are spin dependent* because this spin dependent scattering length is the basis for spin polarized currents which have consistently been observed in a variety of ferromagnetic materials and will be discussed in the next section.

2.5.3   Superdiffusive spin currents

A superdiffusive spin current [21] is the transport of hot, spin polarized electrons (and a compensating flow of oppositely polarized, cooler electrons so that charge is conserved) that can occur immediately following the ultrafast excitation of a magnetic metal. This process is different from both ballistic and diffusive transport - for all isotropic transport processes, the size of the particle distribution σ^2 is a function of time:

$$\sigma^2 = t^\gamma \tag{2.54}$$

where $\gamma = 1$ for diffusive transport and $\gamma = 2$ for ballistic transport. In the superdiffusive transport regime described here, $2 \geq \gamma \geq 1$, where $\gamma = 2$ at short times and $\gamma = 1$ at long times, and thus transport evolves from ballistic to diffusive as the hot electrons cool.

This super diffusive spin transport can lead to demagnetization because of high velocities of the laser-excited electrons ($\sim$1 nm/fs) and because of a difference in excited state lifetimes for majority and minority electron spins. This lifetime difference leads to a long mean free path for majority electrons and a short mean free path for minority electrons, allowing for majority electrons to be depleted near the sample surface because they are transported away.

Superdiffusive spin transport has been measured in magnetic multilayers [22, 23]. In these materials, a stack of three materials are deposited on top of each other. A Ni thin film is at the top of the stack and an Fe thin film is at the bottom; in the middle is a non-magnetic conductor or an insulator. An ultrafast laser pulse is incident on the top of the stack and is absorbed as it

passes through the stack. This preferentially excites electrons near the top of the stack, though electrons towards the bottom are also excited. If the Ni and Fe layers are separated by a conductor, majority spins from the Ni pass through the conductor into the Fe, enhancing the magnetization of the Fe while reducing the demagnetization of the Ni. If the Ni and Fe layers are separated by an insulator, majority spins cannot travel from the Ni to the Fe, and both layers' magnetization is reduced. This behavior is shown below in Figure 2.13:
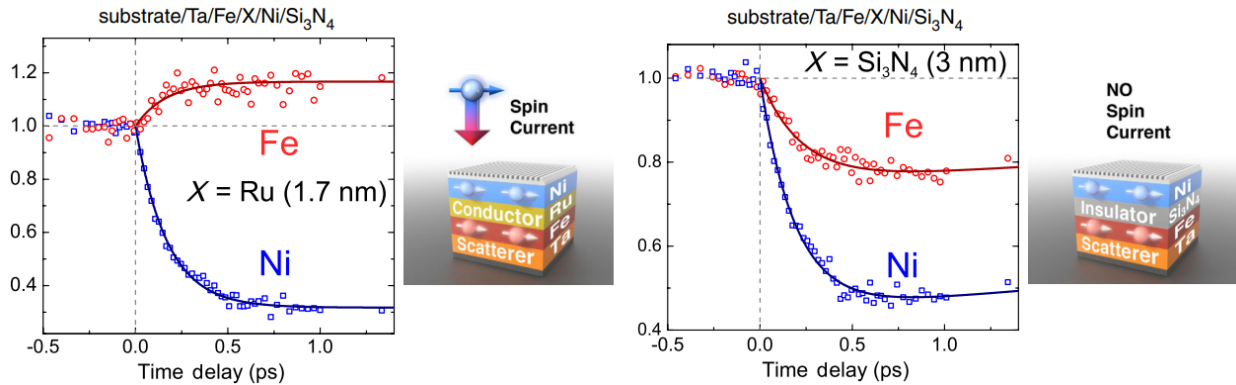
Figure 2.13: **Ultrafast demagnetization of ferromagnetic multilayers after laser excitation.** When the ferromagnetic Ni and Fe layers are separated by an electrically conductive Ru layer, majority spin currents from the Ni are transported into the Fe layer below. When the Ni and Fe layers are separated by an insulator, no spin current can occur. Figure adapted from [23].

2.5.4 Optically induced spin transfer (OISTR)

All of the ultrafast magnetic interactions discussed thus far are secondary interactions that occur after a laser pulse excites electrons from their ground state. The initial interaction between the laser and the material can be modeled as an electric dipole transition, whereby electrons are excited from their ground state below the Fermi energy to states above the Fermi energy (see Section 2.4). The timescale for this electric dipole transition sets the speed limit on any interaction between the laser pulse and the spin system - no faster interactions are possible without violating causality. In optically induced spin transfer (OISTR), a light pulse directly affects the material's spin system

because of electric dipole selection rules that enforce a spin polarized excitation. This direct optical control of the spin system occurs on the fastest possible timescale for the optical control of magnetic materials, making it a promising building block for future spintronic applications.

When a laser pulse is incident on a multi-element magnetic material, it is possible for a net transfer of magnetic moment from one elemental sublattice to another on very short timescales (< 10 fs) [24]. The OISTR occurs because of the structure of spin- and element-projected density of states (DOS) in certain compounds and alloys. To understand how a compound's DOS can allow for the transfer of spins from one elemental sublattice to another, let us consider the the spin- and element-projected DOS for Co_2MnGe:
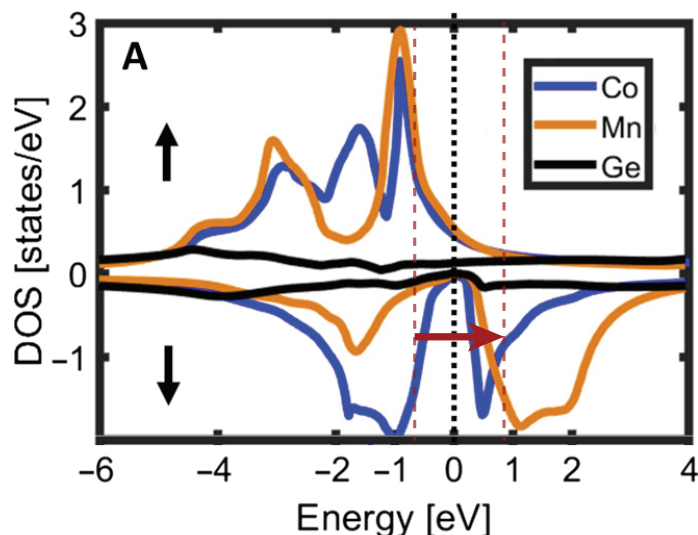
Figure 2.14: **Density of states for majority (up) and minority (down) spins for each element in Co_2MnGe.** The red arrow represents a 1.5 eV pump photon and the red dashed lines guide the eye to one set of possible initial and final states that can be excited by the 1.5 eV pump. Figure adapted from [25].

For the majority spins, there are few available states above the Fermi energy, which make optical transitions unlikely. For the minority spins, the occupied states just below the Fermi energy are predominantly Co in character, whereas the available states just above the Fermi energy are

primarily Mn in character. Since the optical transition will drive primarily minority spins from Co to Mn, this will *increase* the spin polarization of Co and *decrease* the spin polarization of Mn. As long as spin-orbit coupling is a relatively small portion of the material's net magnetization, the spin polarization is a good approximation of the magnetic moment. Thus, in Co_2MnGe, we see a net transfer of magnetization from Mn to Co as a result of excitation with an ultrafast laser pulse. In general, OISTR can occur between different elements if the ground state Fermi energy lies between d-states of different elements [24].

2.6   Maxwell's equations and the dielectric tensor

Having discussed the foundations of magnetism and the ultrafast magnetic interactions that can occur, we need tools to study these magnetic interactions. We will focus our attention on optical probes of magnetism, since only optical probes are capable of sub-picosecond measurements. To that end, we will discuss generic light-matter interactions and magneto-optical effects.

Electromagnetic dynamics are governed by Maxwell's equations, which can be written in SI units as:

$$\nabla \cdot \boldsymbol{D} = \rho_f \tag{2.55}$$

$$\nabla \cdot \boldsymbol{B} = 0 \tag{2.56}$$

$$\nabla \times \boldsymbol{E} = -\frac{\partial}{\partial t}\boldsymbol{B} \tag{2.57}$$

$$\nabla \times \boldsymbol{H} = \boldsymbol{J_f} + \frac{\partial}{\partial t}\boldsymbol{D} \tag{2.58}$$

where $\boldsymbol{E}$ is the electric field and $\boldsymbol{H}$ is the magnetic field, the fundamental fields in electromagnetism. ρ_f indicates the free charges, and Equation 2.56 refers to the fact that there are no magnetic monopoles (aka magnetic charges). $\boldsymbol{J_f}$ is the free current, and $\boldsymbol{B}$ is the magnetic induction.

We will pay special attention to the displacement field $\boldsymbol{D} = \varepsilon_0\boldsymbol{E} + \boldsymbol{P}$, which accounts for the polarization density $\boldsymbol{P}$ of the material; in a linear and homogenous dielectric, the polarization is directly proportional to the material's electric susceptibility $\hat{\chi}$ and to an applied electric field,

giving:

$$\boldsymbol{D} = \varepsilon_0 \boldsymbol{E} + \boldsymbol{P} \tag{2.59}$$

$$= \varepsilon_0 \boldsymbol{E} + \varepsilon_0 \hat{\chi} \boldsymbol{E} \tag{2.60}$$

$$= \varepsilon_0 (1 + \hat{\chi}) \boldsymbol{E} \tag{2.61}$$

$$= \hat{\varepsilon} \boldsymbol{E} \tag{2.62}$$

where $\hat{\varepsilon} = \varepsilon_0 (1 + \hat{\chi})$ is the permittivity of the medium, and this quantity is is also called the dielectric tensor. Note that we have not assumed the medium is isotropic; the polarization density can vary with direction. For a material magnetized along the z-direction, the elements of the dielectric tensor can be expressed as follows:

$$\hat{\varepsilon} = \begin{pmatrix} \varepsilon_{xx} & i\varepsilon_{xy} & 0 \\ -i\varepsilon_{xy} & \varepsilon_{yy} & 0 \\ 0 & 0 & \varepsilon_{zz} \end{pmatrix} \tag{2.63}$$

If the medium is not birefringent, then ε_{xx}, ε_{yy} and ε_{zz} will be equivalent. The existence of an ε_{xy} term can be thought of as a manifestation of the Lorentz force inside the material. The Lorentz force law states that $\boldsymbol{F} = q\boldsymbol{E} + q\boldsymbol{v} \times \boldsymbol{B}$, where q is the particle charge and v is the particle velocity. The Lorentz force induces circular motion in the material's electronic response in the plane perpendicular to the magnetic field, and this circular motion is the origin of many magneto-optical effects.

The dielectric tensor is related to the index of refraction n by:

$$\hat{\varepsilon} = \mathbf{n} \cdot \mathbf{n} \tag{2.64}$$

where n is often expressed as the sum of a dispersive term δ and adsorptive term β:

$$n(\omega) = 1 - \delta(\omega) - i\beta(\omega) \tag{2.65}$$

Here, ω is the frequency of light under consideration. The refractive index and the dielectric tensor are both wavelength dependent, though generally I will not write this wavelength dependence explicitly.

2.7   Magneto-optical Kerr effects (MOKEs)

Light is a powerful tool for studying magnetism. Polarized light couples to the orbital motion of individual spin-polarized electron states, and the orbital motion couples to the electron spin via the spin-orbit interaction. In this way, light is able to probe all aspects of magnetic order in a material. In this thesis, I will focus on a light matter interaction called the magneto-optical Kerr effect (MOKE) which is able to access information about the off-diagonal elements of the dielectric tensor discussed in Section 2.6. The three versions of the magneto optical Kerr effect are shown below:
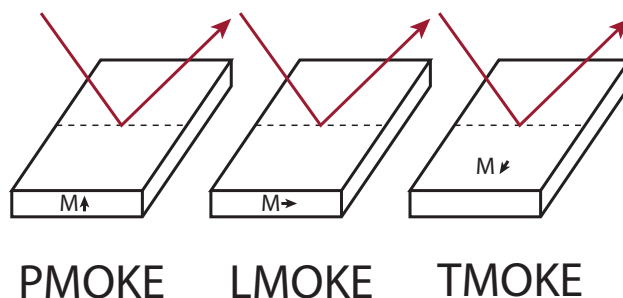
Figure 2.15: **Schematic of the three types of MOKE: polar (P), longitudinal (L), and transverse (T).** In PMOKE, the sample magnetization points out of plane. In LMOKE, the sample magnetization points along the plane of incidence and parallel to the sample surface. In TMOKE, the sample magnetization is normal to the plane of incidence. A general MOKE measurement can combine all of these effects, but most experimental setups use only a single type of MOKE in order to simplify the analysis.

All MOKEs involve reflecting a beam of polarized light off a magnetized sample (the transmissive equivalent of the Kerr effect is known as the Faraday effect). In PMOKE and LMOKE, linearly polarized light becomes elliptically polarized on reflection, and the principle axis of the ellipse is rotated relative to the original polarization. These effects are referred to as the *Kerr ellipticity* and *Kerr rotation*, respectively.

In TMOKE, the intensity of the reflectivity is measured instead of the polarization. If

the incident light is s-polarized relative to the sample, the polarization is parallel to the sample's magnetization; charge oscillations in the sample are thus parallel to the magnetic field and therefore experience no Lorentz force. Thus the sample's magnetization does not affect the reflectivity of s-polarized light. For p-polarized light, the charge oscillations are perpendicular to the magnetic field and therefore experience a Lorentz force. Thus we expect the magnetization to modulate the reflectivity of p-polarized light. If the magnetization points to the right of the incidence plane as viewed from the source (out of the page as viewed in Figure 2.15), the reflectivity is increased. If the magnetization points to the left (into the page in Figure 2.15), the reflectivity is reduced. The Fresnel coefficients for s- and p-polarized light are:

$$r_{ss}(M_\pm) = \bar{r}_{ss} \tag{2.66}$$

$$r_{pp}(M_\pm) = \bar{r}_{pp}\left[1 \pm \frac{\varepsilon_0\varepsilon_{xy}\sin 2\theta_i}{\varepsilon_{xx}^2\cos^2\theta_i - \varepsilon_0\varepsilon_{xx} + \varepsilon_0^2\theta_i}\right] \tag{2.67}$$

as given in [26, 27, 28], where $\bar{r}_{ss}$ and $\bar{r}_{pp}$ are the non-magnetic Fresnel coefficients for s- and p-polarizations, ε_0 is the permittivity of free space, ε_{xy} is the off-diagonal element of the dielectric tensor, θ_i is the incidence angle, and ε_{xx} is the diagonal element of the dielectric tensor. The normalized difference between the reflectivity of p-polarized light from a material magnetized in these two different directions is called the *asymmetry*, or the magnetic asymmetry:

$$A = \frac{I_+ - I_-}{I_+ + I_-} \tag{2.68}$$

$$= Re\left(\frac{2\varepsilon_0\varepsilon_{xy}\sin 2\theta_i}{\varepsilon_{xx}\cos^2\theta_i - \varepsilon_0\varepsilon_{xx}^2 + \varepsilon_0^2\sin^2\varepsilon_0^2\theta_i}\right) \tag{2.69}$$

where I_+ is the intensity of the reflected beam when the sample is magnetized in one orientation, and I_- the intensity of the reflected beam when the sample is magnetized in the opposite orientation. The sign of the asymmetry depends on the choice of which field is "positive." We can see that this asymmetry is directly proportional to the off-diagonal element of the dielectric tensor, and as such, is directly proportional to the sample's magnetization. In this thesis, I will focus exclusively on TMOKE because it is easier to measure changes in reflected intensity for EUV light than it is to measure polarization changes. Equation 2.68 gives us a simple experimental way to measure

the magnetism of a sample: measure the reflectance of a sample with p-polarized light in one magnetization direction, flip the magnetic field and measure the sample's reflectance again, then take the difference of these intensities and divide by their sum.

In this thesis, we will use the TMOKE that occurs in p-polarized reflectivity measurements to measure the sample's magnetic dynamics. Since the s-polarized reflectivity is not affected by the sample's magnetization, we will use it to measure hot electron dynamics and acoustic waves without any magnetic contribution. By combining these measurements, we can study all the degrees of freedom in magnetic thin films.

2.8   X-ray magnetic circular dichroism (XMCD)

In the x-ray region of the electromagnetic spectrum, magnetized materials exhibit a differential absorption between left and right circularly polarized light. This effect was first predicted in 1975 at the Ni M-edge (a $3p \rightarrow 3d$ transition) [29] and is called is called *x-ray magnetic circular dichroism*, or *XMCD*. In order to understand the origins of this effect, we will consider a two step process: in the first step, partially spin polarized electrons are excited from a core level to the valence shell by circularly polarized light. In the second step, this valence shell acts as a spin sensitive detector and only allows for the transition of a single spin polarization.

Although the experiments in this thesis all use M-edge transitions ($3p \rightarrow 3d$), we will follow Stöhr and Wu [30] and consider L-edge transitions ($2p \rightarrow 3d$) because the $L2$ and $L3$ edges ($2p_{1/2} \rightarrow 3d$ and $2p_{3/2} \rightarrow 3d$ transitions, respectively) are intense and do not overlap energetically (the spin-orbit-splitting of the initial state manifold is $\sim$15 eV), whereas the $M2$ and $M3$ edges overlap energetically (the spin-orbit splitting of the initial state manifold is $\sim$1 eV) and the transitions are much less intense. For these reasons, the L-edges are preferred for XMCD. As an aside, we use the M-edge in this thesis because we are primarily interested in ultrafast magnetic dynamics, which are most accessible by use of high harmonic generation (HHG) sources (see chapter 3). These HHG sources are currently limited to energies below 100 eV (corresponding to the transition metal M-edges) for practical applications, but many HHG soft x-ray sources (0.1-1 keV, corresponding to

the transition metal L-edges) have already been demonstrated, such as those found in References [31, 32, 33, 34].

We can probe the magnetic characteristics of an element by using dipole transitions from a non-magnetic core shell to a magnetic valence shell. Assuming that the material is magnetized along the z-axis and that the x-rays are incident along the z-axis, these transition matrix elements are given by:

$$D_\pm = \langle f | \hat{P}_\pm | i \rangle \tag{2.70}$$

where $\hat{P}_\pm = \hat{x} \pm i\hat{y}$ are the dipole operators for right and left circularly polarized light, respectively, the initial and final states are $|i\rangle$ and $|f\rangle$, respectively, and the probability of a given transition is $|D_\pm|^2$. Before computing transition probabilities, we can consider the dipole selection rules in order to reduce the number of transitions we need to compute. These dipole selection rules are:

$$\Delta l = \pm 1 \tag{2.71}$$

$$\Delta m_l = 0, \pm 1 \tag{2.72}$$

$$\Delta m_s = 0 \tag{2.73}$$

where l is the orbital quantum number, m_l is the magnetic quantum number, and m_s is the spin quantum number. A dipole transition must change the orbital quantum number and it cannot change the spin quantum number - this means that a dipole transition cannot flip an electron's spin. The magnetic quantum number either changes by ± 1 in the case of circularly polarized light, or by 0 in the case of linearly polarized light. Here, we will consider only circularly polarized light, so $\Delta m_l = \pm 1$.

We are interested in the magnetic properties of the $3d$ transition elements, and so we need to probe the $3d$ orbital - this will be our final state $|f\rangle$. For such an orbital, $m = 2$, and since we require that $\Delta m = \pm 1$, we will chose our initial state to be a p orbital with $m = 1$. As mentioned before, we will specifically consider the L-edge transitions, and so we will examine the $2p \rightarrow 3d$ transition. The six p orbitals are split by the spin-orbit interaction into two $p_{1/2}$ orbitals and four $p_{3/2}$ orbitals. These orbitals are shown below in Table 2.2:

Orbital	$\lvert lsjm_j\rangle$ basis m_j	$\lvert lsm_lm_s\rangle$ basis $Y_l^{m_l}\Phi_{m_s}$
$p_{1/2}$	1/2	$\sqrt{\dfrac{1}{3}}Y_1^0\uparrow+\sqrt{\dfrac{2}{3}}Y_1^1\downarrow$
	-1/2	$\sqrt{\dfrac{2}{3}}Y_1^{-1}\uparrow-\sqrt{\dfrac{1}{3}}Y_1^0\downarrow$
$p_{3/2}$	3/2	$Y_1^1\uparrow$
	1/2	$\sqrt{\dfrac{2}{3}}Y_1^0\uparrow+\sqrt{\dfrac{1}{3}}Y_1^1\downarrow$
	-1/2	$\sqrt{\dfrac{1}{3}}Y_1^-1\uparrow+\sqrt{\dfrac{2}{3}}Y_1^1\downarrow$
	-3/2	$Y_1^{-1}\downarrow$

Table 2.2: **Wavefunctions for the $p_{1/2}$ and $p_{3/2}$ levels, expressed as linear combinations of $\lvert lsm_lm_s\rangle$ states.** The functions $Y_l^{m_l}$ are the spherical harmonics.

In order to determine the spin polarization of the electrons excited from the initial state, we will assume that the final state is spin polarized, *i.e.* the spin up states are completely full and the only available state is spin down. Since the dipole transition cannot flip the electron's spin, we will only consider transitions from the spin down portion of the p orbitals. These initial states will take the form:

$$|i\rangle = a_{m_l}Y_1^{m_l}\downarrow \tag{2.74}$$

where $Y_l^{m_l}$ are the spherical harmonics and a_{m_l} are given in Table 2.2. The final states are:

$$|f\rangle = Y_2^{m_l}\downarrow \tag{2.75}$$

We can calculate the transition probabilities between these states by using the dipole matrix elements given in Bethe and Salpeter, Chapter 4 [35]:

$$\langle n',l+1,m_l\pm1|\hat{P}_\pm|n,l,m_l\rangle = -\frac{(l\pm m_l+2)(l\pm m_l+1)}{2(2l+3)(2l+1)}R \tag{2.76}$$

where all other matrix elements are 0 and R is the radial matrix element $R = \int R_{nl}^*(r)R_{n'l'}(r)r^3dr$.

The total transition probability is the sum of the transition probability from each initial state to each final state. By way of example, let us calculate explicitly the transition probability from a single p state to all possible final states using right circularly polarized light. We will choose

the $|j = 3/2, m_j = 1/2\rangle$ state (omitting writing $l = 1, s = 1/2$ since this is true for all p states). We can write this state in the $|lsm_lm_s\rangle$ basis as:

$$|j = 3/2, m_j = 1/2\rangle = \sqrt{\frac{2}{3}}\,|m_l = 0, m_s =\uparrow\rangle + \sqrt{\frac{1}{3}}\,|m_l = 1, m_s =\downarrow\rangle \tag{2.77}$$

Here, we reiterate that we can only excite down spin electrons because the d orbital is completely spin polarized. Thus, we neglect the first term of Equation 2.77 since it cannot serve as an initial state. Since we can only have a single final state from the second term of Equation 2.77 because of the selection rules, we can compute the probability of that transition using Equation 2.76 (remembering to take into account the coefficient of the initial state wavefunction):

$$|\langle n' = 3, l = 2, m_l = 2|\,\hat{P}_+\,|n = 2, l = 1, m_l = 1\rangle\,|^2 = \frac{1}{45}R^2 \tag{2.78}$$

We can now obtain the transition probabilities for the $L3$ edge ($2p_{3/2} \to 3d$ transition) by summing the transition probabilities for all 4 initial states in the $p_{3/2}$ manifold and all 10 final states in the d manifold:

$$I_{L_3}^+ = \sum_{i,f}|\langle f|\,\hat{P}_+\,|i\rangle\,|^2 = \frac{1}{3}R^2 \tag{2.79}$$

$$I_{L_3}^- = \sum_{i,f}|\langle f|\,\hat{P}_-\,|i\rangle\,|^2 = \frac{5}{9}R^2 \tag{2.80}$$

We can do the same for the $L2$ edge by summing over the 10 final states in the d manifold and the 2 initial states in the $p_{1/2}$ manifold:

$$I_{L_2}^+ = \sum_{i,f}|\langle f|\,\hat{P}_+\,|i\rangle\,|^2 = \frac{1}{3}R^2 \tag{2.81}$$

$$I_{L_2}^- = \sum_{i,f}|\langle f|\,\hat{P}_-\,|i\rangle\,|^2 = \frac{1}{9}R^2 \tag{2.82}$$

We can determine the relative intensities of the right and left circularly polarized transition by dividing by the total transition intensity. In this way, we get that right circular polarized light excites 32.5% spin down electrons and left circular polarized light excites 67.5% spin down electrons at the $L3$ edge, and right circular polarized light excites 75% down electrons and left circular polarized light excites 25% down electrons at the $L2$ edge.

The XMCD signal is given by $\Delta I = I^+ - I_-$. If the material is non-magnetic, there is no splitting in the d band, both up and down electrons can be excited, and there is no dichroic effect. If the material is ferromagnetic, the d band is exchange split and one spin polarization will be preferentially excited. We have assumed so far that the d band is entirely spin polarized, but in reality there will usually be available states for both spin up and spin down electrons. In this case, the XMCD signal is proportional to the sample's magnetization. For a more complete treatment of XMCD, see Stöhr and Wu [30].

We can treat the M-edge transitions in the exact same way as we have treated the L-edge transitions. In fact, the relative transition probabilities of spin up and spin down electrons for the the $M2$ and $M3$ edges are exactly the same as for the $L2$ and $L3$ edges. The absolute intensities of these edges are different, however, due to the difference in the radial matrix element $R = \int R_{nl}^* R_{n'l'} r^3 dr$. The energy difference between the $M2$ and $M3$ edges is also smaller than the difference between the $L2$ and $L3$ edges due to a smaller spin-orbit interaction in the $3p$ initial states than in the $2p$ initial states.
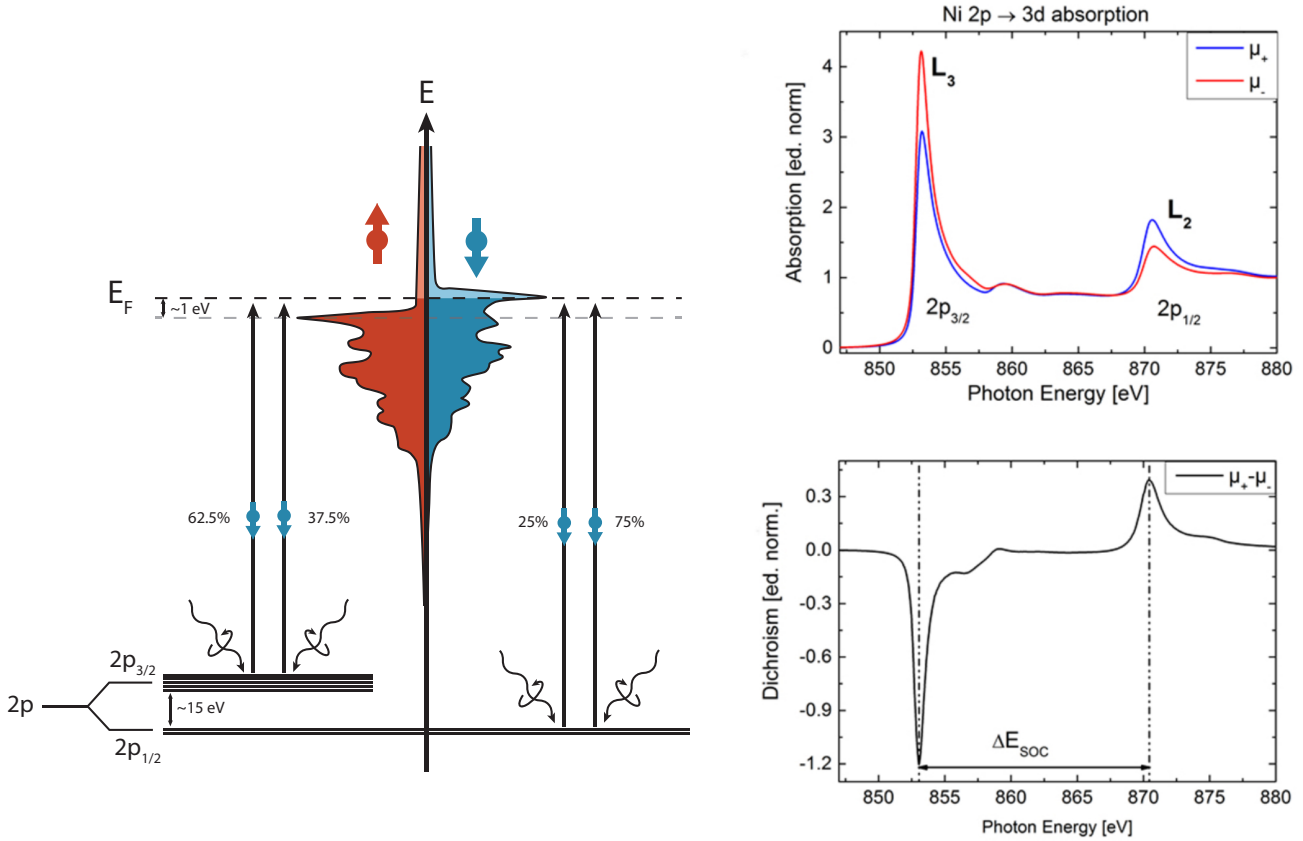
Figure 2.16: **XMCD schematic and absorption spectra.** The XMCD effect is generated by preferentially exciting one spin polarization with left or right circularly polarized light. On the left, the d band is shown for nickel and a large spin polarization at the Fermi energy is apparent. In computing the relative transition probabilities of left and right circularly polarized light, we have assumed that the spin polarization at the Fermi level is 100% and that the only available final states are spin down. On the right, the absorption of right and left circularly polarized light (μ_+ and μ_-) in Ni, along with their difference, is shown. This difference is the quantity referred to as XMCD. The figures on the right are adapted from [36].

2.9   EUV TMOKE

We can calculate the EUV TMOKE signal of a given sample using $\hat{\varepsilon}$, as described in Section 2.7. Since many samples are complex multilayers or have capping layers and substrates that are different materials, we must consider reflections from every interface to accurately calculate

the TMOKE response [37].

Despite our ability to calculate the TMOKE response of the material using macroscopic parameters like $\hat{\varepsilon}$, a microscopic description of TMOKE is sadly lacking. Such a description would likely enable us to study the dynamics of majority and minority spins independently. While developing an accurate microscopic description of EUV TMOKE is beyond the scope of this thesis, I will sketch a rough argument for how to understand EUV TMOKE on a microscopic level.

When p-polarized light is incident on the sample, an evanescent wave with a strange polarization state forms. The evanescent wave's polarization is elliptical, with an axis of rotation in the sample plane, perpendicular to the incident p-polarized light. This polarization state also forms in total internal reflection, and is shown in Figure 2.17 below:
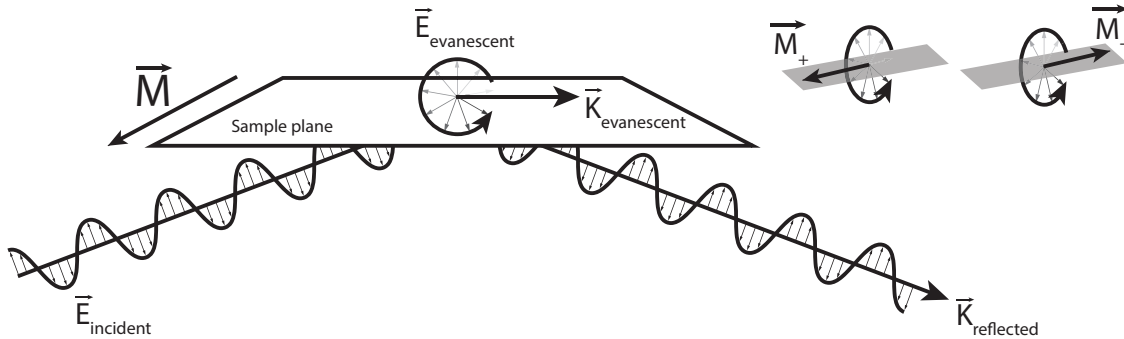
Figure 2.17: **Evanescent wave polarization in TMOKE.** Notice that the polarization of the wave is circular and perpendicular to the sample plane, and the polarization is therefore perpendicular to the sample magnetization. In the top right, I show how the helicity of the polarization changes relative to the magnetic field direction when the magnetic field direction is switched.

If we examine Figure 2.17, we see the emergence of a strange polarization state. This polarization state is circular, but the polarization is sometimes parallel with the propagation direction of the electromagnetic wave! While this may seem impossible based on the requirement that all electromagnetic waves are polarized transverse to their direction of propagation, such a state does not break any fundamental laws of electromagnetism. Milosevic provides an in depth discussion of

this polarization state [38].

Once this polarization state is obtained, we note that it rotates perpendicular to the direction of the magnetic field. If the direction of the magnetic field is switched, the helicty of the rotation relative to the magnetic changes sign; this is the same geometry that occurs in XMCD, implying that TMOKE and XMCD share the same underlying selection rules.

This discussion is only meant to give an approximate understanding of the selection rules for TMOKE and demonstrate heuristically that they are similar to the selection rules for XMCD. A detailed study is necessary to confirm that these selection rules are similar. Such a study would be of great interest to the field and it is my hope that this brief sketch might provide a productive avenue of investigation.

Having discussed a simple heuristic for understanding EUV TMOKE, we now turn our attention towards experimental measurements. We can see a representative EUV TMOKE measurement in Figure 2.18 below. This measurement was taken with the instrument described in Chapter 4. We first note that, even though there is only a single magnetic element (Ni) measured in Figure 2.18, the magnetic asymmetry nevertheless extends all the way from 48 eV to 72 eV, with the largest asymmetry present in the vicinity of the Ni $M2$ (66.2 eV) and $M3$ (68.0 eV) edges. The shape of this asymmetry can be calculated using Equation 2.68, taking into account that ε_{xx} and ε_{xy} are both functions of the photon energy. The large spectral extent of the magnetic asymmetry allows us to probe multiple parts of the band structure near the Fermi energy simultaneously, but it can also cause challenges in multi-element alloys because of the difficulty in assigning particular spectral features to particular elements. Practically, this means that we can only measure alloys where their M-edge resonances are spectrally well separated.
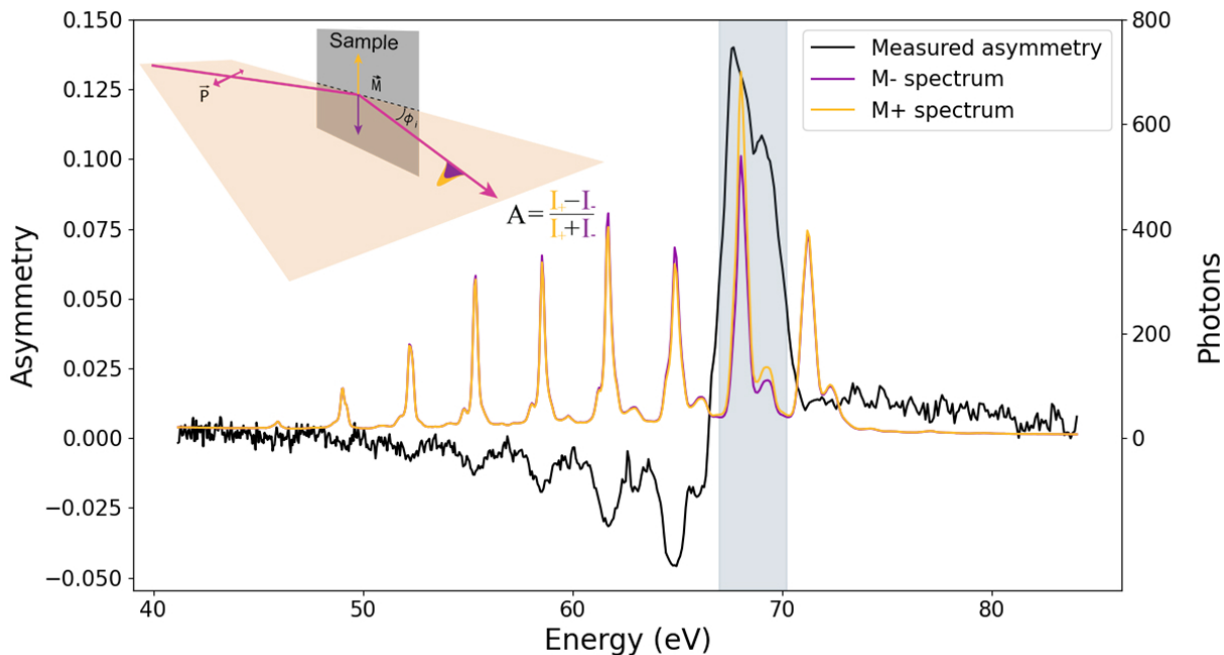
Figure 2.18: **Calculation of the TMOKE asymmetry from measured EUV spectra from the instrument described in Chapter 4.** The sample is a 5 nm Ni thin film with a 5 nm Si_3N_4 capping layer. The yellow and purple curves show the EUV spectra at opposite sample magnetizations, while the black curve shows the TMOKE asymmetry obtained by taking their normalized difference. When making time delayed measurements, we will integrate over one harmonic peak (one possible region is shown in gray), and record this value at various laser-pump, EUV-probe, time delays in order to map the evolution of the magnetization dynamics. The inset shows the TMOKE measurement geometry. Figure adapted from [39]

The broadband HHG source allows us to simultaneously investigate multiple transitions from the $3p$ orbitals to valence states above and below the Fermi energy. Not all states are accessible, however, due to the finite bandwidth of each harmonic peak and the spacing between harmonic peaks. The width of these peaks and the harmonic comb emission pattern are explained in Chapter 3.

In order to determine which elements we can measure simultaneously, let us examine the resonances of $3d$ transition metals. The transmissivity of 200 nm of each magnetic $3d$ transition

metal with photon energy is plotted below in Figure 2.19. Their M-edges (where transmission drops sharply) are clearly visible.
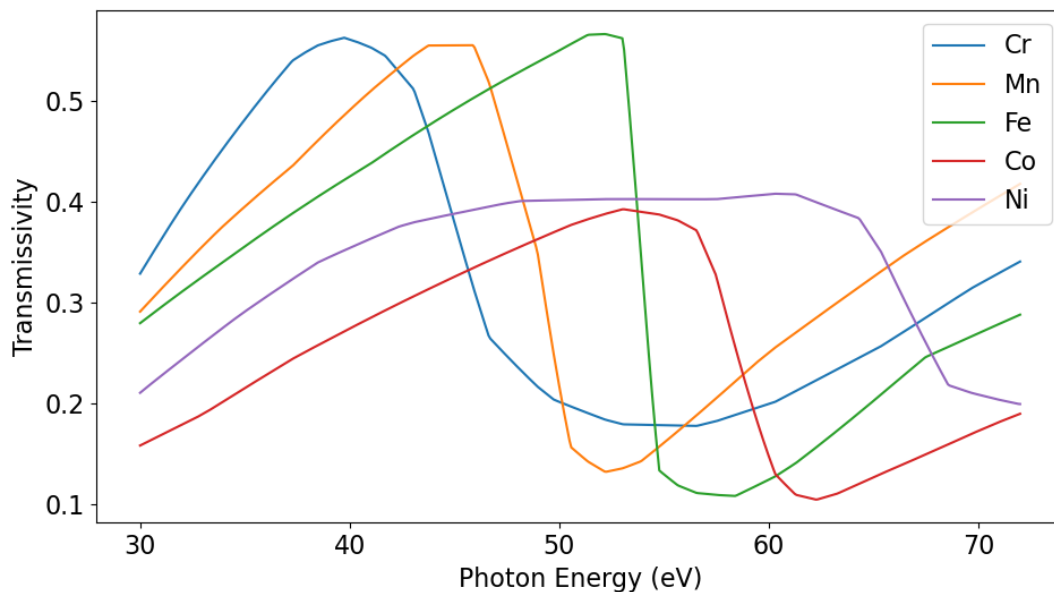
Figure 2.19: **Transmission of 200 nm of the** $3d$ **transition metals near their** M**-edge resonances.** Curves calculated using atomic scattering factors from [40].

Heuristically, if the resonances overlap, we cannot easily attribute a particular portion of the spectrum to a particular element. Specifically, this means that NiCo and FeCo alloys are challenging to study. This is an important limitation, but not a crippling one. Firstly, many other interesting compounds are available (in this thesis, we will look at NiMn and CoMn compounds). Secondly, advances in HHG will produce practical soft x-ray sources that will enable spectroscopy at the L-edge, where elemental resonances are further separated, allowing us to study NiCo and FeCo compounds in the future.

Chapter 3

High Harmonic Generation

High harmonic generation (HHG) allows us to convert low energy photons in the visible or infrared (IR) spectral range to high energy photons in the extreme ultraviolet (EUV) or soft x-ray range (SXR). While HHG is an active research area in its own right, in this thesis I am focused on the utility of HHG as an element specific, ultrafast probe for magnetism. Therefore, I will discuss only the most basic theory for HHG, along with some practical considerations for an experiment. In this thesis I will convert ~1.6 eV IR photons into 40-72 eV EUV photons using neon gas as the nonlinear medium. This requires optical intensities on the order of 10^{14} W/cm^2, and so I will focus ~50 fs pulses up to 1.5 mJ from a regenerative Ti:Sapphire amplifier into Ne gas. A more in-depth discussion of the experimental considerations can be found in Chapter 4. In the rest of Chapter 3, I will discuss HHG in a single atom picture, how to add the emission from multiple atoms coherently, and different gas target geometries that have various advantages and disadvantages for experimental use.

3.1   Three-step model

High harmonic generation (HHG) is most easily understood as a semi-classical three-step model where the atom is treated quantum mechanically and the electric field is treated classically. In this model, a strong electric field comparable to the atomic binding potential ($\sim 3 \times 10^{10}$ V/m) ionizes the atom by distorting the Coulomb potential into a finite barrier, allowing the electron to tunnel through the barrier and escape. The electric field then reverses direction and the free

electron is accelerated back towards the parent ion. Finally, the electron recombines with the parent ion, releasing its kinetic energy as a high energy photon. Pulsed laser sources are need to obtain the high electric fields required by HHG, and noble gasses are the most common nonlinear medium. HHG is most efficient when driven by linearly polarized lasers, and the polarization is maintained in the HHG process. While HHG generally cannot be driven by circularly polarized light with a single wavelength, circularly polarized EUV can be generated through HHG by using two colors with counter rotating polarizations simultaneously [41, 42].
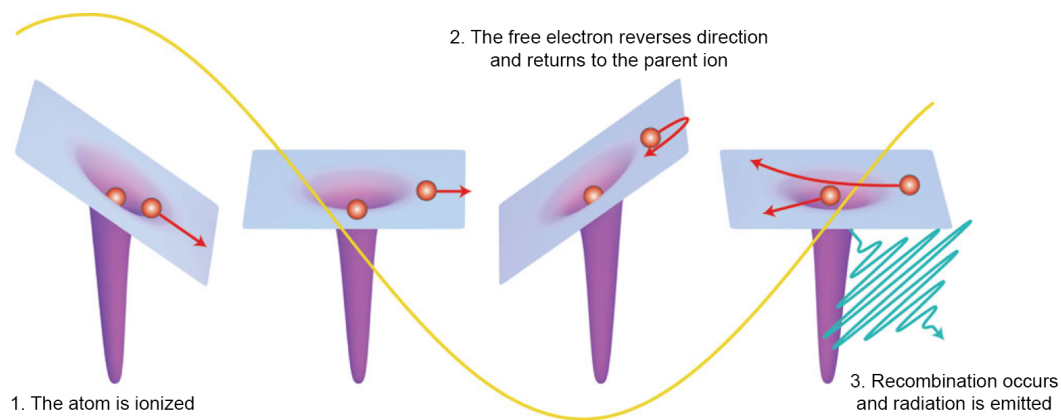
Figure 3.1: **The three-step model of high harmonic generation.** An intense laser field first distorts the Coulomb potential of the atom, allowing an electron to escape via quantum tunneling. When the laser field reverses direction, the electron returns to the parent ion. Finally, the electron can recombine with the parent ion, releasing the kinetic energy it has acquired as radiation. Figure adapted from [43].

As seen in Figure 3.1, the process of high harmonic generation happens within a single optical cycle. This allows for the emission of an isolated attosecond burst by using a driving laser with very short pulse duration [44, 45, 46]. If a longer driving laser pulse duration is used, an attosecond burst will be emitted every half-cycle of the driving laser. These bursts form a "pulse train" with a duration that is somewhat shorter than the driving laser pulse, since the bursts will only be emitted during the portion of the pulse where the field intensity is high enough to ionize

the gas. Because the attosecond bursts occur at every half cycle of the driving laser, they can be represented with a Fourier series consisting of components spaced by 2ω. When the driving laser is short, these Fourier components are wide and eventually form a continuum. When the driving laser is many cycles long, these Fourier components are sharp and well defined. The result is that the HHG spectrum is a well-known "comb" shape, with each tooth spaced 2ω from the next.
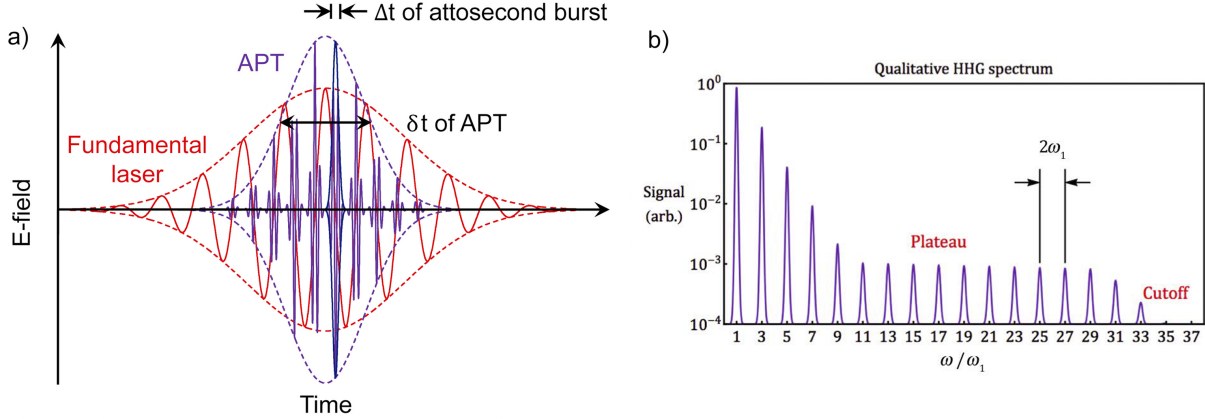
Figure 3.2: **Temporal and spectral characteristics of high harmonic generation.** (a) A single driving laser pulse generates multiple attosecond bursts that form an attosecond pulse train which is shorter than the driving laser pulse. The emission of attosecond bursts are brighter at the leading edge of the laser pulse in real media because of time dependent ionization effects. (b) The harmonic frequencies are spaced by 2ω, starting with the fundamental frequency and reaching the cutoff frequency, because the attosecond bursts are emitted every half-cycle of the driving laser. More driving laser cycles causes the width of an individual harmonic tooth to narrow. Figure adapted from [47, 48].

We can calculate the maximum photon energy that HHG can produce by considering the ionization potential of the nonlinear medium and the maximum kinetic energy that the recombining electron can acquire from the driving laser [49]. This maximum photon energy is:

$$E_{max} = I_p + 3.17 U_p \tag{3.1}$$

where

$$U_p = \frac{e^2 I}{2c\varepsilon_0 m\omega^2} \tag{3.2}$$

is the ponderomotive energy, e is the electron charge, I is the laser intensity, c is the speed of light ε_0 is the permittivity of free space, m is the electron mass, and ω is the driving laser frequency. This maximum photon energy is clearly visible in Figure 3.2. From Equation 3.1, we can see that choosing a nonlinear medium with a higher ionization potential allows for higher photon energies. We can also see in Equation 3.2 that the Ponderomotive energy scales with the inverse square of the driving laser frequency - using a longer wavelength driving laser allows us to obtain higher photon energies. Intuitively, we can understand this because a longer wavelength leads to a longer electron trajectory (since each electric field period is longer), and thus a greater kinetic energy upon recombination.

Although moving to longer wavelengths allows for increased photon energies, the free electron wavepacket diffuses more the longer it spends in free space, reducing the probability of recombination and thereby decreasing the conversion efficiency by $\sim \lambda^{-6}$ if the driving laser intensity is fixed [50]. Increasing the density of emitters can partially compensate for the substantially decreased yield at longer wavelengths. As we consider adding additional emitters, we must address the issue of adding the light from each emitter coherently.

3.2   Phase matching

In order to achieve high efficiency in any nonlinear process, all emitters need to emit light in phase with each other. This means that the driving laser wavelength and generated wavelength need to have the same phase velocity in the medium. This is referred to as *phase matching*. We can write the condition that the phase velocities of the driving laser and the generated harmonic must be equal as:

$$\frac{\omega_f}{k_f} = \frac{\omega_q}{k_q} \tag{3.3}$$

where ω_f and ω_q are the fundamental and qth harmonic angular frequencies, and k_f and k_q are the fundamental and qth harmonic wavenumbers. Since $\omega_q = q\omega_f$, we can write the phase mismatch as:

$$\Delta k = qk_f - k_q \tag{3.4}$$

When $\Delta k = 0$, the signal builds over distance and is limited only by the absorption of the nonlinear medium. When $\Delta k \neq 0$, the signal can only build over a short distance called the coherence length $l_c = \pi/\Delta k$. Our goal is to tune our system parameters such that $\Delta k = 0$.

In high harmonic generation, we assume that the phase velocity of the generated light has an index of refraction very near to 1, and therefore its phase velocity is unchanged relative to vacuum. Thus, we only need to consider how the nonlinear index of refraction changes for the driving laser. In this thesis I will only address HHG in a gaseous medium, and because HHG is an ionizing process, we must consider both the neutral atom contribution and the plasma contribution to the phase matching equation. We can write the phase mismatch as:

$$\Delta k = qP(1-\eta)\frac{2\pi\lambda}{\Delta\delta + n_2} + qP\eta(N_a r_e \lambda) - qk_g \tag{3.5}$$

where q is the harmonic order, P is the pressure, η is the ionization fraction, λ is the driving laser wavelength, $\Delta\delta$ is the difference between indices of refraction of the gas at the driving laser wavelength and at the generated wavelength, N_a is the number density of atoms per unit of pressure, r_e is the classical electron radius, and k_g is the geometric wavenumber [51, 52]. Since the plasma contribution is negative and the neutral atom contribution is positive (and the geometric contribution is usually negative), there is an ionization fraction that causes $\Delta k < 0$ at any pressure. This ionization fraction is called the *critical ionization*, above which phase matching cannot occur. This critical ionization is wavelength and medium dependent and sets an effective maximum field intensity for HHG. The cutoff photon energy scaling with wavelength for various noble gasses, taking into account the critical ionization, is shown below [53, 32]:
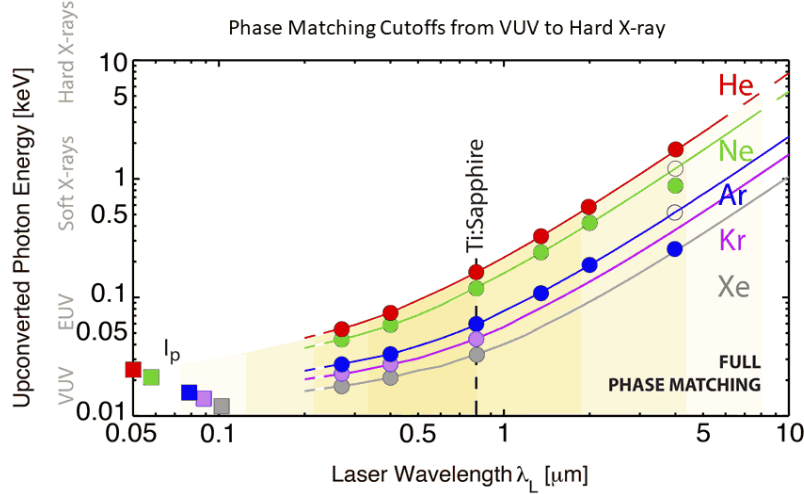
Figure 3.3: **The HHG phase matching cutoff for different gases and driving laser wavelengths.** Ti:Sapphire lasers are indicated because of their prevalence in HHG. Figure adapted from [32].

Another consequence of Equation 3.5 is that there is an optimal pressure for phase matching a particular harmonic order. The specific values of the critical ionization and phase matching pressure also depend on the final term in the phase matching equation: the geometric wavenumber k_g. In considering this term, we turn our discussion towards various gas target geometries for HHG.

3.3 Gas target geometries

While there are many varieties of gas targets that can be used in HHG, we will consider three popular geometries here: the gas jet, the capillary waveguide, and the semi-infinite gas cell. Each of these geometries has various advantages and disadvantages.

Gas Jet

The gas jet is the simplest gas target for HHG. It consists of a small nozzle that releases a plume of gas into a vacuum chamber. The driving laser is then focused very tightly to a position slightly before the plume of gas which maximizes the interaction volume while minimizing the effects of the Guoy phase shift on phase matching. The geometric terms in the gas jet geometry are the

Guoy phase term (always negative) and the atomic dipole term (switches sign on either side of the focus). A more detailed discussion of the geometric contributions for the gas jet can be found in [54, Chapter 1.2.2]. Skimmers can be placed near the gas jet to enhance differential pumping of the gas and minimize the re-absorption of EUV light. The major challenges of using a gas jet are the short interaction length (the gas target is only 100s of microns in length), difficulty achieving high pressures (there is no confinement and so the gas will rapidly disperse into the vacuum), and high gas use.

Despite its limitations, the gas jet geometry continues to be popular in HHG applications because (1) it is a good choice if you have limited pulse energy since a tight focus is then required to achieve high electric fields, (2) it is easy to set up, requiring only a small aperture nozzle, and (3) since the laser is always propagating through free space and no optical coupling is required, the driving laser mode shape and size can be changed on the fly. For these reason, it remains the standard gas target for light science research [55, 56, 57, 58, 59].
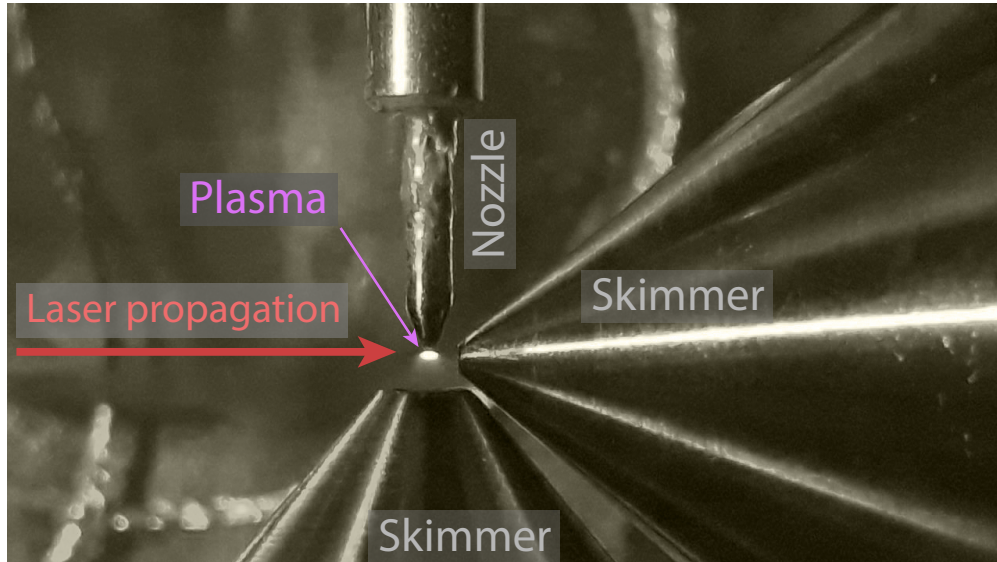
Figure 3.4: **Image of plasma flourescence from an Ar gas jet.** The laser propagates left to right. The gas flows from top to bottom, and there are two "skimmers" present to remove excess gas. Image courtesy of Henrike Probst at the University of Göttingen.

Capillary waveguide

The capillary waveguide improves on the gas jet by confining the driving laser to a particular guided wave mode in a hollow core fiber. This guided wave mode introduces a geometric wavenumber $k_g = u_{11}^2 \lambda/4\pi a^2$ to Equation 3.5 where u_{11} is the guided mode factor, λ is the driving laser wavelength, and a is the inner radius of the hollow waveguide [53]. This geometric wavenumber allows us to cancel neutral atom and plasma contributions from Equation 3.5 to set $\Delta k = 0$ and achieve true phase matching for HHG. Phased matched HHG in a capillary can be 2-3 orders of magnitude brighter as compared to that of a gas jet because of the long interaction length that allows a coherent build up of EUV photons [52]. Moreover, a capillary enables the production bright soft x-ray harmonics driven by mid-IR lasers. This is because the low single-atom yield due to quantum diffusion must be compensated by using very high gas pressures (10-140 atm) [53, 32].
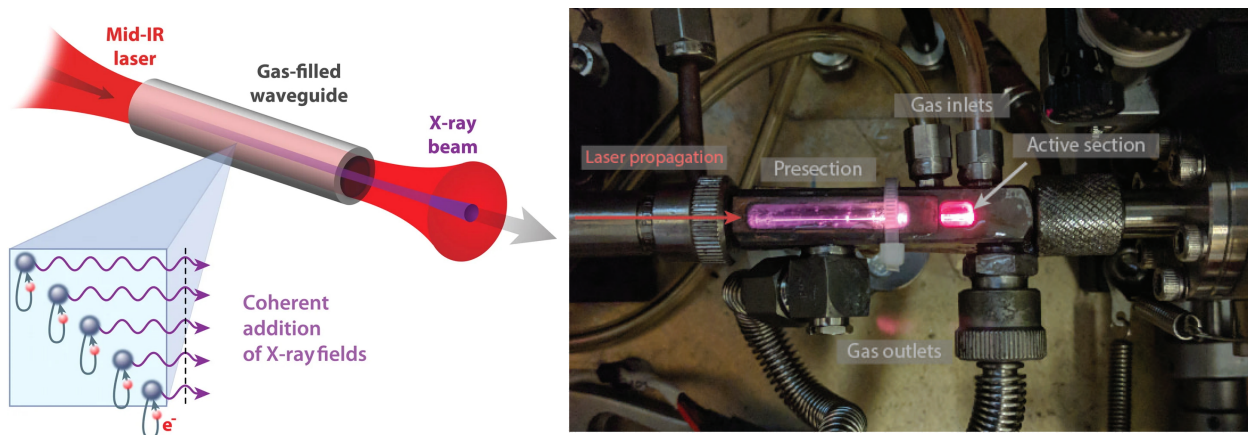
Figure 3.5: **HHG in a capillary waveguide.** Left: A driving laser is focused into a capillary filled with a noble gas. The guided wave mode has a propagation velocity which can be tuned by varying the inner diameter of the fiber. The wave speed of the driving laser can thereby be matched to the wave speed of the coherent EUV / x-ray emission. Figure adapted from [53]. Right: a 2018 capillary from KM Labs. There is a pumped-out presection with no ionization that cleans the laser mode before it enters into the active section, where there is strong ionization and the HHG occurs. In reality there is still some plasma present in the presection, but substantially less than in the active section. Newer capillary designs include water cooling which helps ensure thermal stability.

The capillary can also be combined with a differential pumping aperture to minimize reabsorption. The complexity of this geometry can make it challenging to use: difficulties coupling the driving laser into the capillary and power dissipation into the waveguide can cause long term intensity and pointing instabilities, fabricating gas inlets incorrectly can distort the mode, and sloped gas pressure profiles around the active section can make proper phase matching difficult. Despite these challenges, the capillary waveguide has become a popular choice for applications including angle resolved photoelectron spectroscopy (ARPES) [47, 60, 61, 62, 63] and coherent diffractive imaging (CDI) [64, 65, 66, 67] because of its high brightness and high spatiotemporal coherence.

Semi-infinite gas cell

In this thesis, I use a semi-infinite gas cell (SIGC) as a gas target for HHG. The SIGC combines the ease of alignment of a gas jet with the long interaction length of a capillary and, in my opinion, this combination makes it an ideal light source for applications because it has high brightness, good mode quality, is easy to use after an initial alignment, and is very stable over the long term. In the SIGC geometry, a long cell is filled with a noble gas and a laser is loosely focused into it, to a point just before a copper foil. The laser drills a hole through the copper foil, allowing the generated EUV light to exit the SIGC. Since the laser drills its own exit aperture, no alignment is necessary. After the driving laser and EUV exit the SIGC, they enter a high vacuum environment and no longer interact with the gas medium.
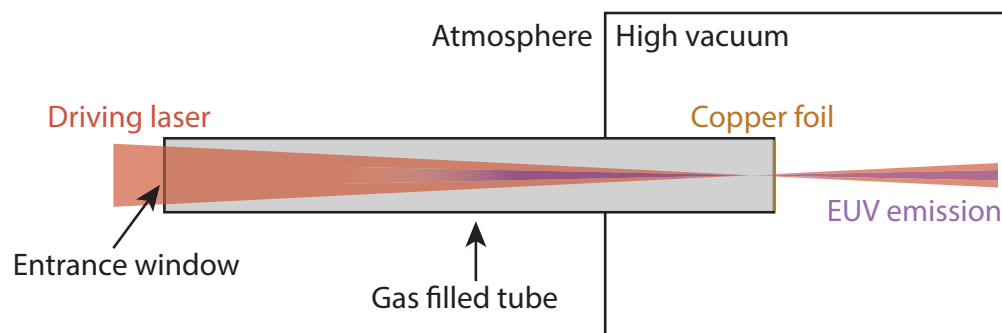
Figure 3.6: **Schematic of a semi-infinite gas cell.**

Although phase matching in the SIGC is not fully understood, there is evidence that this geometry can support laser filamentation and self guiding [68, 69], allowing phase matching over several millimeters of propagation length [70]. Like the capillary waveguide geometry, this extended interaction length allows for the build-up of much brighter EUV emission than in the non-phase matched case.

Phase matching can be optimized for different harmonic energies by moving the focus relative to the exit foil, as shown below:
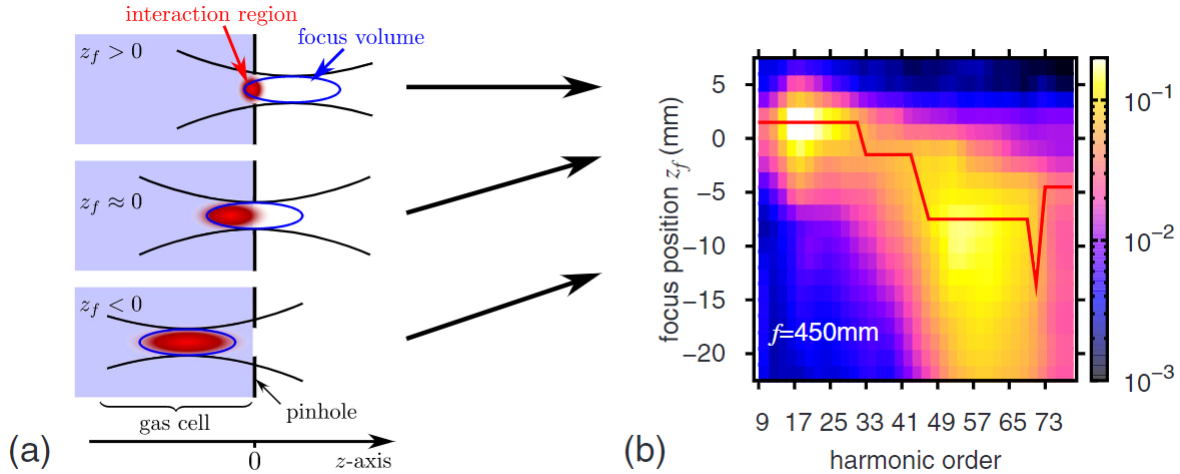
Figure 3.7: **Illustration of phase matching in a SIGC for different focal positions relative to the exit foil.** High or low energy harmonics can be optimized depending on the focal position. These measurements were taken using a pressure of 50 torr of He, which does not have sufficient nonlinearity to create a laser filament with the powers used here. Figure adapted from [71].

In our own setup, we observe the ability to change which harmonics are phase matched by adjusting the position of the focus relative to the exit foil. This may indicate that no filamentation occurs and thus the physics is similar to that described in [71], or the phase matching condition for different energies may still depend on the focal position even in the presence of filamentation due to self focusing and self compression as seen in [72]. We did not investigate this beyond noting that it is possible to tune our optimal phase matching energy by adjusting the lens position, gas pressure, and chirp (second order dispersion) of our driving laser.

3.4   Practical considerations

When designing an HHG source, we need to balance many competing interests:

(1) We need to separate the EUV from the driving laser

(2) Single atom yield decreases with increasing driving laser wavelength

(3) Phase matching pressure increases with increasing driving laser wavelength

(4) Cutoff energy increases with increasing driving laser wavelength

(5) Cutoff energy increases with increasing ionization energy

(6) Total number of emitters increases with increasing density-length product

(7) Reabsorption increases with increasing density-length product

(8) Different gasses have different, energy-dependent reabsorption profiles

(9) Changing emitter type, density, driving laser wavelength, driving laser power, and laser focal plane changes the phase matching condition

(10) Vacuum pumps struggle more with light gasses and less with heavy gasses

(11) A tighter focus increases maximum field intensity and decreases the number of emitters that participate in HHG

(12) The Guoy phase shift is more important with a tighter focus

(13) Having an iris for shaping the transverse spatial mode and for shaping the evolution of the longitudinal mode can be very important for bright harmonics [73].

I will address these considerations for our particular setup. If you find yourself designing your own HHG setup, hopefully this will serve as a useful example for what kind of thought process is involved in building an ultrafast EUV source.

(1) We let the driving laser and EUV propagate 2 meters from the source plane so that the driving laser has diverged enormously and the EUV beam is ~ 2 mm in diameter. This allows us to use a single 200 nm Al filter on copper mesh to remove the 780 nm driving laser light and allow the short wavelength EUV light to pass through. Many setups use rejector mirrors that reflect only the EUV light, but such mirrors are highly polarization sensitive. In this setup, we require the ability to rotate freely between vertical and horizontal polarizations, and so free space propagation is the

easiest way to reduce the power density of the driving laser, preventing us from burning through our Al filters.

(2-4) The best laser is the one you have. We have a KM Labs Wyvern, which is a cryo-cooled Titanium:Sapphire regenerative amplifier with a central wavelength at 780 nm, a $\sim$ 50 fs pulse duration, 5 kHz repetition rate, and 2 mJ pulse energy.

(5-9) Choosing the right gas and geometry requires some thought about what interaction lengths you can phase match over vs how severely it will reabsorb. If you can phase match, a longer density-length product will probably help you get brighter harmonics. Helium has low reabsorption, but if you can't phase match over really long distances, it might not offer much benefit over neon (depending on what energy range you're targeting). Argon reabsorbs strongly and has a curious spectral feature called the Cooper minimum [74]. Xenon and krypton are good for low energy harmonics. Reabsorption is going to limit you no matter what, and the most important thing you can do to mitigate this is to develop a good differential pumping scheme where you can quickly drop from high pressure to low pressure. We do this in our setup by going straight from the SIGC to high vacuum and allowing supersonic expansion to drop our pressure as fast as is possible. Using our laser, for our target energy range of 40-72 eV, means that we will choose neon as a gas target.

(10) If you chose to work with helium, especially at high phase matching pressures, you're going to need a lot of pumping power to get it out of your vacuum system. This typically means big, expensive pumps - or lots of pumps. Neon and argon are both much easier, with neon being somewhat more challenging than argon.

(11-12) If you can ensure that your confocal parameter is longer than your absorption depth limited interaction length, you should strive to reach the critical ionization threshold for your HHG process, otherwise you are leaving photons on the table. If your laser has low pulse energy, you may have to focus very tightly in order to achieve the requisite electric fields for critical ionization. This can make you much more sensitive to the Guoy phase if you are working in a gas jet, or make it impossible to couple into a fiber with an appropriate diameter. Additionally, the very tight focus

reduces the total number of emitters that participate in HHG, reducing your total yield.

(13) Shaping the transverse mode of your beam into an Airy disk is essential for good coupling into a capillary waveguide. It can also greatly extend the phase matching cutoff for phase matching in a gas jet [75], and anecdotally from our own setup, it substantially increases the brightness of our SIGC.

Chapter 4

Experimental design and setup

In this chapter, I will describe an instrument named X-MATTER (**X**UV **M**agnetic **A**symmetry with **T**abletop **T**emporal and **E**lemental **R**esolution) that I developed. X-MATTER is an ultrafast EUV spectrometer for measuring magnetic dynamics using the transverse magneto-optical Kerr effect (TMOKE). This instrument uses a secondary, reference spectrometer to cancel the intensity fluctuations of the HHG source, substantially improving the signal-to-noise ratio (SNR) and acquisition time of our measurements. The development and construction of X-MATTER is the first main achievements of this thesis. Much of this chapter is adapted from my paper titled "An extreme ultraviolet beamline for ultrafast magneto-optical spectroscopy near the shot noise limit" [39], currently under review.

4.1   Motivation

While the fundamental length- and time-scales for magnetic phenomena are set by the exchange length and the exchange interaction (Å to nm and fs, respectively), methods for accurately probing these dynamics have only recently become available. Since the first observation of sub-picosecond demagnetization [8], ultrafast spin dynamics has developed into an active field of research, particularly because of its relevance to future energy-efficient spintronic devices. In the intervening two decades, ultrafast lasers have been used to quench or switch the magnetic orientation of materials [76, 77, 78, 79], while superdiffusive spin currents (see Chapter 2.5.3) provide alternative routes for selective magnetic control in multilayers [21, 23]. In addition, light-induced

spin transfer has been used to manipulate spin polarization on few-femtosecond timescales [80, 81, 82, 83]. Despite this progress, a comprehensive understanding of how magnetic materials behave on short time scales has not yet emerged.

Ultrafast visible lasers can probe the magnetic state of a material on femtosecond timescales using magneto optical effects such as the magneto optical Kerr effect (MOKE) or magnetic circular dichroism (MCD). These methods can in some cases provide limited information on elemental specificity through careful analysis of measurements using tunable or broadband probes [84, 85]. However, direct element specific magnetic dynamics can be obtained by using extreme ultraviolet (EUV/XUV) light sources, which probe transitions from atomic core shells to near the Fermi level. The EUV transverse magneto-optical Kerr effect (TMOKE, see Chapter 2.9) has been used to study fundamental demagnetization timescales [86, 87], spin transport between magnetic multilayers [23, 22], temperature-dependent element-resolved magnetization [88], and light-induced spin transfer between elements in magnetic sublattices of complex alloys [25, 81]. EUV TMOKE has the benefit that it operates in reflection mode, which is ideal for the study of magnetic thin films and multilayer devices. The primary disadvantage of using reflection-mode EUV TMOKE measurements, in contrast with transmission-mode x-ray magnetic circular dichroism measurements (XMCD, see Chapter 2.8), is a large photon loss – generally on the order of 99% or more. This occurs because the TMOKE signal is largest near Brewster's angle – where for example, the reflectivity of a pure Ni sample at 66 eV (at the Ni M-edge) is only 10^{-3} at an angle of 40 degrees from glancing incidence (the angle at which all data in this thesis was acquired). TMOKE can also measure depth dependent magnetization effects that make interpretation challenging, especially for complex multilayer structures [89].

One issue that must be mitigated when using either large scale or tabletop scale EUV light sources is their higher intensity fluctuations compared with visible femtosecond lasers (up to 100% shot-to-shot intensity fluctuations depending on the source, compared with 0.5% for a visible femtosecond laser). The high repetition rate of most HHG experiments (1-100 kHz) allows for temporal averaging to reduce the measurement noise, and some HHG sources have pushed to

even higher repetition rates to further reduce their measurement noise[88]. These extremely high repetition rate fiber-laser based HHG sources effectively reduce their noise through fast averaging, but their low pulse energy limits the total HHG flux and thereby limits their achievable SNR. In the case of x-ray free electron laser (XFEL) sources, extensive beam diagnostics combined with post-processing allow them to achieve similar noise levels to HHG experiments [90, 91]. HHG sources have an additional advantage of perfect synchronization in time between the driving laser and generated HHG light, which has made it possible to uncover new spin and charge dynamics behaviors — including the ability to distinguish between electron-electron scattering and screening [60], the ability to distinguish between spin transport and spin-flip processes [23], and the ability to directly observe light-induced transfer of spin polarization [25]. In practice, the HHG intensity fluctuations essentially limit what signal can be measured within a given time period. Previous research overcame this limit for probing spin dynamics by implementing an intensity-normalizing beamline for HHG based x-ray magnetic circular dichroism (XMCD) in a high-efficiency transmission mode geometry. The element-specific magnetic dynamics of CoPt alloys were then measured with high signal-to-noise ratio (SNR) [92, 93].

Here we present a setup for implementing time-resolved EUV measurements of magnetic samples near the shot noise limit, in the challenging low-efficiency reflection-mode geometry, and over a wide range of pump fluences (see Figure 4.1). This instrument, named X-MATTER (**X**UV **M**agnetic **A**symmetry with **T**abletop **T**emporal and **E**lemental **R**esolution), allows us to measure element-resolved spin dynamics, hot electron dynamics, and acoustic dynamics on their intrinsic timescales, from femtosecond to picosecond and longer time scales. We implement a reference spectrometer that acts as a digital noise canceller, allowing us to cancel the noise of each harmonic order independently, thus reducing the EUV intensity fluctuations to near the shot noise limit. We also present intensity measurements of our EUV flux after propagation through our beamline, demonstrating that we are near the theoretical noise floor as determined by the addition of photon shot noise and electronic noise from our CCD cameras. Finally, we present ultrafast spin dynamics measurements of single-element and multi-element-alloy thin films to demonstrate the capabilities

of this new setup. This approach reduces the time taken to acquire a given signal-to-noise data set by more than an order of magnitude and is particularly beneficial for studying small magnetic asymmetries associated with small magnetic moments. Further improvements in the EUV flux, optical coatings, and grating design can reduce the acquisition time by an additional 1-2 orders of magnitude.
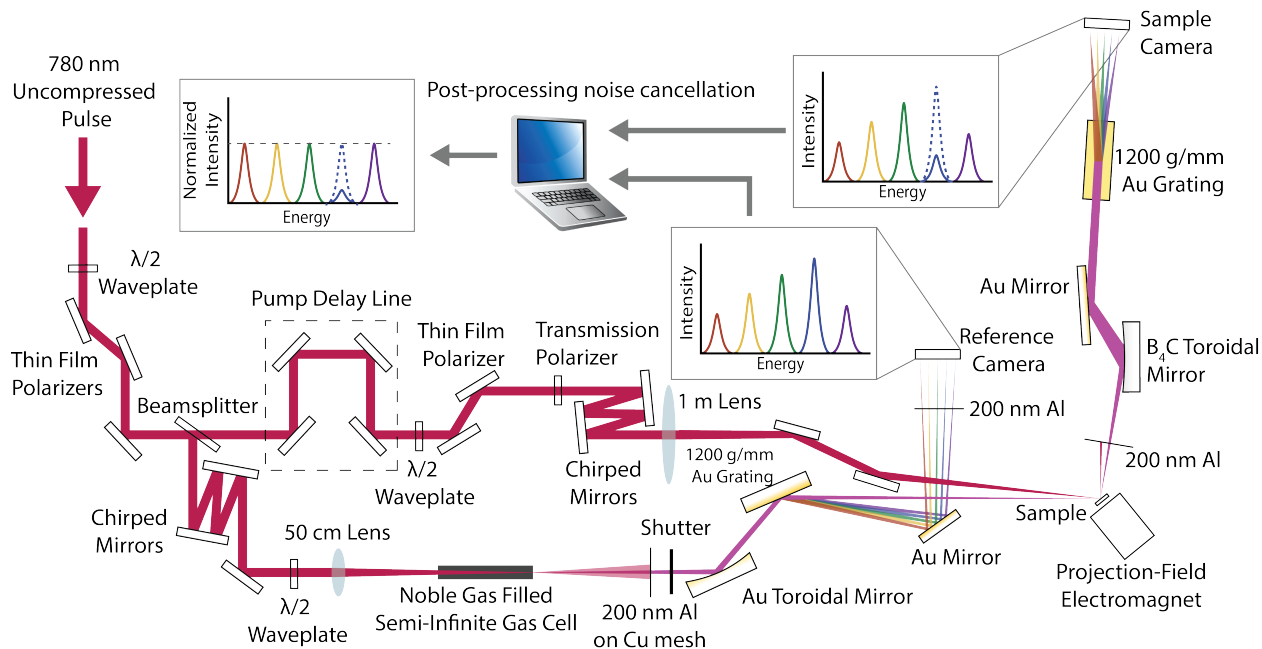
Figure 4.1: **X-MATTER (*X*UV *M*agnetic *A*symmetry with *T*abletop *T*emporal and *E*lemental *R*esolution) experimental setup for near shot noise limited reflection mode ultrafast EUV spectroscopy of magnetic thin films.**

4.2   Design considerations for an intensity normalized EUV reflection mode beamline

We designed the sample and reference spectrometers shown in Figure 4.1 to span a photon energy range of 45-72 eV simultaneously, allowing for the measurement of M-edge reflectivities of the $3d$ transition metals Mn ($\sim$48 eV), Fe ($\sim$55 eV), Co ($\sim$60 eV), and Ni ($\sim$66 eV), as well as the magnetically active edges of some 4d and 5d transition metals. By measuring the reflectivities on

and off these resonances for different polarizations of the EUV probe, we can directly access and separate the spin, charge, and acoustic dynamics in the sample after excitation by a femtosecond laser.

In addition to implementing a sample spectrometer, we also implement a reference spectrometer for monitoring (and then cancelling) the intensity fluctuations associated with each harmonic order. This is important because small laser intensity fluctuations can change the fractional ionization of the gas, and as a result, change the optimal HHG phase matching conditions that are different for each harmonic order [51]. We use a grazing incidence diffraction grating as an EUV beamsplitter – as shown in 4.1, we send the zeroth diffracted order (which contains the full harmonic comb) onto the sample, and use the first diffracted order of the reference spectrometer to monitor the intensity fluctuations of each harmonic order.

When designing the beamline, we required that the sample and reference spectrometers have the same photon throughput. This requirement ensures that we can operate both the sample camera and reference camera with the same exposure times, thereby allowing both cameras to measure the same number of EUV pulses. This is not a trivial requirement in the EUV because of the spectrally varying reflectivity and strong absorption of all optics throughout the entire EUV spectrum. In addition to designing the beamline so that each spectrometer has similar photon throughput, we also implement a timing scheme that ensures both cameras measure the same EUV pulses. This timing scheme, synchronizing the cameras, shutters, and electromagnet, is shown in Figure 4.2:
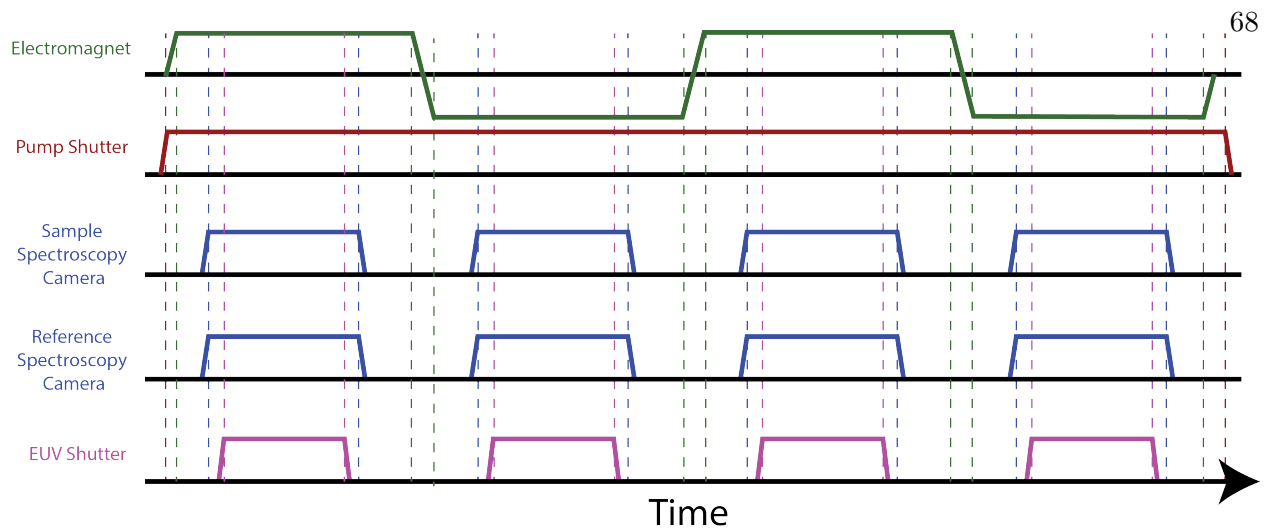
Figure 4.2: **Timing diagram for the X-MATTER beamline.** Importantly, both cameras are gated by the same shutter, ensuring that we have the same number of pulses on both cameras and allowing the noise cancellation procedure to work correctly. We allow for the electromagnet to cycle during the camera readout time to maximize data collection efficiency. The pump shutter is open the entire time, with timing synchronization between the pump and the probe implemented by a delay stage.

After designing the beamlines to have similar photon throughput and properly synchronizing the cameras with the shutters, we need to verify that they *actually* have similar throughput, since many of the assumptions we make about the reflectivity of the mirrors and diffraction efficiency of the gratings can be highly inaccurate. We verify this photon throughput with a 5 nm Si_3N_4 / 5 nm Ni / SiO_2 sample, as shown in Figure 4.3 below:
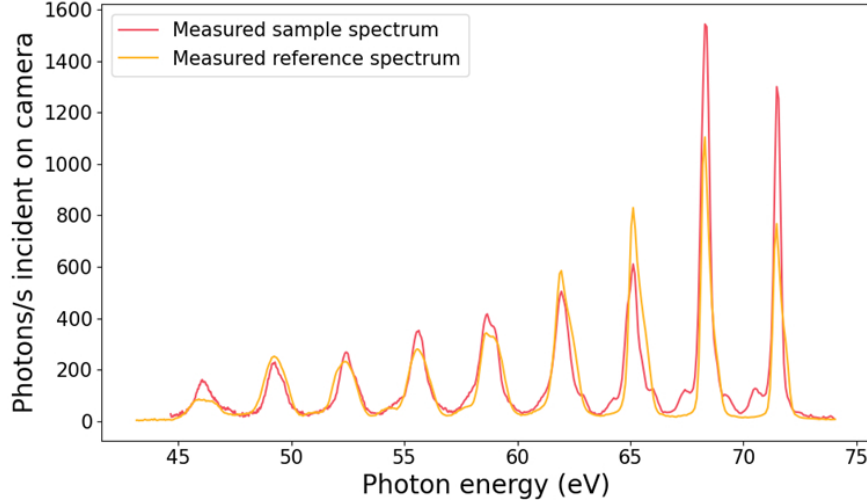
Figure 4.3: **Measured sample and reference spectra for a 5 nm Si_3N_4 / 5 nm Ni / SiO_2 sample.** Note that the TMOKE measurement geometry requires that the sample spectrum must be measured with a sample in-line. The CCD cameras can operate with the same settings and exposure times because the HHG flux on both cameras is comparable. The intensity variations across the sample spectrum relative to the reference spectrum are due to the presence of different optics in the sample and reference spectrometers, and do not affect the ability to normalize the HHG fluctuations. The slight "shoulders" in the sample spectrum come from sample imperfections. For both spectra, the spectral resolution is reduced at lower energies because the spectrometer focuses onto a circle while the detector is flat, leading to lower energies being further from the focus than higher energies. This can be corrected by using a flat field grating spectrometer. Camera counts were converted to photon flux by using the energy dependent quantum efficiency and electron-hole pair generation for these detectors.

We probe the femtosecond laser-induced spin dynamics of the sample by using the EUV transverse magneto-optical Kerr effect (EUV TMOKE), as described in Chapters 2.7 and 2.9. We spectrally resolve the EUV TMOKE signal, allowing us to access transitions from the $3p$ orbital to final states above and below the Fermi level in the valence shell.

Finally, this setup also allows for high-sensitivity studies of hot electron and acoustic dynamics [94]. These capabilities are important for understanding the full properties of magnetic

thin films, including transport, mechanical and magnetic properties. To measure these nonmagnetic properties, transient reflectivity measurements in s-polarization must be implemented. The setup shown in Figure 4.1 enables such measurements by making it possible to rotate the EUV polarization relative to the sample, simply by rotating the polarization of the driving laser beam. This is impossible if polarization sensitive optics are used to separate the EUV from driving laser.

4.3   Experimental setup and photographs

Here I describe my setup for implementing near-shot-noise limited spectroscopic EUV reflectivity and TMOKE measurements to precisely capture ultrafast magnetic dynamics in reflection mode. I also show photographs of the beamline to show how this instrument is implemented in the laboratory.

4.3.1   The laser system and high-harmonic generation (HHG)

We generate $\sim$50 fs laser pulses centered at 780 nm at a 5 kHz repetition rate using a commercial cryo-cooled Ti:sapphire regenerative laser amplifier (KM Labs Wyvern). We can tune the laser pulse energy between 0.2-2 mJ using a $\lambda/2$ waveplate and a pair of thin film polarizers. The amplified pulse has 0.7% shot-to-shot RMS intensity noise. The beam position and pointing are locked using a closed-loop feedback system involving 2 piezo-actuated mirror mounts and a pair of cameras that images the beam in-focus and out-of-focus. This beam stabilization system maintains the beam position to within < 3 μm and the beam pointing to within < 5 μrad indefinitely.

The amplified pulse is split to generate the laser pump and EUV probe pulses, with 90% of the power used for the probe arm, and 10% of the power used for the pump pulse. The EUV probe pulse is generated by focusing 1.44 mJ of laser energy (using a 50 cm CaF_2 lens), in a $\sim$50 fs pulse duration, to a 96 μm spot size ($1/e^2$, central lobe) into a Ne filled semi-infinite gas cell at a pressure of 140 torr. The 96 μm focal spot size is attained by adjusting the aperture of an iris placed immediately after the lens. The focused laser intensity of 5×10^{14} W/cm^2 is chosen to achieve critical ionization near the peak of the laser pulse for the Ne gas HHG medium (ionization

potential 21.56 eV and critical ionization of 1% for a 780 nm driving laser). This gas pressure balances between driving a sufficient number of emitters to ensure a strong HHG signal, mitigating ionization-induced defocusing and phase-mismatch due to the presence of a plasma, and reducing residual absorption of the harmonics by the gas medium. This gas pressure is controlled with an electronic needle-valve pressure regulator (MKS TYPE 640), tunable from 10 to 100 or 100 to 1000 torr.
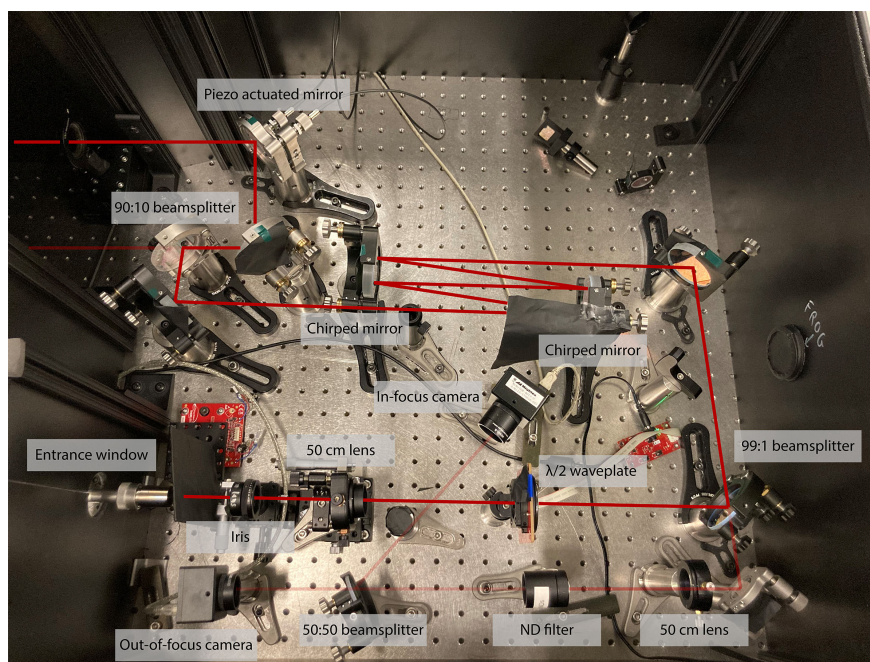
Figure 4.4: **Delivery of the laser beam to the semi-infinite gas cell (SIGC) for HHG.** The beam is vertically polarized relative to the table. Two piezo actuated mirrors (only the second is shown here, the first is inside the amplifier before the compressor gratings) control the beam pointing together with two cameras that image the beam in-focus and out-of-focus. A 90:10 beamsplitter lets us generate both a probe beam (90% of the total laser power) and a pump beam (10% of the total laser power). Chirped mirrors perform the final stages of pulse compression. The $\lambda/2$ waveplate lets us rotate the polarization to any angle, writing that polarization onto the EUV beam. The lens focuses the beam, and the iris apertures it. The beam then passes into the SIGC containing $\sim$140 torr Ne through the entrance window.

After the semi-infinite gas cell (SIGC), the beam exits into a vacuum chamber with a 1600 L/s turbo-pump (Leybold Oerlikon Mag W 2010 C) without any intermediate high pressure regions, allowing for the steepest possible pressure gradient after the copper or stainless steel exit foil to reduce reabsorption of the EUV light. The HHG flux from the semi-infinite gas cell is $\sim 10^{10}$ photons per second per harmonic, measured immediately after the aluminum filter using a NIST calibrated EUV photodiode. We calibrate the throughput of each filter by adding a second filter, measuring the flux, then removing the first filter and measuring the flux again. The beam delivery to the SIGC is shown in Figure 4.4 (without the waveplate and thin film polarizers that are placed immediately after the amplifier exit). Including filter attenuation and losses due to detector quantum efficiency, the beamline transmission for each arm $\sim 2 \times 10^{-7}$ in p-polarization and $\sim 4 \times 10^{-6}$ for s-polarization, for a total beamline transmission of $\sim 4 \times 10^{-7}$ and $\sim 8 \times 10^{-6}$, respectively.

4.3.2   Pump arm

A beamsplitter allows for 10% of the amplified pulse to be transmitted for use as a pump-beam, while the rest of the beam is used for generating the EUV probe, as described above. The pump beam intensity is electronically controlled by a combination of a $\lambda/2$ waveplate (mounted in a Newport AG-PR100P), thin film polarizer, and transmission polarizer. After intensity control, we use a motorized linear translation stage (Aerotech ANT130-110-L-25DU-MP) and a retroreflector to adjust the timing of the pump pulses relative to the probe. We set the pump beam polarization relative to the sample using an additional $\lambda/2$ waveplate, and we control the spot size on the sample with a 1 m lens. The 780 nm pump beam is p-polarized relative to the sample, is aligned to a near-collinear path with the EUV probe beam, and enters the vacuum system through a 0.5 mm thick anti-reflection-coated CaF_2 window.

4.3.3   Sample environment

The sample is glued to a thin sapphire disk (0.5 mm thickness x 15.875 mm diameter, Meller Optics). This disk is pressure fit into a custom ceramic mount and the mount is attached to a 3-axis positioning stage (SmarAct XYZ-SLC17:30). The entire assembly is held under vacuum at roughly 2×10^{-5} torr. We use a camera to view the sample and to spatially overlap the pump and probe beams, where the probe arm is aligned by removing the aluminum filter and using the red driving laser beam as a proxy. Temporal overlap between the IR pump and IR/EUV probe beams is achieved using a β-barium borate (BBO) crystal to generate second harmonic light. The sample and positioner are housed in a custom vacuum chamber that allows for a 35-45° angle of incidence of the pump and probe beams, and for easy application of an in-plane magnetic field up to 200 mT using an out-of-vacuum projection field electromagnet (GMW Magnet Systems, Model 5201).

4.3.4   EUV beam delivery and spectrometers

After the exiting the HHG cell, the infrared driving laser and EUV beams co-propagate 2 m in vacuum to a 12 mm stainless steel aperture, which rejects the majority of the driving laser. The EUV and the remainder of the driving laser are coincident on a 200 nm thick aluminum filter supported by a copper mesh (Luxel), which passes the EUV light below 72 eV and rejects the infrared laser light. The remaining EUV light is then focused by a gold toroidal mirror (13° angle of incidence, 50 cm focal length), and incident on a 1200 groove/mm grating (Richardson Gratings) with a 1° blaze in the conical dispersion configuration (referred to later as the reference grating). The zeroth order, which contains the full HHG spectral comb, is focused on the sample with a focal spot size of 58 x 64 um. After the zeroth order is reflected by the sample, it is incident on a 200 nm Al filter (to reject the collinear pump light), refocused by a toroid (B_4C, 12° angle of incidence, 27 cm focal length), and diffracted by a 1200 groove/mm grating (Richardson Gratings) with a 5.2° blaze in the conical dispersion configuration. The resultant spectrum is imaged with a spectroscopy format CCD (Andor Newton 940, BN coating).

The first order of the reference grating, which is spectrally dispersed, is reflected by a 45° gold mirror, passed through a 200 nm Al filter to block stray light from the pump beam, and focused onto a CCD camera (Andor Newton 940, BN coating) where it is used to monitor the spectral intensity of each tooth of the HHG comb and normalize the intensity fluctuations of the EUV source. The spectral resolution of both spectrometers is ∼0.5 eV at 71 eV, and sufficient to easily distinguish between adjacent harmonics that are separated by 3 eV.

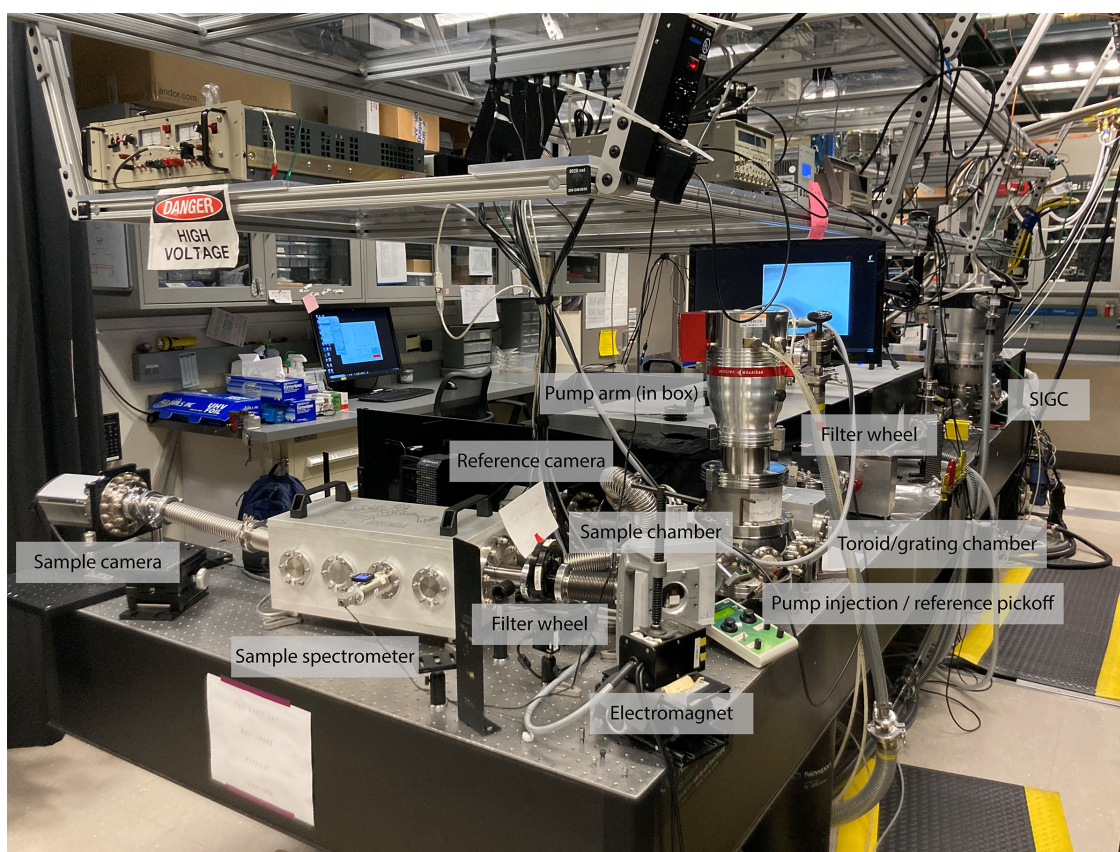A photograph of the EUV beamline is shown below in Figure 4.5:

Figure 4.5: **A photograph of the X-MATTER beamline.** The pump arm is contained within the labeled box to reduce air currents, and all the EUV optics are located inside their labeled vacuum chambers.

4.3.5   Noise analysis

Although HHG is the most extreme nonlinear optical process uncovered to date, good phase matching allows us to achieve 2-5% RMS intensity fluctuations with a 0.3 s exposure in this setup. The % RMS noise of a signal is equal to its standard deviation divided by its mean. This quantity provides a scale invariant measure of the signal-to-noise (or more precisely, noise-to-signal) ratio. To further reduce these intensity fluctuations, we implement a post-processing digital noise canceler by splitting the EUV beam and measuring the spectrum on two cameras (one reference camera placed before the sample, the other camera placed after the sample, see Figure 4.1). Once both spectra are obtained, we can bin the counts by energy into separate harmonic "teeth," and cancel the noise of each tooth independently.

In designing this noise reducing beamline, our objective is to use the measured noise of a reference signal to minimize intensity fluctuations of the sample signal. To minimize the sample signal's intensity fluctuations, we can write a simple equation that combines the measurements of these two signals:

$$\tilde{x}_s(t) = \frac{x_s(t)}{x_r(t)/\mu_r} \tag{4.1}$$

where $\tilde{x}_s(t)$ is the reduced noise sample signal at each time point, $x_s(t)$ is the original sample signal intensity at each time point, $x_r(t)$ is the noisy reference signal intensity at each time point, and μ_r is the mean of the reference signal intensity over time. Equation 4.1 shows that, to obtain the reduced noise sample signal, we divide the original sample signal $x_s(t)$ by the normalized reference signal $x_r(t)/\mu_r$. Normalizing the reference signal allows us to reduce the noise on the sample signal without changing its mean. We use Equation 4.1 throughout this paper to reduce the noise of our sample signal.

We can only cancel noise that is correlated between the reference camera and the sample camera. Some noise, like the photon shot noise, will remain uncorrelated and cannot be canceled. If we assume that all the correlated noise is canceled and the uncorrelated noise remains, we can

write the standard deviation of our noise-reduced signal as:

$$\sigma_{\tilde{x}_s} = \frac{1}{\mu_r} \sqrt{\sigma_r^2 \mu_s^2 + \sigma_s^2 \mu_r^2} \tag{4.2}$$

Where μ_r is the mean reference signal, μ_s is the mean sample signal, σ_s is the sample signal noise, and σ_r is the reference signal noise. If the photon shot noise is substantially larger than all other noise sources, the sample signal noise and reference signal are both well approximated by their respective photon shot noise. We can see this by writing the total signal noise for a single camera as:

$$\sigma_{singlecamera} = \sqrt{n_{shotnoise}^2 + n_{darkcurrent}^2 + n_{readout}^2 + n_{ADC}^2} \tag{4.3}$$

The photon shot noise is equal to the square root of the mean number of photons. The dark current noise is 0.01 electrons / pixel / second when operating at -60 °C, and the readout noise is 4.6 electrons per full vertical binned pixel (equivalent to 512 actual pixels). We operate the camera in full vertical binned mode, and assume that there is dark current and readout noise for any pixels in the total integrated region we analyze. The dark current noise and readout noise were attained from Andor's factory calibration. The quantization error n_{ADC} (also called analog-to-digital converter noise or ADC noise) is the error that occurs whenever an analog signal is discretized. This error can be modeled as a white noise source with $n_{ADC} = \sqrt{1/12}$ LSB [95], where LSB is the least significant bit (2^{-16} for our cameras). The exposure time is 0.3 s. With this exposure time, the photon shot noise dominates all other noise terms if there are more than 100 photons per harmonic.

If we divide Equation 4.2 by the total sample signal, we get the % RMS noise floor. By integrating the total flux across the 66 eV harmonic and across all harmonics in Fig. 4.6, we can calculate the shot noise of our measurement. Then, by combining the shot noise of both beams in Equation 4.2, we can compute the measurement noise floor. We calculate the noise floor of the measurement to be 2.78% RMS for a the 66 eV harmonic and 1.08% RMS for all harmonics in p-polarization with a 5 nm / Si_3N_4 / 5 nm Ni / SiO_2 sample. We can observe the actual intensity noise for a single harmonic and for all harmonics in Figure 4.6:
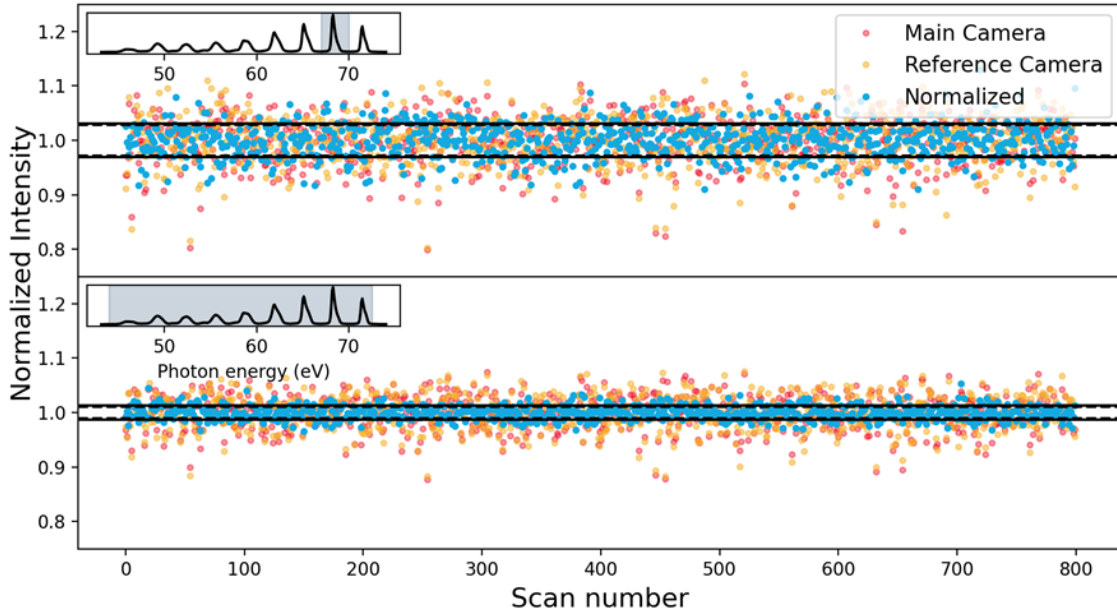
Figure 4.6: **Intensity normalization of the HHG signal.** Each point corresponds to a 0.3 s exposure containing 1500 EUV pulses. The top figure shows the normalization of a single 66 eV harmonic, and the bottom figure shows the normalization of all harmonics simultaneously. For the 66 eV harmonic, the % RMS noise on the sample camera is 4.29% before normalization and 3.19% after normalization. The % RMS noise of all harmonics on the sample camera is 3.06% before normalization and 1.18% after normalization. Note that, while the harmonic source is very stable without the normalization, large fluctuations are eliminated and long-term drifts are minimized.

By comparing our normalized intensity noise with the shot noise limit, we see that the intensity % RMS noise is within 15% of the noise limit for a single harmonic (3.19% measured vs 2.78% theoretical) and within 10% of the noise limit for all harmonics (1.18% measured vs 1.08% theoretical). Some of the unaccounted noise may come from slight energy shifts in the harmonics, for example associated with small fluctuations in the Ne ionization levels. Based on estimates of the reflectivity of our optics, we calculate that near the Ni M-edge, a 10 meV shift in the harmonic energy leads to a 0.1% change in the relative reflectivities of the sample spectrometer beam path and the reference beam path. Comparing the noise of a single harmonic with the noise of all harmonics demonstrates that our beamline operates near the shot noise limit over a wide range of

photon fluxes.

4.3.6 Time-resolved experimental results

To demonstrate the capability of our new instrument, we present time-resolved data on single element ferromagnets and magnetic alloys, including the fluence dependence of the magnetic dynamics, the presence of hot electron dynamics and acoustic waves, and ultrafast spin transfer between different magnetic elements. To perform these measurements, the samples were excited with a $\sim$50 fs, 780 nm pulse at various fluences.

a. Single element ferromagnets

We present measurements of a single element ferromagnet (5 nm Ni thin films) in order to demonstrate our capabilities for measuring fluence dependent magnetic dynamics, hot electron dynamics, and acoustic waves. The flux difference of the reflectivity measurements that compose a TMOKE measurement is the product of a sample's reflectivity and asymmetry. For this Ni sample, the s- and p-polarized reflectivities between 40 eV and 72 eV average 0.03 and 0.003 respectively, while the static asymmetry is 14%. With this relatively large asymmetry, high quality time-resolved TMOKE data can be acquired in under 1 hour using this setup.

i. Fluence dependent demagnetization

To observe laser-induced magnetization dynamics, we pump the sample with a ~ 50 fs pulse at 780 nm and measure the EUV TMOKE asymmetry at a given time delay between the infrared pump and the EUV probe, as seen below in Figure 4.7:
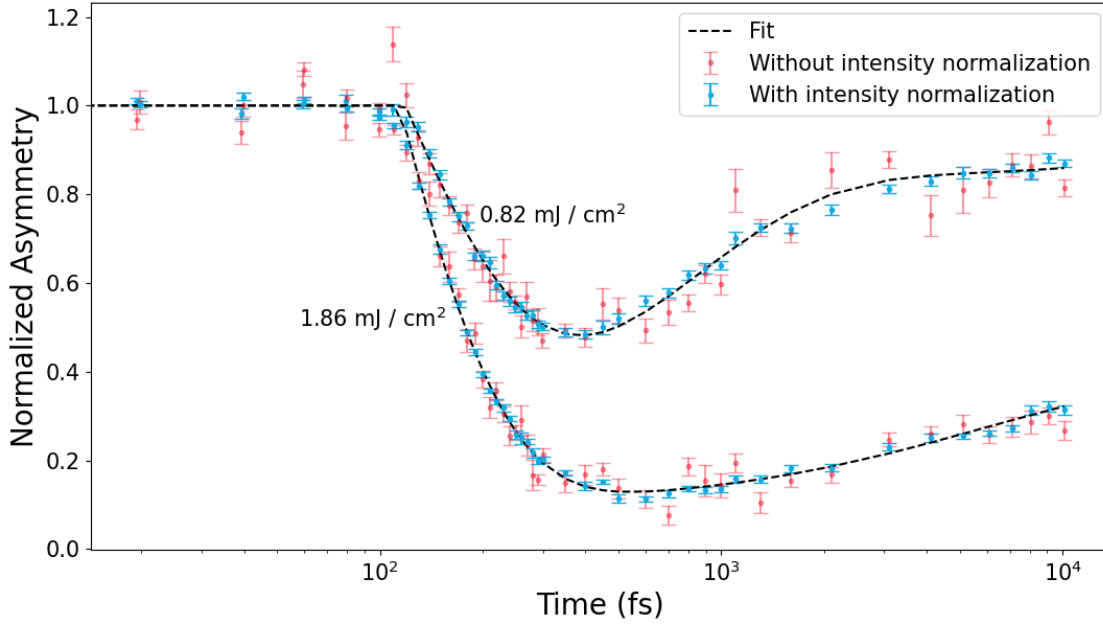
Figure 4.7: **Time-resolved EUV TMOKE data for a 5 nm Si$_3$N$_4$ / 5 nm Ni / SiO$_2$ sample, using the selected region shown in Figure 2.18.** The x-axis is on a log scale. The blue intensity-normalized data points have smaller error bars than the red, non-normalized, data points. The pump is incident on the sample at t=100 fs. At different pump fluences, the sample behaves differently, as expected: (top curve) three timescales are present for a low pump fluence below that required to completely drive a ferromagnetic to paramagnetic phase transition – a fast demagnetization, a fast recovery, and a slow recovery; (lower curve) only two timescales are present above the critical fluence – a fast demagnetization and a slow recovery, as shown previously [80]. The error bars show the standard error. The data shown here uses a slightly different noise reduction method than the one described in Equation 4.1; for the data shown here, the noise of the sample spectrometer is rescaled to match the noise of the reference spectrometer before the normalization occurs, although the difference between these two algorithms is imperceptible in this case.

In Figure 4.7, we fit the TMOKE data to a three-exponential curve:

$$1 + \Theta(t - t_0)\left[A_1 e^{-(t-t_0)/\tau_1} - A_2 e^{-(t-t_0)/\tau_2} - A_3 e^{-(t-t_0)/\tau_3}\right] \tag{4.4}$$

Here, Θ represents the Heaviside step function and allows the three exponential behavior to begin at t_0. This three-exponential curve is a phenomenological model describing the behavior of the magnetism of the system, as validated by recent correlated ARPES and EUV TMOKE measurements. As expected, we note that the behavior of the magnetization dynamics varies significantly with laser pump power - this is because to drive a full ferromagnetic to paramagnetic phase transition in nickel [80, 61], the laser fluence must exceed a critical fluence that drives the hot electron bath to temperatures at or beyond the Curie temperature. We note also that the time delays in Figure 4.7 (and in Figure 4.8) are taken in a random order to ensure that sample damage or long-term drift do not influence these measurements. We observe a clear improvement in data quality based on our HHG intensity normalization procedure and an improvement in fitting accuracy. Quantitatively, the demagnetization timescale associated with the 0.82 mJ/cm^2 pump pulse (below critical) is estimated to be 104 ± 22 fs without intensity normalization and 96 ± 6 fs with intensity normalization. The demagnetization timescale associated with the 1.86 mJ/cm^2 (above critical) pump pulse is estimated to be 77 ± 6 fs without intensity normalization and 79 ± 2 fs with intensity normalization. These estimates correspond to a 3-4x increase in the accuracy of demagnetization timescale estimation.

ii. Transient reflectivity – observing hot electrons and acoustic waves

In addition to time-resolved EUV TMOKE for the element-specific magnetic state, we can measure the time-resolved reflectivity of s-polarized light at multiple harmonic energies from our sample, which gives us access to both the excited electronic (i.e. hot electrons) and acoustic dynamics, as has been shown previously [94, 96, 97]. We observe a significant improvement in the data quality for the time-resolved reflectivity data, which manifests most obviously as a greatly reduced number of outlier data points. The harmonic near 65 eV probes the M-edge transition closest to the Fermi energy, and a fast reflectivity spike corresponding to hot electron excitation is clearly visible in the s-polarized reflectivity data. In the time-resolved reflectivity data at all energies, we can see oscillations corresponding to acoustic waves. The time-resolved reflectivity data is shown

below in Figure 4.8:
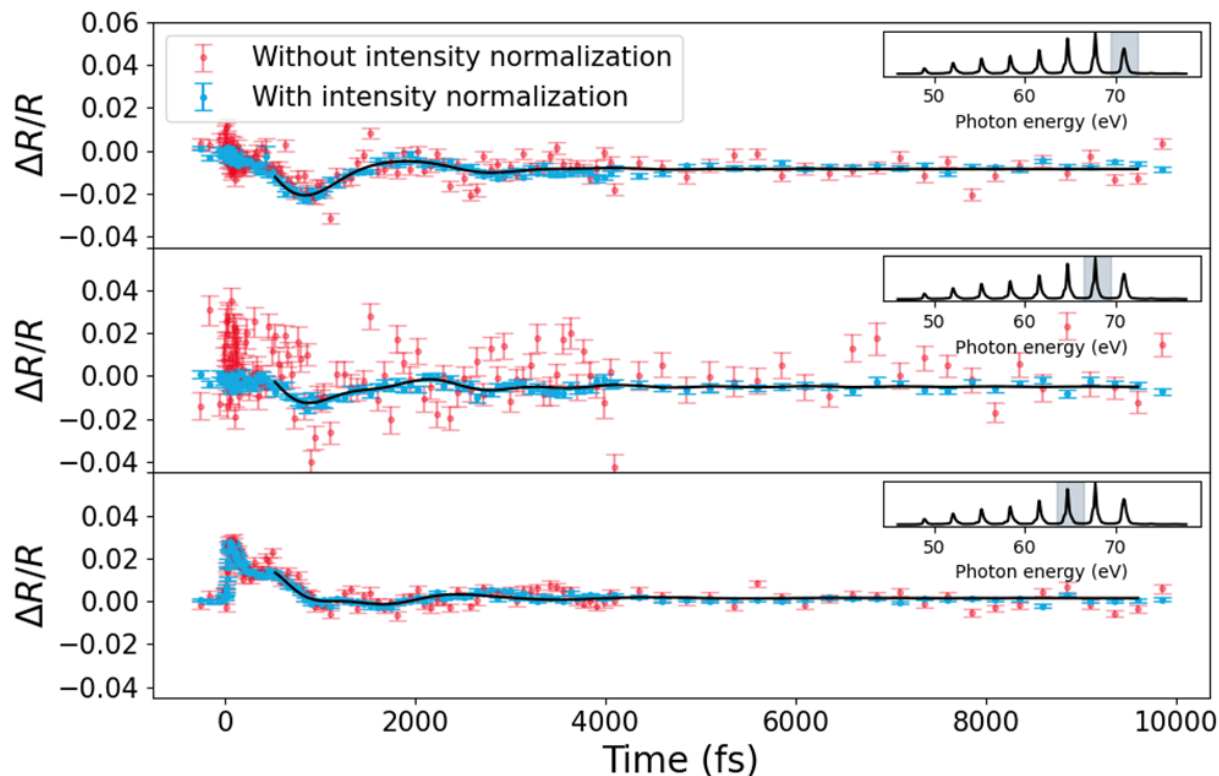
Figure 4.8: **Change in reflectivity of different s-polarized high harmonic photon energies of the 5 nm Si$_3$N$_4$ / 10 nm Ni / SiO$_2$ sample after pumping with a laser pulse with 1.6 eV photon energy and a fluence of 1.86 mJ / cm^2.** The laser pump pulse is incident on the sample at t=0 fs. The error bars show the standard error. The solid black lines show the fit to a sum of two exponentially decaying sinusoids corresponding to acoustic modes in Ni and in Si$_3$N$_4$.

By fitting these oscillations to exponentially decaying sinusoids corresponding to acoustic oscillations based on the speed of sound in our sample, this technique may therefore offer an approximate non-destructive in-situ confirmation of film thickness, which is important for fluence absorption calculations in all magnetic pump-probe experiments. We note that extremely accurate characterizations of film thickness can be performed with variable angle EUV reflectometry measurements [98]. If we take the Fourier transform of the intensity normalized reflectivity data in

Figure 4.8 (blue points), we can confirm that the measured acoustic waves are consistent with the sample composition and geometry, as seen below in in Figure 4.8.
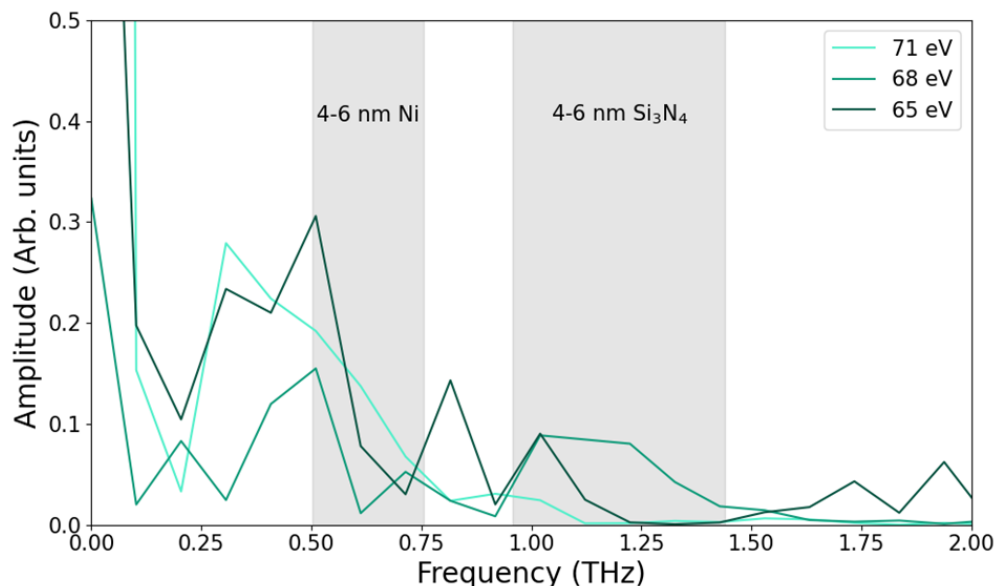
Figure 4.9: **Fourier transform of the time-resolved s-polarized reflectivity data in Figure 4.8.** We display in gray the windows of the acoustic frequencies corresponding to calculated acoustic wave periods in 4-6 nm thick Ni and Si_3N_4, based on longitudinal acoustic velocities of 6040 m/s [99] and 11500 m/s [100], respectively. We observe spectral density corresponding these acoustic wave periods. Before applying the Fourier transform to the data in Figure 4.8, we apply a Savitzky-Golay filter with polynomial degree 7 and a 21 time point window and then interpolate onto linearly spaced points in time. (The data in this figure is actually the Fourier transform of the data in Figure 4.8 *after the sample signal noise was rescaled to match the reference signal, and then normalized.* This resulted in barely perceptible differences in the normalization, and so the Fourier analysis was not repeated for the case where the sample signal noise was not rescaled.)

The acoustic oscillations observed in the s-polarized reflectivity data are consistent with the sample geometry and may even indicate that the Ni and Si_3N_4 layers are both slightly thicker than 5 nm, since that is where we see the greatest spectral density. There may also be variability

in the acoustic velocity due to thin film effects. We fit the data in Figure 4.8 to two sinusoidal oscillations that decay exponentially; one oscillation has a period corresponding to 2 ps for Ni, and the other has a period corresponding to 0.98 ps for Si_3N_4. The amplitudes and relative phases of the sinusoids, as well as the exponential decay and an overall offset, vary as a fit parameters.

b. Magnetic compounds and ultrafast light induced spin transfer

Next, we present measurements of a magnetic Heusler compound (Co_2MnGe) in order to demonstrate the capability of this setup to measure small changes in sample magnetization in a multi-element sample. In Figure 4.10 below, we show low-noise measurement of light-induced spin transfer in Co_2MnGe, achieving better data quality than in our previous work [25]. For this Co_2MnGe sample, the s- and p-polarized reflectivities between 40 and 72 eV are 0.03 and 0.003 respectively, while the static asymmetries of Co and Mn in the magnetic Heusler alloy Co_2MnGe are 2.5% and 4%, respectively. With these small asymmetries and reflectivities, such a sample is challenging to measure without a way to eliminate HHG intensity fluctuations.

We observe a transient enhancement of the Co signal at 40 fs, which is indicative of light-induced spin transfer between the Mn and Co sublattices [25]. This transient enhancement is 6% of the Co asymmetry, corresponding to an absolute difference in asymmetry of 0.15%. We obtained this data over the course of $\sim$2 days without adjusting the setup, demonstrating the long-term stability of our instrument. To observe these same dynamics in the data without noise cancellation would require a roughly 15x longer acquisition time (a few weeks), as indicated by the large error bars on the time-resolved Co asymmetry without intensity normalization.
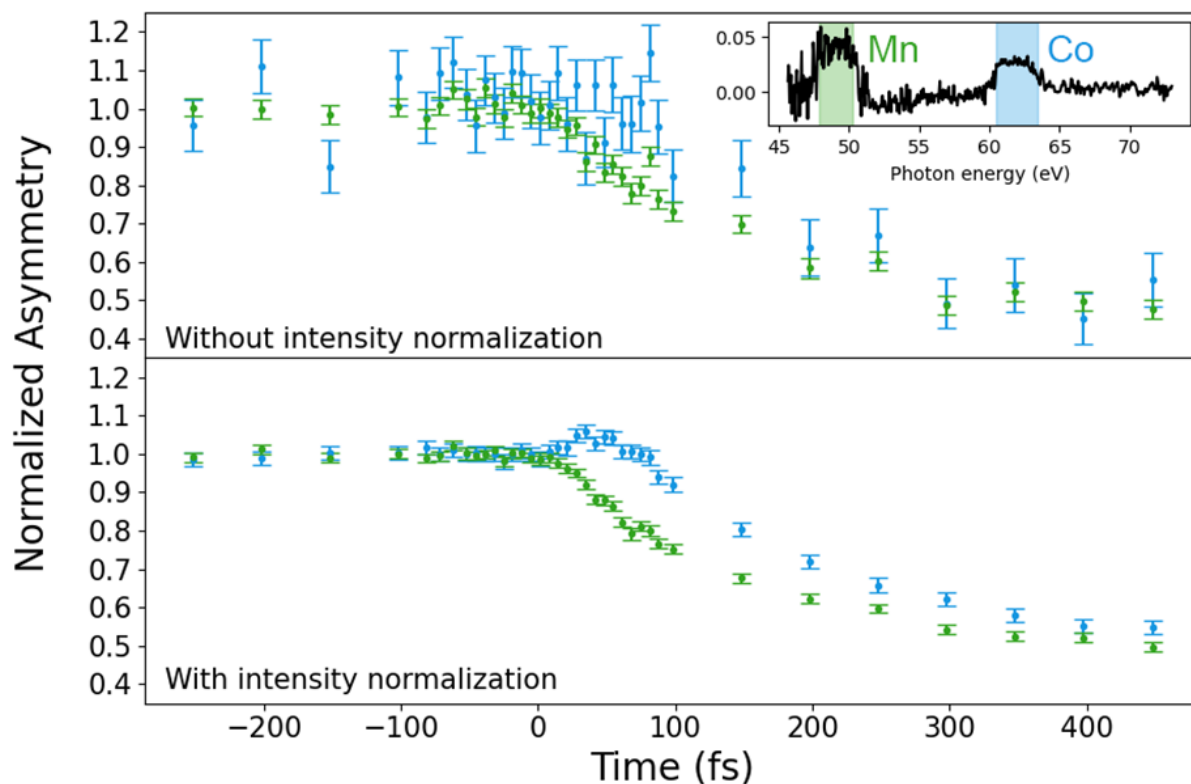
Figure 4.10: **Magnetization dynamics of the Co and Mn in the Co$_2$MnGe Heusler alloy, showing how optical pumping directly and immediately transfers magnetization from Mn (green) to Co (blue).** The laser pump pulse is incident on the sample at t=0 fs. The inset shows the static asymmetry of the sample and highlights which parts are used for determining a given element's magnetization. Both data sets were acquired over the same 40-hour time period and contain the same non-normalized sample spectrometer data. The lower plot uses the reference spectrometer to normalize intensity fluctuations, improving the data quality substantially.

Chapter 5

Ultrafast dynamics of Heusler Compounds

In this chapter, I will discuss measurements of Heusler made with the X-MATTER beamline from Chapter 4. I will first describe the crystalline structure, electronic properties, and magnetic properties of Heuslers. I will then discuss two specific Heusler compounds in detail (NiMnSb and Co_2MnGa), along with measurements of their ultrafast magnetic and electronic dynamics. The measurement of the ultrafast magnetic and electronic dynamics in these compounds is the second main achievement of this thesis. Nevertheless, the experimental results in this section are thus far unpublished and some of the interpretation of the data remains uncertain.

5.1   What are Heuslers?

Heuslers are a class of ternary alloys discovered by Fritz Heusler. He synthesized the alloy Cu_2MnAl and realized that it has a remarkable property: it is ferromagnetic *despite* the fact that none of its constituent elements is ferromagnetic! Altogether, there are now more than 1000 Heusler compounds in existence. These Heuslers exhibit interesting properties including magnetocaloric effects [101], superconductivty [102], half-metallicity [103, 104], semiconductivity [105], and topological electronic states [106, 107]. These Heusler alloys may also be useful in spintronic applications because of the prevalence of high spin polarization at their Fermi energy. Amazingly, many of the Heusler's properties can be predicted simply by counting its valence electrons. We will discuss the crystal structure and the simple rules for determining some of the properties of many Heusler compounds here, following the excellent review of Graf *et al.* [108].

Structurally, Heuslers take the form X_2YZ or XYZ, with the former sometimes referred to as full-Heuslers and the latter as half-Heuslers. The X and Y elements are considered to have a cationic character, and the Z element an anionic character. Thus, the Heusler compounds can be broken into sublattices consisting of a covalent part (X_2Y), and an ionic part (X_2Z, YZ). The elements that can be chosen for positions X, Y, and Z, as well as the crystal structure for half-Heuslers and Heuslers, are shown below in Figure 5.1:

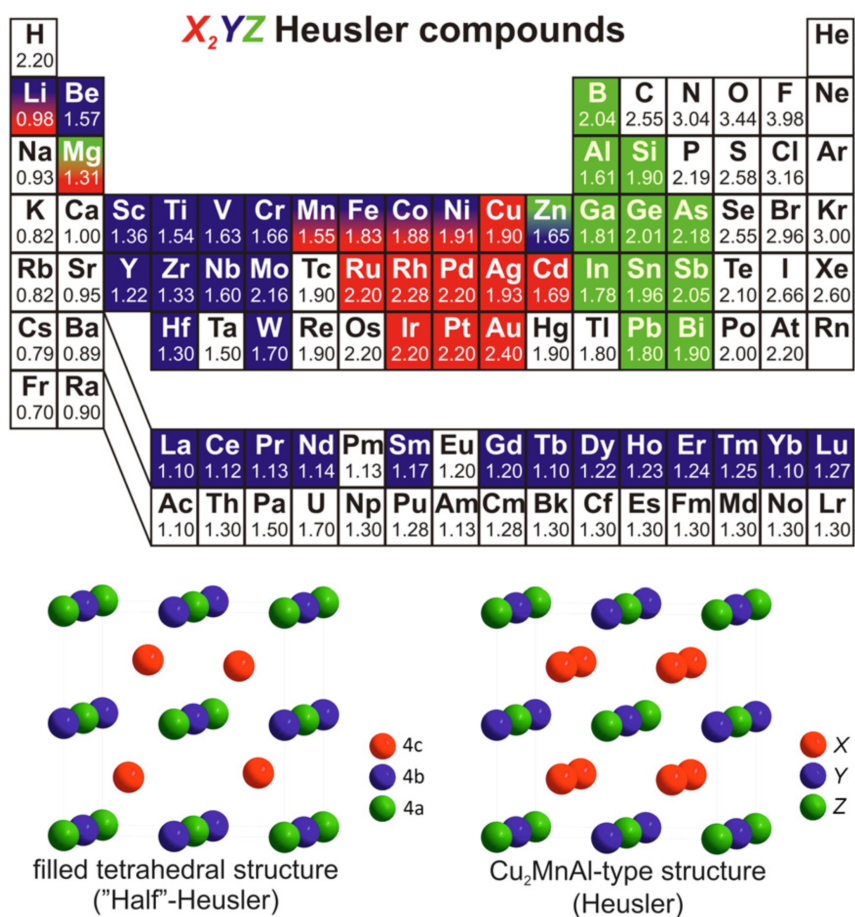Figure 5.1: **The Heusler periodic table and crystal structure.** The top figure shows the periodic table of elements, highlighting which elements can be used in which positions of the Heusler compound. There are an enormous number of potential compounds that can be formed by these elements. The bottom figure shows the crystal structure of half-Heusler and full-Heusler compounds. Figure adapted from [108].

Half-Heusler compounds with 8 electrons are semiconductors in what is referred to as a Nowotny-Juza phase [109, 110, 111]. Half-Heusler compounds 18 valence electrons ($V_E = 18$) are also semiconductors and can be modeled as having no valence electrons on X, a d^{10} configuration for Y and a s^2p^6 configuration for Z [112]. The closed shell configuration leads to their particular stability, and since all the shells are either completely full or completely empty, they are diamagnetic semiconductors. Deviating from $V_E = 18$ leads to instability, except in cases where a rare earth element allows for additional valence electrons in the $4f$ orbital, and in the case of NiMnSb, which has 4 electrons in the manganese $3d$ orbital. In both the case of rare earth half-Heuslers and NiMnSb, the high degree of localization for the additional valence electrons is essential for the compound's stability. Because of its 4 extra d electrons, NiMnSb has a magnetic moment of $4\mu_B$ per unit cell.

For full-Heuslers, compounds with $V_E = 24$ are semiconductors. The full-Heuslers obey the Slater-Pauling rule for localized magnetic moments, and the magnetic moment of a single unit cell in a full-Heusler compound is given by $m = V_E - 24$, as shown for the Co$_2$YZ compounds in Figure 5.2 below:
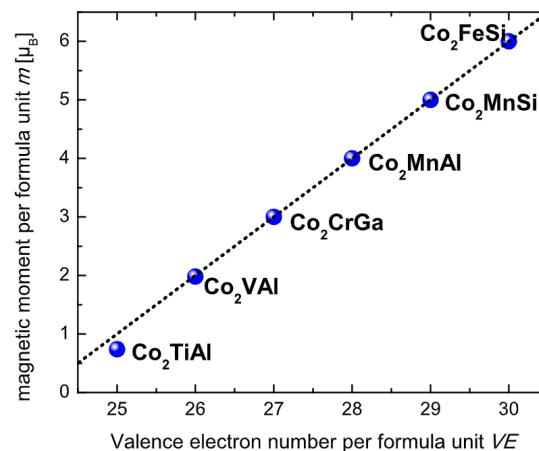

Figure 5.2: **Comparison of the Slater-Pauling curve and the magnetic moment of Co$_2$YZ compounds.** The blue dots are measured magnetic moments and the dotted line is the theoretical prediction for the magnetic moment based on the Slater-Pauling rule. Figure adapted from [108].

Full- and half-Heuslers are additionally distinguished by the distribution of their magnetic moments throughout the unit cell. Half-Heuslers have a magnetic moment only on atoms occupying the octahetral sites. In the full-Heusler, the two atoms occupying the tetrahedral sites can have a magnetic interaction, and this interaction creates a second magnetic sublattice distinct from the octahedral magnetic sublattice. Due to these two distinct magnetic sublattices, more types of magnetic order are possible in full-Heuslers than in half-Heuslers.
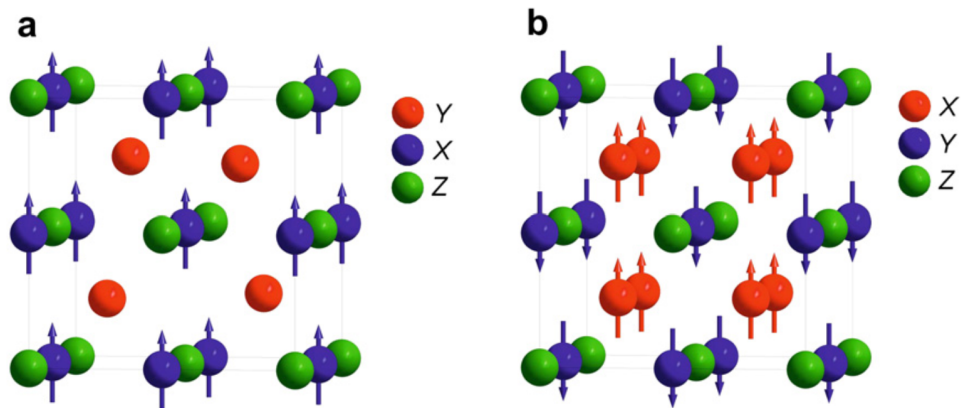
Figure 5.3: **(a) The magnetic sublattice of a half-Heusler, and (b) the multiple magnetic sublattices of a full-Heusler.** Note that, while the spins on X and Y are anti-aligned in (b), this is only one possibility and is not always the case. Figure adapted from [108].

As a note of subtlety, although the half-Heuslers nominally have a magnetic moment on the octahedral sites, the tetrahedral sites can in fact carry a much smaller induced magnetic moment, as is the case in NiMnSb [113, 114].

Both full- and half-Heuslers can exhibit half-metallic ferromagnetism, whereby the material is conducting for the majority spin orientation and insulating (or semiconducting) for the minority spin orientation. A strong imbalance of the density of states below the Fermi energy always causes these half-metallic materials to exhibit ferromagnetism. The densities of states near the Fermi energy for metallic ferromagnets and half-metallic ferromagnets are compared below in Figure 5.4:
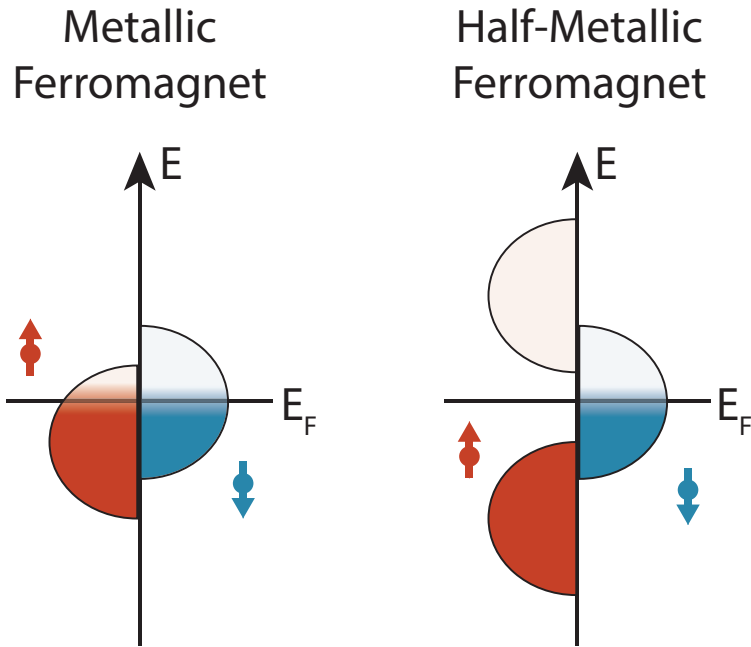
Figure 5.4: **Comparison of the density of states near the Fermi energy for a metallic ferromagnet and a half-metallic ferromagnet.** The metallic ferromagnetic is conducting for both majority and minority spins, and the half-metallic ferromagnetic is conducting only for the minority spins - in its majority spin state, it has an energy gap near E_F.

In considering the half-metallic character of a material, we can define it's spin polarization at the Fermi energy:

$$P(E_F) = \frac{N_\uparrow(E_F) - N_\downarrow(E_F)}{N_\uparrow(E_F) + N_\downarrow(E_F)} \tag{5.1}$$

We can clearly see that the spin polarization is simply the fraction of electrons that are spin up (or spin down), and the value can range from -100% to $+100\%$. A true half-metallic ferromagnet should have $P(E_F) = \pm 100\%$.

Finally, let us consider disorder in the crystal structure of these Heusler compounds. Figure 5.5 shows the possible types of disorder for full- and half-Heusler compounds.
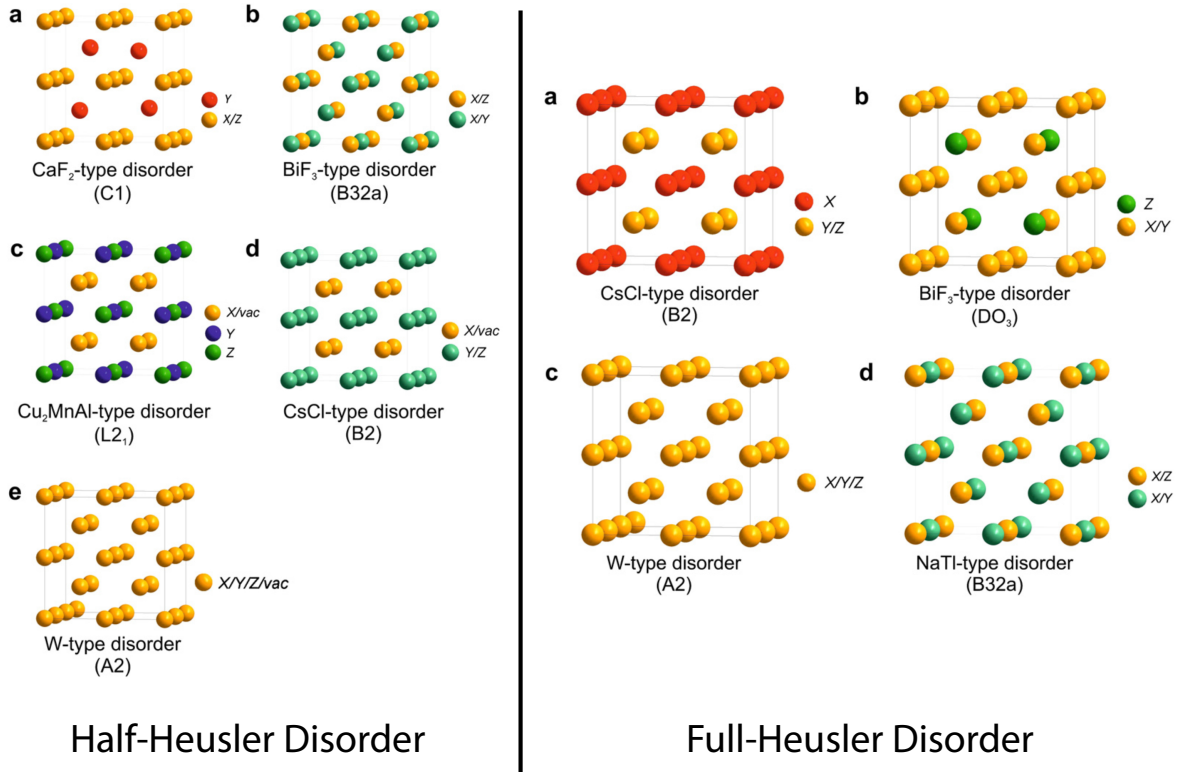
Figure 5.5: **Classifications of intersite disorder shown for half-Heuslers on the left and full-Heuslers on the right.** Figure adapted from [108].

The electronic structure of Heuslers is strongly dependent on the arrangement of atoms in the crystal lattice, and so disorder in Heuslers can substantially alter their electronic and magnetic properties. For example, the band gap of TiNiSn can close in the presence of $L2_1$ or C1 disorder [108], and Co_2MnGe maintains its half-metallic character in the B2 phase, but not in the A2 phase [25]. Since this thesis is not focused on the growth and characterization of samples, I will not discuss methods for structural determination here, but the interested reader is encouraged to consult Graf *et al.* for more information [108].

With a basic understanding of Heuslers' crystal structure, electronic and magnetic properties, we are now ready to examine the ultrafast laser induced spin and charge dynamics of these interesting materials.

5.2   NiMnSb

NiMnSb is a half-Heusler with 22 valence electrons, $C1_b$ crystal structure, a saturation magnetic moment of 4.04 μ_B / unit formula, and a Curie temperature of 732 K [115]. It is a half metallic ferromagnet with 100% spin polarization at the Fermi level and an energy gap around the Fermi level in the majority spin state of ~0.5 eV. The magnetic moment of the Mn atoms is expected to be highly localized due to the strong localization of the $3d$ electrons in Mn. The magnetic moments of the Ni and Sb atoms are predicted to be induced by the Mn moments [113, 114]. These small induced moments may be changed by temperature or structural changes, and the half-metallicity of the material can be affected by mechanical strain [116]. The magnetic moments of Ni, Mn, and Sb as measured or calculated by different references are shown below in Table 5.1

Ni (μ_B)	Mn (μ_B)	Sb (μ_B)	Temperature	Theory / Experiment	Reference
0.18 ± 0.02	3.79 ± 0.02	-	10 K	Experiment	[117]
0.19 ± 0.02	3.55 ± 0.02	-	260 K	Experiment	[117]
0.20	3.85	-0.10	0 K	Theory	[114]
0.25	3.72	-0.07	0 K	Theory	[104]

Table 5.1: **Atomic magnetic moments of NiMnSb.**

While there is generally good agreement here between theory and experiment, some temperature dependent XMCD measurements show a nearly 50% decrease of atomic magnetic moment as the temperature is increased from 50 K to 200 K [118], in disagreement with the neutron scattering measurements presented in [117]. I am not aware of room temperature measurements or high temperature measurements of the individual atomic moments for NiMnSb.

Using density functional theory (DFT), it is possible to calculate the element resolved density of states (DOS). The element resolved DOS and crystal structure for NiMnSb are shown below in Figure 5.6:
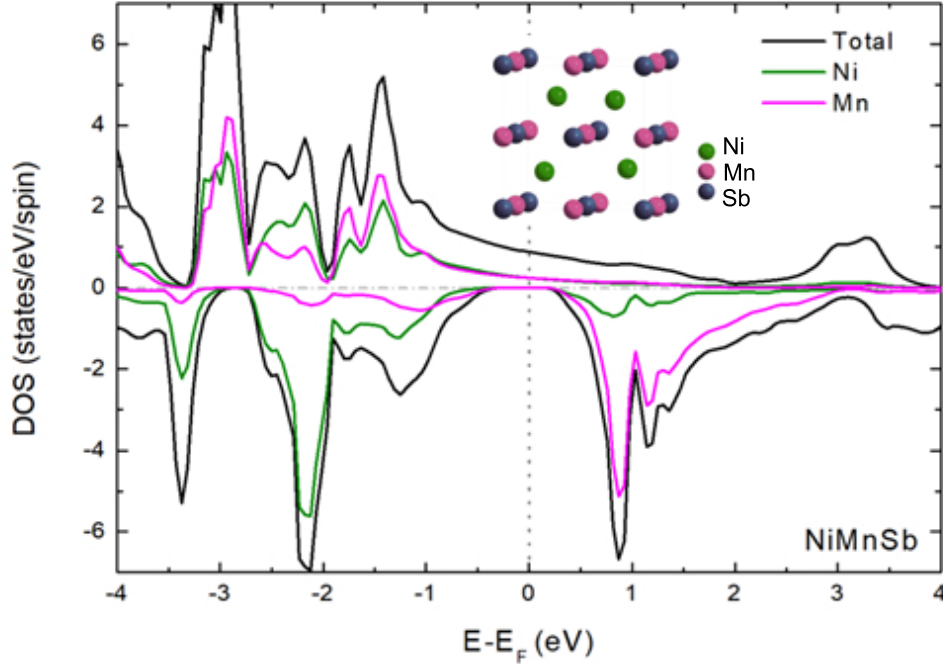
Figure 5.6: **Ground state density of states and crystal structure for the half-metallic half-Heusler NiMnSb.** A large band gap is apparent in the minority spin states. Theory predicts that the Sb moment is antiferromagnetically ordered relative to the Mn moment, while the Ni and Mn moments are ordered ferromagnetically. Figure adapted from [83].

By examining the element resolved density of states in Figure 5.6, we can see that the ground state Fermi energy lies between Ni and Mn d-states, and thus we expect that optically pumping spins from one sublattice to another should be possible if we choose the correct photon energy (see Section 2.5.4). Indeed, Steil *et al.* predicted that a large optically induced spin transfer (OISTR) should be present for a 1.5 eV pump photon energy for NiMnSb, as shown below in Figure 5.7 [83]. Note that, while the magnetic moment of the Ni is expected to increase by 40-60% relative to its initial value and the magnetic moment of the Mn is expected to decrase by 10-15% relative to its initial value, the absolute change in the Mn moment is still larger than the change in the Ni moment.
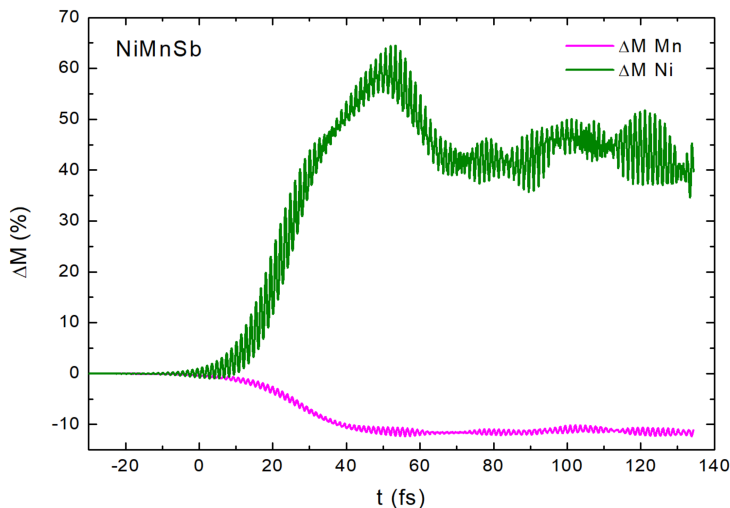
Figure 5.7: **Time domain density functional theory (TD-DFT) calculations for the relative change in magnetic moment on Ni and Mn in the half-Heusler NiMnSb.** We see an increase on the magnetic moment on the Ni of 40-50%, and a corresponding decrease on the Mn sublattice of 10-15%. Figure adapted from [83, Supplemental Information].

These theoretical calculations show the largest predicted relative OISTR signal of any material (Ni magnetization increase of $\sim$50% after pumping with 800 nm light in NiMnSb, 5-10x more than the $\sim$7% increase in Co magnetization observed in Co_2MnGa after pumping with 800 nm light [25]). To test these theoretical OISTR predictions, Steil *et al.* measured the ultrafast laser induced spin dynamics of NiMnSb using a 60 fs bichromatic 800 nm pump, 400 nm probe setup [83].
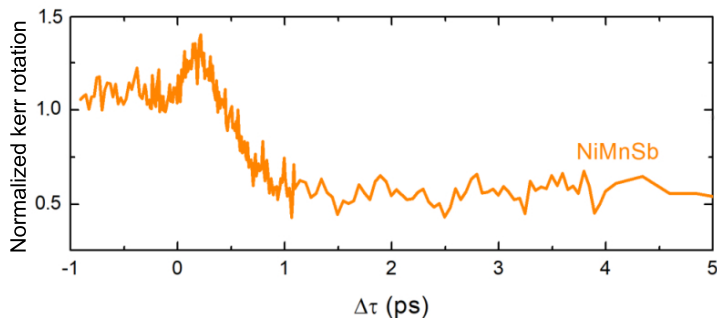
Figure 5.8: **Demagnetization of NiMnSb measured with MOKE at 400 nm.** Figure adapted from [83].

There is a clear increase in Kerr rotation from 0-100 fs, corresponding to an increase in magnetization. Since the probe wavelength is 400 nm and visible MOKE is not element selective, it is unclear which elements contribute most strongly to the MOKE signal. Element specific measurements are needed to determine the full picture of the magnetic dynamics in this material, and I will present such measurements in the next section.

5.2.1   EUV TMOKE measurements of NiMnSb

We measured a thin film NiMnSb sample with a structure of 2 nm Ru / 13 nm NiMnSb / (In,Ga)As / InP:Fe (top to bottom) using two complimentary HHG setups: the setup described in Chapter 4, and Möller *et al.*'s setup at the University of Göttingen, as described in [88]. The harmonic comb in our HHG setup has an energy spacing of 3.16 eV between teeth, and the harmonic comb in the Göttingen setup has an energy spacing of 2.4 eV between teeth. Each setup has a harmonic bandwidth of $\sim$100 meV. Combining the measurements of these two setups allows us to sample the material's band structure more finely than either measurement could accomplish independently. Importantly, these setups use two slightly different angles of incidence: our setup in Boulder uses a 40° angle of incidence (AOI) from grazing, and the setup in Göttingen uses a 45° AOI. Changing the angle of incidence can change the shape of the asymmetry, as demonstrated in [119].

The ground state TMOKE asymmetry can be calculated using DFT and compared to the ground state measurements from our EUV TMOKE setup and the EUV TMOKE setup in Göttingen. For reference, the Sb $N4/N5$ edge ($4d \rightarrow$ valence transition) is located at ~ 33 eV, the Mn $M2/M3$ edge ($3p \rightarrow$ valence transition) is located at ~ 47 eV, and the Ni $M2/M3$ edge is located at ~ 67 eV. The comparison between the experimental and theoretical ground states is shown below in Figure 5.9:
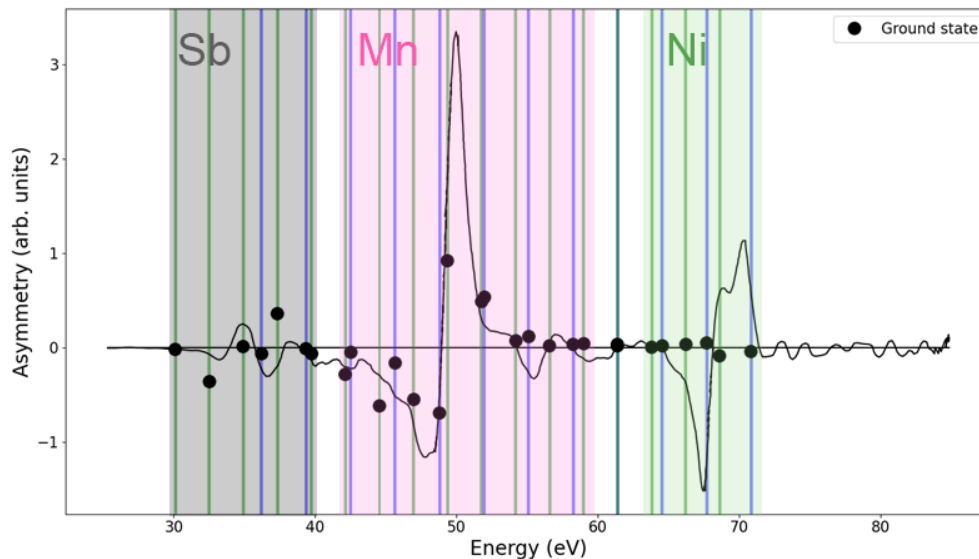
Figure 5.9: **Theoretical and measured ground state asymmetry for NiMnSb.** The solid black line shows the calculated TMOKE asymmetry for a 45° measurement of bulk NiMnSb. The blue bars show the energy bandwidth for each harmonic in the Boulder setup (40° AOI), and the green bars show the energy bandwidth for each harmonic in the Göttingen setup (45° AOI). The black dots show the measured asymmetry at a given harmonic. Both experiments measure the asymmetry of a 2 nm Ru / 13 nm NiMnSb / (In,Ga)As / InP:Fe (top to bottom) sample. The colored regions indicate which portions of the asymmetry correspond with which elements. Using harmonic combs from different sources allows us to sample the magnetic asymmetry more densely. The experimental asymmetries from each experiment have been multiplied by an arbitrary scaling factor across the entire energy range in order to find the best match with theory.

In comparing theory and experiment, we notice a few important differences. First, we notice that experimental and theoretical Mn asymmetries are in excellent agreement from 47 eV to 60 eV, but that the measurements from Boulder and Göttingen diverge from each other in the 42-47 eV range. This divergence is likely because the asymmetries are measured at two different angles (40° in Boulder, and 45° in Göttingen). Next, we notice that the sign of the Ni asymmetry is opposite what is predicted by theory, and its magnitude is ~10x smaller than predicted. The small size of the Ni asymmetry makes it a good candidate for testing the sensitivity of our beamline, as

based on the analysis in Chapter 4, measuring such a signal previously would have required months of data acquisition time. Finally, we note that the sign of the Sb asymmetry is opposite what is predicted.

The difference in sign between the theoretical prediction for the Ni asymmetry and the measured asymmetry is particularly important. The fact that this sign has flipped implies that the coupling between the Mn and Ni sublattices is *antiferromagnetic*, rather than ferromagnetic. Since the antiferromagnetic coupling is not predicted in the ground state, we verified the sample integrity in a variety of ways. A thicker sample (20 nm NiMnSb, other stack materials the same) was also measured to ensure that the asymmetry sign flip between Ni and Mn was not due to thin film effects. The samples were measured with SQUID magnetometry to ensure their magnetic moment is consistent with theoretical predictions. We are in the process of calculating thin film interference effects of the Ru capping layer, but preliminary calculations suggest this capping layer is not responsible for reversing the sign of the Ni asymmetry. Although the experimental measurements of the Boulder and Göttingen setups are in agreement, they contradict the ferromagnetic coupling between the Ni and Mn measured by neutron diffraction in [117]. The source of this discrepancy has not yet been determined.

Since the experimental and theoretical ground states are so different, a comparison of the theoretical and experimental excited state dynamics is not meaningful. The theoretical ground state asymmetry must be corrected to make such a comparison useful, but unfortunately, the mechanism through which this theoretical ground state asymmetry might be corrected is not forthcoming.

Nevertheless, experiment need not wait for theory. We can measure the excited state dynamics of this sample without calculating anything. We pump the sample with 1.58 eV photon energy at multiple fluences and measure the asymmetry at multiple energies and time delays. The laser induced dynamics of three energies (two associated with Mn and one associated with Ni) are shown below in Figure 5.10:
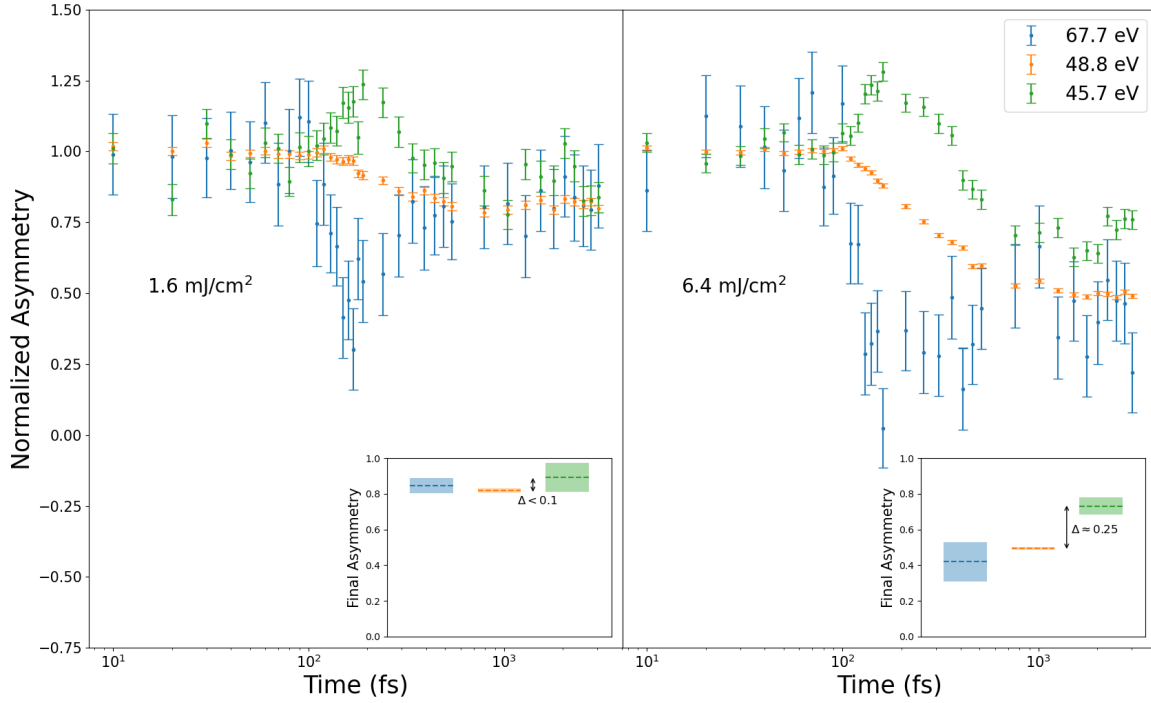
Figure 5.10: **The laser induced dynamics of the NiMnSb asymmetry with two different fluences, measured at three harmomic energies from the Boulder experiment** (described in Chapter 4). The x-axis shows logarithmic time, and $t_0 = 100$ fs. The 67.7 eV harmonic is associated with Ni, and the 48.8 and 45.7 eV harmonics are associated with Mn. The inset shows the average value of the asymmetry from 2 ps to 3 ps (dashed line), along with the standard deviation of that value (colored box). The two headed arrow indicates the difference in the "final" asymmetry value between the two harmonics associated with Mn.

The magnetization dynamics of NiMnSb are shown in Figure 5.10. First, we note the rapid increase in asymmetry of the 45.7 eV harmonic and a rapid decrease in the asymmetry of the 67.7 eV harmonic. This may be a result of pumping minority spins from Mn (associated with 45.7 eV) to Ni (associated with 67.7 eV). The potential magnetization transfer from Ni to Mn is opposite of the theoretical predictions in [83]. Interestingly, in the low fluence regime, the 67.7 eV harmonic recovers very quickly to an equilibrium value, consistent with the maximum demagnetization of the Mn harmonics. This equilibrium value is reached when the electronic and spin degrees of freedom

attain equilibrium with each other. We also note that there is approximately a 100 fs delay before the 48.8 eV harmonic begins to demagnetize.

In the high fluence regime, the 45.7 eV and 48.8 eV harmonics reach different equilibrium values. This likely occurs because the band structure of the sample is changing. When the sample is pumped at high fluence, it should demagnetize and pass through a phase transition [80, 61]. When a metallic ferromagnet is heated beyond its Curie temperature, the exchange splitting described by the Stoner model (Chapter 2.2.2) will collapse. This collapsing exchange splitting causes the harmonics to probe different energies, meaning that the measured asymmetries no longer equilibrate to their unpumped value, since the entire band structure is changing and no longer reflected by the pre-t_0 normalization.

5.3   Co$_2$MnGa

Co$_2$MnGa is a full-Heusler with 28 valence electrons, L2$_1$ crystal structure, a saturation magnetic moment of $4.05\mu_B$ per unit formula, and a Curie temperature of $T_c = 694$ K [120]. Much of the interest in this material comes from the fact that it is a magnetic Weyl semimetal [121]. Ultrafast excitations of magnetic Weyl semimetals are almost entirely unexplored [122]. In this section, I will discuss the structure and properties of Co$_2$MnGa, previous ultrafast measurements of Co$_2$MnGa, and our own measurements of Co$_2$MnGa using the setup described in Chapter 4.

Co (μ_B)	Mn (μ_B)	Ga (μ_B)	Temperature	Theory / Experiment	Reference
0.688	2.775	-0.093	0 K	Theory	[123]
0.52 ± 0.08	3.01 ± 0.16	-	4.2 K	Experiment	[120]

Table 5.2: **Atomic magnetic moments of Co$_2$MnGa.**

The magnetic moments of Co, Mn, and Ga as measured or calculated are shown above in Table 2.2. Our sample is a 20 nm thick Co$_2$MnGa sample grown with Magnetron sputtering, as described in [124]. This sample has a 3 nm SiO$_2$ capping layer and a MgO (001) substrate,

and has a tetragonal strain induced distortion because of its form factor. Its lattice constants were measured to be $a = 5.804$ Å in the film plane and $c = 5.740$ Å perpendicular to the film plane [124]. Using DFT, Galakis *et al.* calculate the element resolved density of states for bulk Co_2MnGa [123]. Mohamed Elhanoty at the University of Uppsala calculated the element resolved density of states for us based on the lattice constants for a 20 nm thin film, as shown in 5.11. This density of states shows that the Fermi energy lies between Co and Mn d-states, meaning that we may expect OISTR between these two elemental sublattices.
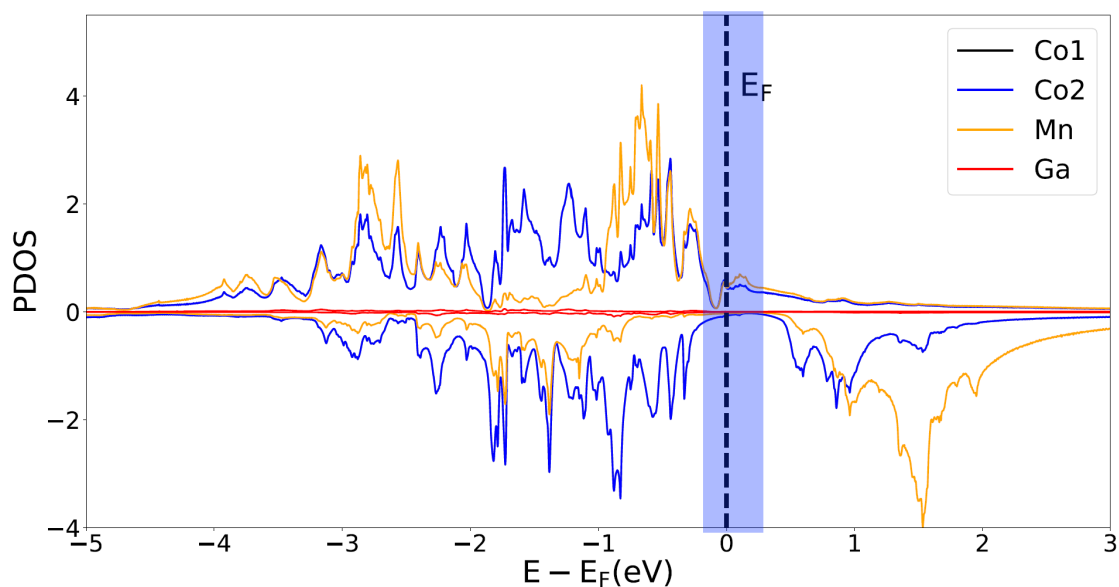
Figure 5.11: **The element resolved (partial) DOS for Co_2MnGa.** A gap is apparent in the minority spin states at the Fermi energy, and a high degree of spin polarization is observed. The band structure for each of two Co atoms per unit formula is calculated separately, and they are identical. The Fermi energy is indicated by E_F, and the blue band shows where partial occupation occurs around the Fermi energy. Calculations performed by Mohamed Elhanoty at the University of Uppsala.

While the Fermi energy lies between Co and Mn d-states, it is important to note that there is a large Co DOS at 1 eV above the Fermi energy, where the Mn DOS is relatively small. This implies that, with a 1.6 eV pump photon energy, Co $\rightarrow$ Co transitions will also be important in

this material. There are three possible transitions:

- Transitions from occupied states below the Fermi energy to occupied states above the Fermi energy *within a single element* for the same spin channel.

- Transitions from occupied states below the Fermi energy to occupied states above the Fermi energy *between elements* for the same spin channel, given that their orbitals overlap.

- Spin flips mediated by spin-orbit coupling.

5.3.1   Previous ultrafast measurements of Co$_2$MnGa

To my knowledge, the only previous ultrafast measurements of Co$_2$MnGa were performed at the FEMTOSPEX femtoslicing facility [125] at BESSY II by Serej Solopow [126]. Their sample is a 100 nm Co$_2$MnGa thin film grown by magnetron sputtering on a MgO (001) substrate. After sputtering, the sample is annealed at 500 °C to form the L2$_1$ phase. The sample is capped with a 3 nm Al capping layer, which oxidizes to Al$_2$O$_3$.

To study the temporal dynamics of this system, Solopow uses 50 fs, 1 eV, 2.1 mJ/cm^2 pulses from a Ti:Sapphire OPA as a pump to excite the system. They use a $\sim$ 100 fs, soft x-ray probe that is tunable across multiple elemental L-edge transitions for a probe. This x-ray probe is generated with a femtoslicing technique, whereby an electron bunch in the storage ring is modulated by a sub-50 fs laser pulse. The laser pulse is temporally much shorter than the electron bunch, and so only a portion of the bunch is modulated. The modulation gives that portion of the electron bunch a different energy than the rest of the bunch, making it possible to separate out the modulated electrons. Solopow uses reflection mode x-ray absorption spectroscopy (XAS) to determine charge dynamics, and reflection mode x-ray magnetic circular dichroism (XMCD) to measure spin dynamics, as shown below in Figures 5.12 and 5.13:
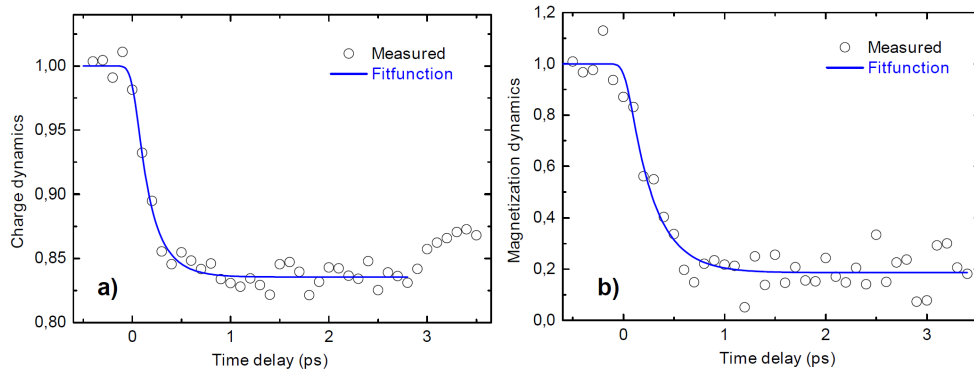
Figure 5.12: **(a) Charge and (b) spin dynamics of Co at the L-edge in Co$_2$MnGa after excitation by a 1 eV pump pulse, measured by a femtoslicing x-ray probe.** Figure adapted from [126, Chapter 5.2].

Figure 5.13: **(a) Charge and (b) spin dynamics of Mn at the L-edge in Co$_2$MnGa after excitation by a 1 eV pump pulse, measured by a femtoslicing x-ray probe.** Figure adapted from [126, Chapter 5.2].

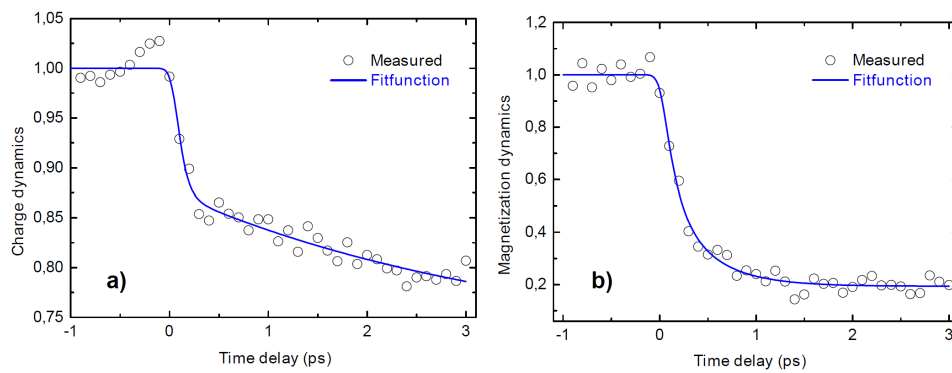Solopow does not observe any spin transfer between elemental sublattices, though there is a suggestive bump in the XMCD signal of Co near t_0, but the data is too noisy to draw any substantive conclusions about OISTR processes between elements in this material.

5.3.2   Theoretical predictions and EUV TMOKE measurements of Co$_2$MnGa

Since our beamline is designed to operate at the shot noise limit, we may be able to obtain a sufficiently high SNR to determine if OISTR processes between elements are happening in Co$_2$MnGa. Theoretically, OISTR is predicted to occur between Mn and Co, with minority spins being pumped from Co to Mn, increasing the total Co moment by nearly 10% of its initial moment and reducing the Mn moment by nearly 20%. The theoretically predicted magnetization dynamics of Co and Mn are shown below in Figure 5.14:
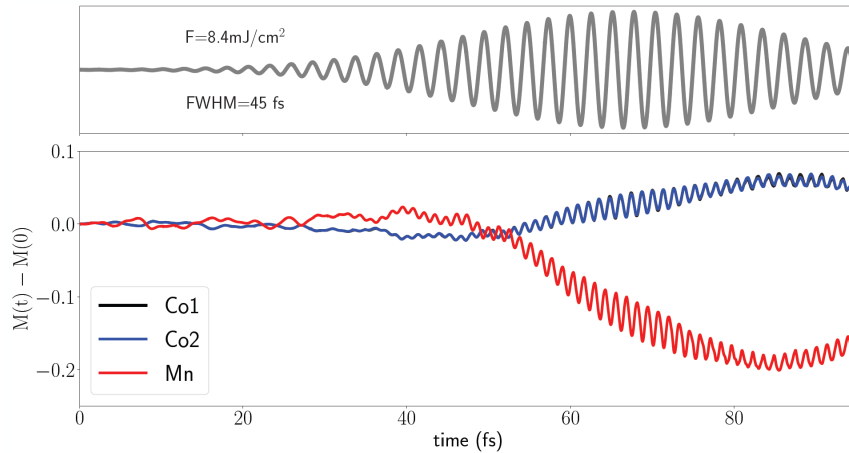
Figure 5.14: **Co$_2$MnGa theoretical magnetization dynamics during excitation with a 1.6 eV laser pulse.** The top figure shows an incident laser pulse with 1.6 eV photon energy and a fluence of 8.4 mJ/cm^2. The bottom figure shows the magnetization dynamics of different elements in Co$_2$MnGa based on the Kohn-Sham Hamiltonian using TD-DFT. The y-axis is in units of μ_B. The two cobalt atoms per unit formula are treated independently, but are shown to follow the same dynamics. These calculations were performed by Mohamed Elhanoty at the University of Uppsala.

Here we see a clear increase in the magnetization of Co, which we expect based on our heuristic rule that the Fermi energy lies between the Mn and Co d-states. If we choose a specific time, e.g. the peak electric field of the laser pulse, we can examine how the occupation of different elements has changed at different energies, as shown below in Figure 5.15:
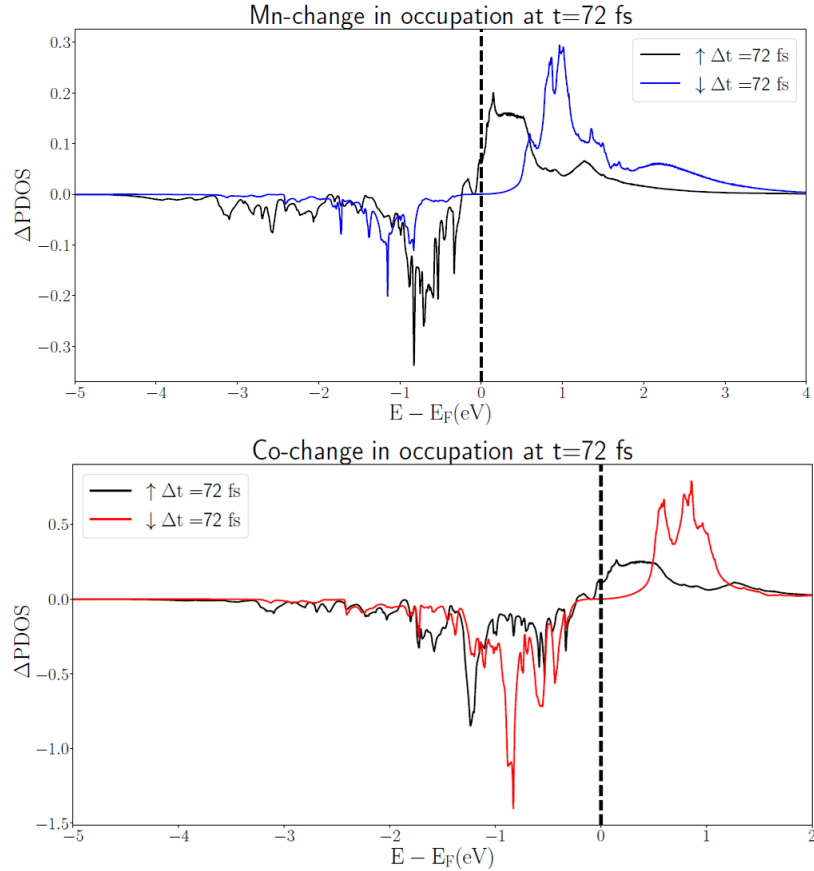
Figure 5.15: **Theoretical change in occupation for Mn and Co sublattices in Co$_2$MnGa.** The change in occupation is plotted relative to the ground state Fermi energy. The time is chosen to be 72 fs because that is the arrival time of the peak electric field intensity, as shown in Figure 5.14. These changes in occupation take into account all three possible excitation channels. The change in magnetization of a given element can be determined by summing the entire change in the partial density of states (PDOS) of both spin channels from -5 eV to 5 eV. Note that these plots have very different y-axis scalings. These calculations were performed by Mohamed Elhanoty at the University of Uppsala.

Relative to the Fermi energy, we see especially large depletions of the minority state in Co near -0.8 eV, and a large increase in the minority state near 1 eV. For Mn, we instead see a large depletion of the majority state at -0.8 eV, and a large increase in the minority state at 1 eV. Qualitatively, the integrated area of the Mn minority state peak at 1 eV is much larger than the

integrated aread of the Mn minority state trough at -1.2 eV. These extra minority state electrons must, therefore, come from Co.

Experimentally, we pump the sample using a 45 fs pulse with 1.6 eV photon energy and 3.2 mJ / cm^2 fluence incident fluence. (The discrepancy between this fluence and the fluence used in theory is due to a mirror coating that caused us to misestimate our actual fluence. We plan to re-do the theory calculations.) We probe the sample with multiple energies, measuring both the transient reflectivity and time-resolved TMOKE. A few of the selected energies are shown in Figure 5.16 below:
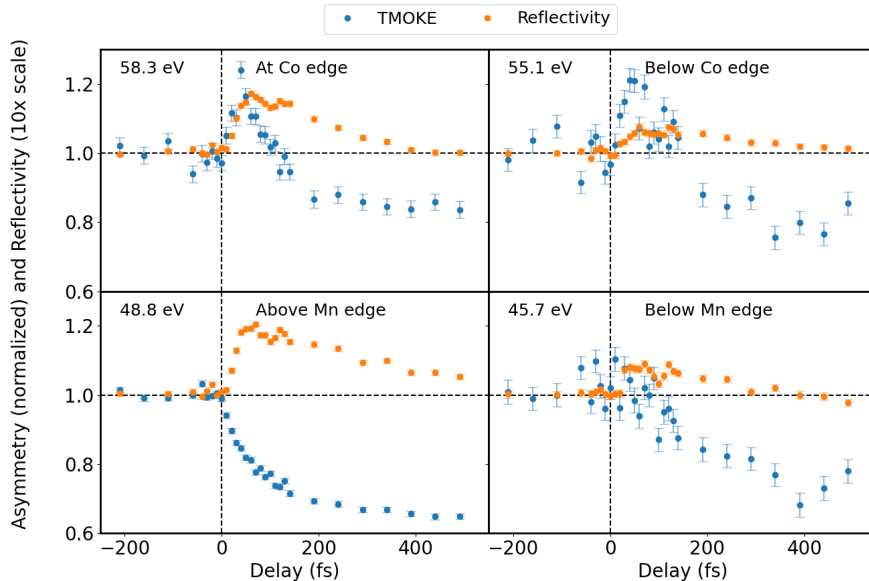
Figure 5.16: **Experimental laser induced dynamics of Co$_2$MnGa with a 1.6 eV, 3.2 mJ pump at and below the Co edge (58.9 eV), and above and below the Mn edge (47.2 eV).** The TMOKE signal at and below the Co edge peaks at $\sim$ 40 fs, whereas the reflectivity peaks at $\sim$ 60 fs, indicating a lag between the spin dynamics and total charge dynamics. The Mn TMOKE signal above the Fermi energy decays rapidly without any increase, and the Mn TMOKE below the Fermi energy, though noisier, also decays after excitation. Interestingly, a second reflectivity peak at $\sim$ 120 fs is present at all energies.

Here, we observe an increase in the Co TMOKE signal that is $\sim 3x$ larger than the increase in the Co TMOKE signal for Co_2MnGe [25]. The Mn TMOKE signal, by contrast, decays quickly. This data is consistent with the interpretation that we can transfer Co minority spins to Mn, increasing the magnetization of the Co and decreasing the magnetization of the Mn. The time delay between the Co TMOKE peak and the Co reflectivity peak is evidence that the initial excitation of electrons is highly spin dependent (which is expected because dipole transitions do not flip the spin state). The origin of the second reflectivity peak near 120 fs is unclear and it is currently the subject of theoretical investigation.

Chapter 6

Conclusions and future directions

We have demonstrated the performance of a new beamline called X-MATTER (**X**UV **M**agnetic **A**symmetry with **T**abletop **T**emporal and **E**lemental **R**esolution) for measuring element-resolved dynamics of magnetic thin films in reflection-mode near the shot noise limit. We present measurements showing a noise floor within 5% of the shot noise limit for a single harmonic, and we show how the low measurement noise improves the SNR of fluence dependent magnetic dynamics, excited electron dynamics, acoustic wave detection, and the ultrafast transfer of spin polarization between different elemental sublattices in a magnetic alloy. This new beamline already offers more than an order of magnitude improvement over the noise performance of the previous beamline, enabling us to study previously inaccessible phenomena.

Further optimization of the laser and HHG source by increasing the repetition rate and flux, as well as enhanced instrument control and optimization of the data acquisition approach, can improve our data acquisition rate by ∼10-100x. Specifically, the EUV flux can be enhanced by increasing the repetition rate of the laser driver by ∼10x or more (e.g. from 5 to 50 kHz), by optimizing the reflectivity of the EUV focusing optics and gratings, and by optimizing the geometry of the HHG source.

We also note that our measurements and analyses are performed using Ne as the gas medium, which can span a photon energy range of 40-72 eV simultaneously, using 780 nm driving lasers. By shifting to longer wavelength driving lasers (> 1 μm) [53], further increases in the HHG flux would be possible, since the same photon energy range can be reached by phase matching the

HHG process in Ar gas, which exhibits less residual absorption of the EUV beam.

We used the X-MATTER beamline to study the ultrafast magnetic dynamics of NiMnSb and Co_2MnGa. The Ni moment of NiMnSb is much smaller than theoretically predicted (experimentally, the asymmetry is $\sim 0.5\%$), and so our measurement of its temporal evolution is an excellent demonstration of the capabilities of this beamline. We are currently working to understand why the coupling between the Ni and Mn sublattices are measured to be opposite to what is theoretically predicted. Nevertheless, NiMnSb still shows evidence of OISTR between Mn and Ni (even though it is not in the expected direction) and it shows evidence of exchange collapse after intense pumping. In Co_2MnGa, we notice a pronounced increase in the Co TMOKE asymmetry after laser excitation, indicative of a minority spin transfer from Co to Mn. We also observe the presence of a time delay between the peak of the TMOKE signal and the peak of the reflectivity signal, which seems to indicate that the excitation of one spin channel proceeds faster than the excitation of the other spin channel and may be further evidence of an OISTR type mechanism.

The ability to make low-noise, element-resolved measurements of ultrafast magnetic, electronic, and acoustic excitations unlocks the possibility to explore the fundamental interactions in magnetic thin films on their natural timescales. This setup enables a shot noise limited approach to studying magnetic dynamics that can be further improved with increases to photon flux and throughput. The high SNR of this new instrument has enabled us to study the spin dynamics of multi-element magnetic compounds across their entire band structure, an important advance that is yielding new insight into light matter interactions in magnetic materials.

Bibliography

[1] Christoph Sander. "Magnets and garlic: an enduring antipathy in early-modern science". In: **Intellectual History Review** 30.4 (2020), pp. 523–560. DOI: 10.1080/17496977. 2019.1648924. eprint: https://doi.org/10.1080/17496977.2019.1648924. URL: https: //doi.org/10.1080/17496977.2019.1648924.

[2] P. Kusch and H. M. Foley. "The Magnetic Moment of the Electron". In: **Phys. Rev.** 74 (3 Aug. 1948), pp. 250–263. DOI: 10.1103/PhysRev.74.250. URL: https://link.aps.org/ doi/10.1103/PhysRev.74.250.

[3] Alberto Moscatelli. "Deviations from 2". In: **Nature Phys.** 518 (13 May 2017). DOI: https: //doi.org/10.1038/nphys4126.

[4] David J. Griffiths. **Introduction to quantum mechanics.** Upper Saddle River, NJ: Pearson Prentice Hall, 2005. ISBN: 978-0-131-11892-8.

[5] Joachim Stöhr and Hans Christoph Siegmann. **Magnetism: From Fundamentals to Nanoscale Dynamics**. Vol. 5. Springer, 2006.

[6] Vadym Zayets. **Exchange Interaction**. 2022. URL: https://staff.aist.go.jp/v. zayets/spin3_47_exchange.html.

[7] O Gunnarsson. "Band model for magnetism of transition metals in the spin-density-functional formalism". In: **Journal of Physics F: Metal Physics** 6.4 (Apr. 1976), pp. 587–606. DOI: 10.1088/0305-4608/6/4/018. URL: https://doi.org/10.1088/0305-4608/6/4/018.

[8] E. Beaurepaire et al. "Ultrafast Spin Dynamics in Ferromagnetic Nickel". In: **Phys. Rev. Lett.** 76 (22 May 1996), pp. 4250–4253. DOI: 10.1103/PhysRevLett.76.4250. URL: https://link.aps.org/doi/10.1103/PhysRevLett.76.4250.

[9] MB Agranat et al. "Interaction of picosecond laser pulses with the electron, spin, and phonon subsystems of nickel". In: **Zh. Eksp. Teor. Fiz** 86.1376 (1984), p. 10.

[10] A Vaterlaus et al. "Different spin and lattice temperatures observed by spin-polarized photoemission with picosecond laser pulses". In: **Journal of applied physics** 67.9 (1990), pp. 5661–5663.

[11] A. Vaterlaus, T. Beutler, and F. Meier. "Spin-lattice relaxation time of ferromagnetic gadolinium determined with time-resolved spin-polarized photoemission". In: **Phys. Rev. Lett.** 67 (23 Dec. 1991), pp. 3314–3317. DOI: 10.1103/PhysRevLett.67.3314. URL: https://link.aps.org/doi/10.1103/PhysRevLett.67.3314.

[12] A. Vaterlaus et al. "Spin-lattice relaxation in ferromagnets studied by time-resolved spin-polarized photoemission". In: **Phys. Rev. B** 46 (9 Sept. 1992), pp. 5280–5286. DOI: 10.1103/PhysRevB.46.5280. URL: https://link.aps.org/doi/10.1103/PhysRevB.46.5280.

[13] R. J. Elliott. "Theory of the Effect of Spin-Orbit Coupling on Magnetic Resonance in Some Semiconductors". In: **Phys. Rev.** 96 (2 Oct. 1954), pp. 266–279. DOI: 10.1103/PhysRev.96.266. URL: https://link.aps.org/doi/10.1103/PhysRev.96.266.

[14] Y. Yafet. "Conduction electron spin relaxation in the superconducting state". In: **Physics Letters A** 98.5 (1983), pp. 287–290. ISSN: 0375-9601. DOI: https://doi.org/10.1016/0375-9601(83)90874-5. URL: https://www.sciencedirect.com/science/article/pii/0375960183908745.

[15] Régis Decker et al. "Measuring the atomic spin-flip scattering rate by x-ray emission spectroscopy". In: **Scientific Reports** 9 (June 2019). ISSN: 2045-2322. DOI: 10.1038/s41598-019-45242-8. URL: https://doi.org/10.1038/s41598-019-45242-8.

[16] Michael Krauß et al. "Ultrafast demagnetization of ferromagnetic transition metals: The role of the Coulomb interaction". In: **Phys. Rev. B** 80 (18 Nov. 2009), p. 180407. DOI: 10.1103/PhysRevB.80.180407. URL: https://link.aps.org/doi/10.1103/PhysRevB.80.180407.

[17] C Stamm et al. "Femtosecond modification of electron localization and transfer of angular momentum in nickel". In: **Nature materials** 6.10 (2007), pp. 740–743.

[18] A Goris et al. "Role of spin-flip exchange scattering for hot-electron lifetimes in cobalt". In: **Physical review letters** 107.2 (2011), p. 026601.

[19] M Aeschlimann et al. "Ultrafast spin-dependent electron dynamics in fcc Co". In: **Physical review letters** 79.25 (1997), p. 5158.

[20] Sebastiaan van Dijken, Xin Jiang, and Stuart S. P. Parkin. "Spin-dependent hot electron transport in $Ni_{81}Fe_{19}$ and $Co_{84}Fe_{16}$ films on GaAs(001)". In: **Phys. Rev. B** 66 (9 Sept. 2002), p. 094417. DOI: 10.1103/PhysRevB.66.094417. URL: https://link.aps.org/doi/10.1103/PhysRevB.66.094417.

[21] M. Battiato, K. Carva, and P. M. Oppeneer. "Superdiffusive Spin Transport as a Mechanism of Ultrafast Demagnetization". In: **Phys. Rev. Lett.** 105 (2 July 2010), p. 027203. DOI: 10.1103/PhysRevLett.105.027203. URL: https://link.aps.org/doi/10.1103/PhysRevLett.105.027203.

[22] Dennis Rudolf et al. "Ultrafast magnetization enhancement in metallic multilayers driven by superdiffusive spin current". In: **Nature Communications** 3 (1 Sept. 2012). DOI: 10.1038/ncomms2029.

[23] Emrah Turgut et al. "Controlling the Competition between Optically Induced Ultrafast Spin-Flip Scattering and Spin Transport in Magnetic Multilayers". In: **Phys. Rev. Lett.** 110 (19 May 2013), p. 197201. DOI: 10.1103/PhysRevLett.110.197201. URL: https://link.aps.org/doi/10.1103/PhysRevLett.110.197201.

[24] P Elliott et al. "Ultrafast laser induced local magnetization dynamics in Heusler compounds". In: **Scientific Reports** 6.1 (2016), pp. 1–9.

[25] Phoebe Tengdin et al. "Direct light–induced spin transfer between different elements in a spintronic Heusler material via femtosecond laser excitation". In: **Science Advances** 6.3 (2020), eaaz1100. DOI: `10.1126/sciadv.aaz1100`. eprint: `https://www.science.org/doi/pdf/10.1126/sciadv.aaz1100`. URL: `https://www.science.org/doi/abs/10.1126/sciadv.aaz1100`.

[26] Ml Freiser. "A survey of magnetooptic effects". In: **IEEE Transactions on magnetics** 4.2 (1968), pp. 152–161.

[27] ZJ Yang and MR Scheinfein. "Combined three-axis surface magneto-optical Kerr effects in the study of surface and ultrathin-film magnetism". In: **Journal of applied physics** 74.11 (1993), pp. 6810–6823.

[28] Peter M. Oppeneer. **Handbook of magnetic materials, Chapter 3: Magneto-optical Kerr spectra**. Ed. by KH Jürgen Buschow. Elsevier, 2003.

[29] J. L. Erskine and E. A. Stern. "Calculation of the M_{23} magneto-optical absorption spectrum of ferromagnetic nickel". In: **Phys. Rev. B** 12 (11 Dec. 1975), pp. 5016–5024. DOI: `10.1103/PhysRevB.12.5016`. URL: `https://link.aps.org/doi/10.1103/PhysRevB.12.5016`.

[30] J. Stöhr and Y. Wu. "X-Ray Magnetic Circular Dichroism: Basic Concepts and Theory for 3D Transition Metal Atoms". In: **New Directions in Research with Third-Generation Soft X-Ray Synchrotron Radiation Sources**. Ed. by A. S. Schlachter and F. J. Wuilleumier. Dordrecht: Springer Netherlands, 1994, pp. 221–250. ISBN: 978-94-011-0868-3. DOI: `10.1007/978-94-011-0868-3_9`. URL: `https://doi.org/10.1007/978-94-011-0868-3_9`.

[31] M.-C. Chen et al. "Bright, Coherent, Ultrafast Soft X-Ray Harmonics Spanning the Water Window from a Tabletop Light Source". In: **Phys. Rev. Lett.** 105 (17 Oct. 2010), p. 173901.

DOI: 10.1103/PhysRevLett.105.173901. URL: https://link.aps.org/doi/10.1103/PhysRevLett.105.173901.

[32] Tenio Popmintchev et al. "Bright Coherent Ultrahigh Harmonics in the keV X-ray Regime from Mid-Infrared Femtosecond Lasers". In: **Science** 336.6086 (2012), pp. 1287–1291. DOI: 10.1126/science.1218497. URL: https://www.science.org/doi/abs/10.1126/science.1218497.

[33] Kyung-Han Hong et al. "Multi-mJ, kHz, 2.1μm optical parametric chirped-pulse amplifier and high-flux soft x-ray high-harmonic generation". In: **Opt. Lett.** 39.11 (June 2014), pp. 3145–3148. DOI: 10.1364/OL.39.003145. URL: http://opg.optica.org/ol/abstract.cfm?URI=ol-39-11-3145.

[34] Tingting Fan et al. "Bright circularly polarized soft X-ray high harmonics for X-ray magnetic circular dichroism". In: **Proceedings of the National Academy of Sciences** 112.46 (2015), pp. 14206–14211. DOI: 10.1073/pnas.1519666112. URL: https://www.pnas.org/doi/abs/10.1073/pnas.1519666112.

[35] Hans A. Bethe and Edwin E. Salpeter. **Quantum Mechanics of One- and Two-Electron Atoms**. Springer New York, NY, 1986. ISBN: 978-0-306-20022-9. DOI: https://doi.org/10.1007/978-1-4613-4104-8. URL: https://link.springer.com/book/10.1007/978-1-4613-4104-8.

[36] Thomas Tietze. "Magnetism of unconventional nanoscaled materials: an X-ray circular dichroism and muon spin rotation study". PhD thesis. 2014.

[37] J Zak et al. "Magneto-optics of multilayers with arbitrary magnetization directions". In: **Physical Review B** 43.8 (1991), p. 6423.

[38] Milan Milosevic. "On the nature of the evanescent wave". In: **Applied spectroscopy** 67.2 (2013), pp. 126–131.

[39] Peter C. Johnsen et al. "An extreme ultraviolet beamline for ultrafast magneto-optical spectroscopy near the shot noise limit". In: **Review of Scientific Instruments** (Submitted for review 2022).

[40] Burton L Henke, Eric M Gullikson, and John C Davis. "X-ray interactions: photoabsorption, scattering, transmission, and reflection at E= 50-30,000 eV, Z= 1-92". In: **Atomic data and nuclear data tables** 54.2 (1993), pp. 181–342.

[41] Christopher A. Mancuso et al. "Strong-field ionization with two-color circularly polarized laser fields". In: **Phys. Rev. A** 91 (3 Mar. 2015), p. 031402. DOI: `10.1103/PhysRevA.91.031402`. URL: `https://link.aps.org/doi/10.1103/PhysRevA.91.031402`.

[42] Ofer Kfir et al. "In-line production of a bi-circular field for generation of helically polarized high-order harmonics". In: **Applied Physics Letters** 108.21 (2016), p. 211106.

[43] Katsumi Midorikawa. "Ultrafast dynamic imaging". In: **Nature Photonics** 5.11 (2011), pp. 640–641.

[44] Ivan P. Christov, Margaret M. Murnane, and Henry C. Kapteyn. "High-Harmonic Generation of Attosecond Pulses in the "Single-Cycle" Regime". In: **Phys. Rev. Lett.** 78 (7 Feb. 1997), pp. 1251–1254. DOI: `10.1103/PhysRevLett.78.1251`. URL: `https://link.aps.org/doi/10.1103/PhysRevLett.78.1251`.

[45] G. Sansone et al. "Isolated Single-Cycle Attosecond Pulses". In: **Science** 314.5798 (2006), pp. 443–446. DOI: `10.1126/science.1132838`. eprint: `https://www.science.org/doi/pdf/10.1126/science.1132838`. URL: `https://www.science.org/doi/abs/10.1126/science.1132838`.

[46] Ming-Chang Chen et al. "Generation of bright isolated attosecond soft X-ray pulses driven by multicycle midinfrared lasers". In: **Proceedings of the National Academy of Sciences** 111.23 (2014), E2361–E2367. DOI: `10.1073/pnas.1407421111`. eprint: `https://www.pnas.org/doi/pdf/10.1073/pnas.1407421111`. URL: `https://www.pnas.org/doi/abs/10.1073/pnas.1407421111`.

[47] S. Eich et al. "Time- and angle-resolved photoemission spectroscopy with optimized high-harmonic pulses using frequency-doubled Ti:Sapphire lasers". In: **Journal of Electron Spectroscopy and Related Phenomena** 195 (2014), pp. 231–236. ISSN: 0368-2048. DOI: `https://doi.org/10.1016/j.elspec.2014.04.013`. URL: `https://www.sciencedirect.com/science/article/pii/S036820481400108X`.

[48] Benjamin R Galloway. "High-Order Harmonic Generation Driven by Mid-Infrared Laser Light". PhD thesis. University of Colorado at Boulder, 2017.

[49] Jeffrey L. Krause, Kenneth J. Schafer, and Kenneth C. Kulander. "High-order harmonic generation from atoms and ions in the high intensity regime". In: **Phys. Rev. Lett.** 68 (24 June 1992), pp. 3535–3538. DOI: `10.1103/PhysRevLett.68.3535`. URL: `https://link.aps.org/doi/10.1103/PhysRevLett.68.3535`.

[50] J. Tate et al. "Scaling of Wave-Packet Dynamics in an Intense Midinfrared Field". In: **Phys. Rev. Lett.** 98 (1 Jan. 2007), p. 013901. DOI: `10.1103/PhysRevLett.98.013901`. URL: `https://link.aps.org/doi/10.1103/PhysRevLett.98.013901`.

[51] Andrew Ralph Rundquist. **Phase-matched generation of coherent, ultrafast x-rays using high harmonics**. Washington State University, 1998.

[52] Andy Rundquist et al. "Phase-Matched Generation of Coherent Soft X-rays". In: **Science** 280.5368 (1998), pp. 1412–1415. DOI: `10.1126/science.280.5368.1412`. eprint: `https://www.science.org/doi/pdf/10.1126/science.280.5368.1412`. URL: `https://www.science.org/doi/abs/10.1126/science.280.5368.1412`.

[53] Tenio Popmintchev et al. "Phase matching of high harmonic generation in the soft and hard X-ray regions of the spectrum". In: **Proceedings of the National Academy of Sciences** 106.26 (2009), pp. 10516–10521. DOI: `10.1073/pnas.0903748106`. eprint: `https://www.pnas.org/doi/pdf/10.1073/pnas.0903748106`. URL: `https://www.pnas.org/doi/abs/10.1073/pnas.0903748106`.

[54] Jennifer L Ellis. "Development and Application of Extreme Ultraviolet Light Sources–Harnessing Novel Geometries of High-Harmonic Generation and Using Photoelectron Spectroscopy to Study Nanoparticle Dynamics". PhD thesis. University of Colorado at Boulder, 2018.

[55] Avner Fleischer et al. "Spin angular momentum and tunable polarization in high-harmonic generation". In: **Nature Photonics** 8.7 (2014), pp. 543–549.

[56] Daniel D Hickstein et al. "Non-collinear generation of angularly isolated circularly polarized high harmonics". In: **Nature Photonics** 9.11 (2015), pp. 743–750.

[57] Jennifer L. Ellis et al. "High harmonics with spatially varying ellipticity". In: **Optica** 5.4 (Apr. 2018), pp. 479–485. DOI: `10.1364/OPTICA.5.000479`. URL: `http://opg.optica.org/optica/abstract.cfm?URI=optica-5-4-479`.

[58] Kevin M Dorney et al. "Controlling the polarization and vortex charge of attosecond high-harmonic beams via simultaneous spin–orbit momentum conservation". In: **Nature photonics** 13.2 (2019), pp. 123–130.

[59] Laura Rego et al. "Necklace-structured high-harmonic generation for low-divergence, soft x-ray harmonic combs with tunable line spacing". In: **Science Advances** 8.5 (2022), eabj7380. DOI: `10.1126/sciadv.abj7380`. eprint: `https://www.science.org/doi/pdf/10.1126/sciadv.abj7380`. URL: `https://www.science.org/doi/abs/10.1126/sciadv.abj7380`.

[60] Cong Chen et al. "Distinguishing attosecond electron–electron scattering and screening in transition metals". In: **Proceedings of the National Academy of Sciences** 114.27 (2017), E5300–E5307.

[61] Wenjing You et al. "Revealing the nature of the ultrafast magnetic phase transition in Ni by correlating extreme ultraviolet magneto-optic and photoemission spectroscopies". In: **Physical review letters** 121.7 (2018), p. 077204.

[62]   Xun Shi et al. "Ultrafast electron calorimetry uncovers a new long-lived metastable state in 1 T-TaSe2 mediated by mode-selective electron-phonon coupling". In: **Science advances** 5.3 (2019), eaav4449.

[63]   Yingchao Zhang et al. "Creation of a novel inverted charge density wave state". In: **Structural Dynamics** 9.1 (2022), p. 014501.

[64]   Bosheng Zhang et al. "High contrast 3D imaging of surfaces near the wavelength limit using tabletop EUV ptychography". In: **Ultramicroscopy** 158 (2015), pp. 98–104.

[65]   Elisabeth R Shanblatt et al. "Quantitative chemically specific coherent diffractive imaging of reactions at buried interfaces with few nanometer precision". In: **Nano letters** 16.9 (2016), pp. 5444–5450.

[66]   Robert M Karl Jr et al. "Full-field imaging of thermal and acoustic dynamics in an individual nanostructure using tabletop high harmonic beams". In: **Science advances** 4.10 (2018), eaau4295.

[67]   Nathan J Brooks et al. "Temporal and spectral multiplexing for EUV multibeam ptychography with a high harmonic light source". In: **Optics Express** 30.17 (2022), pp. 30331–30346.

[68]   Yusuke Tamaki et al. "Highly efficient, phase-matched high-harmonic generation by a self-guided laser beam". In: **Physical Review Letters** 82.7 (1999), p. 1422.

[69]   V. Tosa et al. "Generation of high-order harmonics in a self-guided beam". In: **Phys. Rev. A** 67 (6 June 2003), p. 063817. DOI: 10.1103/PhysRevA.67.063817. URL: https://link.aps.org/doi/10.1103/PhysRevA.67.063817.

[70]   J. R. Sutherland et al. "High harmonic generation in a semi-infinite gas cell". In: **Opt. Express** 12.19 (Sept. 2004), pp. 4430–4436. DOI: 10.1364/OPEX.12.004430. URL: http://opg.optica.org/oe/abstract.cfm?URI=oe-12-19-4430.

[71] Daniel S. Steingrube et al. "Phase matching of high-order harmonics in a semi-infinite gas cell". In: **Phys. Rev. A** 80 (4 Nov. 2009), p. 043819. DOI: 10.1103/PhysRevA.80.043819. URL: https://link.aps.org/doi/10.1103/PhysRevA.80.043819.

[72] D S Steingrube et al. "High-order harmonic generation directly from a filament". In: **New Journal of Physics** 13.4 (Apr. 2011), p. 043022. DOI: 10.1088/1367-2630/13/4/043022. URL: https://doi.org/10.1088/1367-2630/13/4/043022.

[73] Sophie Kazamias et al. "High order harmonic generation optimization with an apertured laser beam". In: **The European Physical Journal D-Atomic, Molecular, Optical and Plasma Physics** 21.3 (2002), pp. 353–359.

[74] O. Hassouneh et al. "Cooper minimum in singly ionized and neutral argon". In: **Phys. Rev. A** 98 (4 Oct. 2018), p. 043419. DOI: 10.1103/PhysRevA.98.043419. URL: https://link.aps.org/doi/10.1103/PhysRevA.98.043419.

[75] Hung-Wei Sun et al. "Extended phase matching of high harmonic generation by plasma-induced defocusing". In: **Optica** 4.8 (Aug. 2017), pp. 976–981. DOI: 10.1364/OPTICA.4.000976. URL: http://opg.optica.org/optica/abstract.cfm?URI=optica-4-8-976.

[76] Ganping Ju et al. "Ultrafast generation of ferromagnetic order via a laser-induced phase transformation in FeRh thin films". In: **Physical review letters** 93.19 (2004), p. 197403.

[77] AV Kimel et al. "Laser-induced ultrafast spin reorientation in the antiferromagnet TmFeO3". In: **Nature** 429.6994 (2004), pp. 850–853.

[78] AV Kimel et al. "Ultrafast non-thermal control of magnetization by instantaneous photo-magnetic pulses". In: **Nature** 435.7042 (2005), pp. 655–657.

[79] Andrei Kirilyuk, Alexey V Kimel, and Theo Rasing. "Ultrafast optical manipulation of magnetic order". In: **Reviews of Modern Physics** 82.3 (2010), p. 2731.

[80] Phoebe Tengdin et al. "Critical behavior within 20 fs drives the out-of-equilibrium laser-induced magnetic phase transition in nickel". In: **Science advances** 4.3 (2018), eaap9744.

[81]   Moritz Hofherr et al. "Ultrafast optically induced spin transfer in ferromagnetic alloys". In: **Science advances** 6.3 (2020), eaay8717.

[82]   John Kay Dewhurst et al. "Laser-induced intersite spin transfer". In: **Nano letters** 18.3 (2018), pp. 1842–1848.

[83]   Daniel Steil et al. "Efficiency of ultrafast optically induced spin transfer in Heusler compounds". In: **Phys. Rev. Research** 2 (2 May 2020), p. 023199. URL: https://link.aps.org/doi/10.1103/PhysRevResearch.2.023199.

[84]   AR Khorsand et al. "Element-specific probing of ultrafast spin dynamics in multisublattice magnets with visible light". In: **Physical review letters** 110.10 (2013), p. 107205.

[85]   Jake Sutcliffe and J Olof Johansson. "A femtosecond magnetic circular dichroism spectrometer". In: **Review of Scientific Instruments** 92.11 (2021), p. 113001.

[86]   La-O Chan et al. "Ultrafast demagnetization dynamics at the M edges of magnetic elements observed using a tabletop high-harmonic soft x-ray source". In: **Physical Review Letters** 103.25 (2009), p. 257402.

[87]   Chan La-O-Vorakiat et al. "Ultrafast demagnetization measurements using extreme ultraviolet light: Comparison of electronic and magnetic contributions". In: **Physical Review X** 2.1 (2012), p. 011005.

[88]   Christina Möller et al. "Ultrafast element-resolved magneto-optics using a fiber-laser-driven extreme ultraviolet light source". In: **Review of Scientific Instruments** 92.6 (2021), p. 065107.

[89]   Martin Hennecke et al. "Ultrafast element- and depth-resolved magnetization dynamics probed by transverse magneto-optical Kerr effect spectroscopy in the soft x-ray range". In: **Phys. Rev. Research** 4 (2 June 2022), p. L022062. DOI: 10.1103/PhysRevResearch.4.L022062. URL: https://link.aps.org/doi/10.1103/PhysRevResearch.4.L022062.

[90] Filippo Bencivenga et al. "Nanoscale transient gratings excited and probed by extreme ultraviolet femtosecond pulses". In: **Science advances** 5.7 (2019), eaaw5805.

[91] Albert Beardo et al. "A General and Predictive Understanding of Thermal Transport from 1D-and 2D-Confined Nanostructures: Theory and Experiment". In: **ACS nano** 15.8 (2021), pp. 13019–13030.

[92] Kelvin Yao et al. "A tabletop setup for ultrafast helicity-dependent and element-specific absorption spectroscopy and scattering in the extreme ultraviolet spectral range". In: **Review of Scientific Instruments** 91.9 (2020), p. 093001.

[93] Clemens von Korff Schmising et al. "Element-specific magnetization dynamics of complex magnetic systems probed by ultrafast magneto-optical spectroscopy". In: **Applied Sciences** 10.21 (2020), p. 7580.

[94] Kathleen M Hoogeboom-Pot et al. "Nondestructive measurement of the evolution of layer-specific mechanical properties in sub-10 nm bilayer films". In: **Nano Letters** 16.8 (2016), pp. 4773–4778.

[95] Philip CD Hobbs. **Building electro-optical systems: making it all work**. John Wiley & Sons, 2022.

[96] Travis D Frazer et al. "Full characterization of ultrathin 5-nm low-k dielectric bilayers: Influence of dopants and surfaces on the mechanical properties". In: **Physical Review Materials** 4.7 (2020), p. 073603.

[97] Albert Beardo et al. "Thermal transport from 1D-and 2D-confined nanostructures on silicon probed using coherent extreme UV light: General and predictive model yields new understanding". In: **arXiv preprint arXiv:2103.03776** (2021).

[98] Michael Tanksalvala et al. "Nondestructive, high-resolution, chemically specific 3D nanostructure characterization using phase-sensitive EUV imaging reflectometry". In: **Science Advances** 7.5 (2021), eabd9667.

[99]   David R Lide. **CRC handbook of chemistry and physics**. Vol. 85. CRC press, 2004.

[100]   RJ Bruls et al. "The temperature dependence of the Young's modulus of MgSiN2, AlN and Si3N4". In: **Journal of the European Ceramic Society** 21.3 (2001), pp. 263–268.

[101]   Thorsten Krenke et al. "Inverse magnetocaloric effect in ferromagnetic Ni–Mn–Sn alloys". In: **Nature materials** 4.6 (2005), pp. 450–454.

[102]   Tomasz Klimczuk et al. "Superconductivity in the Heusler family of intermetallics". In: **Physical Review B** 85.17 (2012), p. 174505.

[103]   I Galanakis, Ph Mavropoulos, and Ph H Dederichs. "Electronic structure and Slater–Pauling behaviour in half-metallic Heusler alloys calculated from first principles". In: **Journal of Physics D: Applied Physics** 39.5 (2006), p. 765.

[104]   I Galanakis and Ph Mavropoulos. "Spin-polarization and electronic properties of half-metallic Heusler alloys calculated from first principles". In: **Journal of Physics: Condensed Matter** 19.31 (2007), p. 315213.

[105]   F Casper et al. "Half-Heusler compounds: novel materials for energy and spintronic applications". In: **Semiconductor Science and Technology** 27.6 (2012), p. 063001.

[106]   Stanislav Chadov et al. "Tunable multifunctional topological insulators in ternary Heusler compounds". In: **Nature materials** 9.7 (2010), pp. 541–545.

[107]   Hsin Lin et al. "Half-Heusler ternary compounds as new multifunctional experimental platforms for topological quantum phenomena". In: **Nature materials** 9.7 (2010), pp. 546–549.

[108]   Tanja Graf, Claudia Felser, and Stuart SP Parkin. "Simple rules for the understanding of Heusler compounds". In: **Progress in solid state chemistry** 39.1 (2011), pp. 1–50.

[109]   Hans Nowotny and Wilhelm Sibert. "Ternäre Valenzverbindungen in den Systemen Kupfer (Silber)-Arsen (Antimon, Wismut)-Magnesium". In: **International Journal of Materials Research** 33.12 (1941), pp. 391–394.

[110] Robert Juza and Franz Hund. "Die Kristallstrukturen LiMgN, LiznN, Li3AIN2 und Li3GaN2". In: **Die Naturwissenschaften** 33.4 (1946), pp. 121–122.

[111] Robert Juza and Franz Hund. "Die ternären Nitride LiMgN und LiZnN. 16. Mitteilung über Metallamide und Metallnitride". In: **Zeitschrift für anorganische Chemie** 257.1-3 (1948), pp. 1–12.

[112] D Jung, H-J Koo, and M-H Whangbo. "Study of the 18-electron band gap and ferromagnetism in semi-Heusler compounds by non-spin-polarized electronic band structure calculations". In: **Journal of Molecular Structure: THEOCHEM** 527.1-3 (2000), pp. 113–119.

[113] M. Le žai ć et al. "Thermal Collapse of Spin Polarization in Half-Metallic Ferromagnets". In: **Phys. Rev. Lett.** 97 (2 July 2006), p. 026404. DOI: `10.1103/PhysRevLett.97.026404`. URL: `https://link.aps.org/doi/10.1103/PhysRevLett.97.026404`.

[114] L. M. Sandratskii. "Thermal magnetic properties of the Ni sublattice in half-metallic NiMnSb: A theoretical study based on first-principles calculations". In: **Phys. Rev. B** 78 (9 Sept. 2008), p. 094425. DOI: `10.1103/PhysRevB.78.094425`. URL: `https://link.aps.org/doi/10.1103/PhysRevB.78.094425`.

[115] PJ Webster and RM Mankikar. "Chemical order and magnetic properties of the Ni2- xMnSb system". In: **Journal of magnetism and magnetic materials** 42.3 (1984), pp. 300–308.

[116] T. Block et al. "Band-structure calculations of the half-metallic ferromagnetism and structural stability of full- and half-Heusler phases". In: **Phys. Rev. B** 70 (20 Nov. 2004), p. 205114. DOI: `10.1103/PhysRevB.70.205114`. URL: `https://link.aps.org/doi/10.1103/PhysRevB.70.205114`.

[117] Ch Hordequin, E Lelievre-Berna, and J Pierre. "Magnetization density in the half-metallic ferromagnet NiMnSb". In: **Physica B: Condensed Matter** 234 (1997), pp. 602–604.

[118] C. N. Borca et al. "Evidence for temperature dependent moments ordering in ferromagnetic NiMnSb(100)". In: **Phys. Rev. B** 64 (5 July 2001), p. 052409. DOI: `10.1103/PhysRevB.64.052409`. URL: `https://link.aps.org/doi/10.1103/PhysRevB.64.052409`.

[119] Dmitriy Zusin. "Ultrafast dynamics of Magnetic multilayer films: magneto-optical spectroscopy and resonant scattering in the extreme ultraviolet and soft X-ray spectral regions". PhD thesis. University of Colorado at Boulder, 2018.

[120] PJ Webster. "Magnetic and chemical order in Heusler alloys containing cobalt and manganese". In: **Journal of Physics and Chemistry of Solids** 32.6 (1971), pp. 1221–1231.

[121] Binghai Yan and Claudia Felser. "Topological materials: Weyl semimetals". In: **Annual Review of Condensed Matter Physics** 8 (2017), pp. 337–354.

[122] Chris P Weber. "Ultrafast investigation and control of Dirac and Weyl semimetals". In: **Journal of Applied Physics** 129.7 (2021), p. 070901.

[123] I. Galanakis, P. H. Dederichs, and N. Papanikolaou. "Slater-Pauling behavior and origin of the half-metallicity of the full-Heusler alloys". In: **Phys. Rev. B** 66 (17 Nov. 2002), p. 174429. DOI: `10.1103/PhysRevB.66.174429`. URL: `https://link.aps.org/doi/10.1103/PhysRevB.66.174429`.

[124] Peter Swekis et al. "Magnetic and Electronic Properties of Weyl Semimetal Co2MnGa Thin Films". In: **Nanomaterials** 11.1 (2021), p. 251.

[125] Niko Pontius et al. "The FemtoSpeX facility at BESSY II". In: **Journal of large-scale research facilities JLSRF** 2 (2016), A46–A46.

[126] Sergej Solopow. "Wavelength dependent demagnetization dynamics in Co2MnGa Heusler-alloy". PhD thesis. Universität Potsdam, 2019.